

CONTROLLED GROWTH AND ASSEMBLY OF SINGLE-WALLED CARBON  
NANOTUBES FOR NANOELECTRONICS

by

Badr Omrane

M. A. Sc., École Polytechnique of Montréal, 2005

B. Eng., École Polytechnique of Montréal, 2003

A Dissertation Submitted in Partial Fulfillment  
of the Requirements for the Degree of

DOCTOR OF PHILOSOPHY

in the Department of Electrical and Computer Engineering

© BADR OMRANE, 2009  
University of Victoria

All rights reserved. This thesis may not be reproduced in whole or in part, by photocopy  
or other means, without the permission of the author.

## **Supervisory Committee**

### CONTROLLED GROWTH AND ASSEMBLY OF SINGLE-WALLED CARBON NANOTUBES FOR NANOELECTRONICS

by

Badr Omrane

M. A. Sc., École Polytechnique of Montréal, 2005

B. Eng., École Polytechnique of Montréal, 2003

#### **Supervisory Committee**

Dr. Chris Papadopoulos, (Department of Electrical and Computer Engineering)  
**Supervisor**

Dr. Daler N. Rakhmatov, (Department of Electrical and Computer Engineering)  
**Departmental Member**

Dr. Thomas E. Darcie, (Department of Electrical and Computer Engineering)  
**Departmental Member**

Dr. Frank C. J. M. van Veggel, (Department of Chemistry)  
**Outside Member**

## Abstract

Dr. Chris Papadopoulos, (Department of Electrical and Computer Engineering)  
**Supervisor**

Dr. Daler N. Rakhmatov, (Department of Electrical and Computer Engineering)  
**Departmental Member**

Dr. Thomas E. Darcie, (Department of Electrical and Computer Engineering)  
**Departmental Member**

Dr. Frank C. J. M. van Veggel, (Department of Chemistry)  
**Outside Member**

Carbon nanotubes are promising candidates for enhancing electronic devices in the future at the nanoscale level. Their integration into today's electronics has however been challenging due to the difficulties in controlling their orientation, location, chirality and diameter during formation. This thesis investigates and develops new techniques for the controlled growth and assembly of carbon nanotubes as a way to address some of these challenges.

Colloidal lithography using nanospheres of 450 nm in diameter, acting as a shadow mask during metal evaporation, has been used to pattern thin films of single-walled carbon nanotube multilayer catalysts on Si and Si/SiO<sub>2</sub> substrates. Large areas of periodic hexagonal catalyst islands were formed and chemical vapor deposition resulted in aligned single-walled carbon nanotubes on Si substrates within the hexagonal array of catalyst islands. On silicon dioxide, single-walled carbon nanotubes connecting the hexagonal catalyst islands were observed. To help explain these observations, a growth

model based on experimental data has been used. Electrostatic interaction, van der Waals interaction and gas flow appear to be the main forces contributing to single-walled carbon nanotube alignment on Si/SiO<sub>2</sub>. Although the alignment of single-walled carbon nanotubes on Si substrates is still not fully understood, it may be due to a combination of the above factors, in addition to silicide-nanotube interaction. Atomic force microscopy and Raman spectroscopy of the post-growth samples show single-walled carbon nanotubes of 1-2 nm in diameter. Based on the atomic force microscopy data and Raman spectra, a mixture of individual and bundles of metallic and semiconducting nanotubes were inferred to be present.

A novel technique based on direct nanowriting of carbon nanotube catalysts in liquid form has also been developed. The reliability of this method to produce nanoscale catalyst geometries in a highly controlled manner, as required for carbon nanotube growth and applications, was demonstrated. Chemical vapor deposition growth of the patterned regions shows individual and bundles of single-walled carbon nanotubes. This was confirmed by Raman spectroscopy of the samples, giving single-walled carbon nanotubes ~1-2 nm in diameter. The capabilities of the nanowriting process were also explored for direct-writing of carbon based nanomaterials such as single-walled carbon nanotubes and C<sub>60</sub> molecules.

Finally, a brief survey on carbon nanotube field-effect transistor modeling tools has been presented, followed by two-terminal current-voltage measurements on colloidal lithography and nanowriting samples. Results show primarily ohmic behavior with

conductances of  $\sim 0.86$ - $16.5 \mu\text{S}$  for the hexagonal catalyst array patterned samples for various geometries and  $\sim 0.27$ - $1 \mu\text{S}$  for the nanowriting samples. In addition, compact models have been used to gain insights into the device performance and the unique advantages of the hexagonal array approach over devices fabricated using parallel or randomly distributed SWCNTs. Device performance appears to be determined primarily by the contact resistance which includes both Schottky barrier resistances and an interface resistance.

In summary, colloidal lithography and direct-writing of single-walled carbon nanotube catalyst have been used to achieve the controlled growth and assembly of carbon nanotubes. Electronic transport of carbon nanotube devices fabricated using these two methods showed near ohmic behavior with device performance modeled primarily by the contact resistance. The approaches developed in this thesis allow nanoscale control over catalyst deposition and nanotube growth which makes them promising for the fabrication of future carbon nanotube electronic devices.

## Table of Contents

<b>Supervisory Committee .....</b>	<b>ii</b>
<b>Abstract.....</b>	<b>iii</b>
<b>Table of Contents .....</b>	<b>vi</b>
<b>List of Tables .....</b>	<b>ix</b>
<b>List of Figures.....</b>	<b>x</b>
<b>Acknowledgments .....</b>	<b>xix</b>
<b>1 Background on Carbon Nanotubes.....</b>	<b>1</b>
1.1 Carbon Nanotube Structure .....	5
1.2 Electronic Properties of Single-Walled Carbon Nanotubes .....	9
1.3 Phonon Properties in Single-Walled Carbon Nanotubes .....	18
1.4 Raman Spectroscopy .....	20
1.5 Carbon Nanotube Synthesis .....	22
1.5.1 Arc-Discharge Technique .....	23
1.5.2 Pulsed Laser Evaporation Technique.....	23
1.5.3 Catalytic Chemical Vapor Deposition .....	24
1.5.3.1 Carbon Nanotube Growth Model.....	24
1.5.3.2 Catalyst Particle Size and Support Layer.....	26
1.5.3.3 Temperature and gas feedstock.....	28
1.6 Control of Carbon Nanotube Growth.....	28
1.6.1 Catalyst Patterning .....	29
1.6.2 Substrate surface .....	30

1.6.3	Electric Field.....	32
1.7	Carbon Nanotube Electronic Devices .....	33
1.7.1	Carbon Nanotube Field-Effect Transistor.....	33
1.7.2	Effects of Metal Contacts on Carbon Nanotube Field-Effect Transistors .....	36
1.7.3	Beyond Carbon Nanotube Field-Effect Transistors.....	38
1.8	Scope of the Research and Thesis Outline .....	41
<b>2</b>	<b>Colloidal Lithography for Carbon Nanotube Catalyst Patterning .....</b>	<b>44</b>
2.1	Overview of Colloidal Lithography .....	44
2.2	Mask Formation .....	48
2.3	Catalyst Composition .....	49
2.4	Single-Walled Carbon Nanotube Growth .....	53
2.5	Experimental Results and Discussion .....	54
2.6	Summary .....	66
<b>3</b>	<b>Direct-Writing of Single-Walled Carbon Nanotube Catalysts .....</b>	<b>67</b>
3.1	Background on Nanowriting .....	67
3.2	Apparatus and Materials.....	69
3.2.1	Type of Catalysts Used.....	69
3.2.2	Al <sub>2</sub> O <sub>3</sub> -FeMo Catalyst.....	71
3.2.3	Cationized Ferritin Catalyst.....	72
3.3	Single-Walled Carbon Nanotube Growth .....	72
3.3.1	Al <sub>2</sub> O <sub>3</sub> -FeMo Catalyst.....	73
3.3.2	Cationized Ferritin Catalyst.....	73
3.4	Experimental Results and Discussion .....	73

3.5 Direct-Patterning of Nanostructures Using Nanopipettes .....	85
3.6 Summary .....	91
<b>4 Electronic Properties and Applications of Produced Single-Walled Carbon Nanotube Structures.....</b>	<b>93</b>
4.1 Survey of Carbon Nanotube Field-Effect Transistor Modeling Tools.....	93
4.2 Electronic Transport Measurements.....	102
4.2.1 Electronic Transport of the Colloidal Lithography Samples .....	102
4.2.2 Electronic Transport of the Nanowriting Samples.....	106
4.2.3 Discussion.....	107
4.3 Summary .....	111
<b>5 Conclusion and Future Work .....</b>	<b>112</b>
5.1 Future Work .....	114
5.1.1 Single-Walled Carbon Nanotube Catalyst Patterning Methods.....	114
5.1.2 Single-Walled Carbon Nanotube Electronic Devices.....	117
<b>6 Bibliography .....</b>	<b>120</b>

## List of Tables

Table 1-1: Classification of the different forms of carbon (adapted from [22]).....	6
Table 1-2: Mechanical and thermal properties of SWCNTs compared to other materials [6]. .....	20
Table 3-1: Catalyst height as a function of tip velocity .....	81
Table 3-2: Ferritin catalyst widths as a function of contact time.....	82
Table 4-1: Resistances of the CNTFET made of a SWCNT of 1.5 nm in diameter and 450 nm in length.....	101
Table 4-2: Zero bias conductances and resistances of each area of the post-growth hexagonal catalyst array evaporated on Si substrate.....	104
Table 4-3: Zero bias conductances and resistances for each area of the hexagonal catalyst array on Si/SiO <sub>2</sub> .....	106
Table 4-4: Conductances and resistances on the post-growth Al <sub>2</sub> O <sub>3</sub> -FeMo catalyst lines. ....	107

## List of Figures

- Figure 1-1: HRTEM of a) MWCNTs by Sumio Iijima in 1991 [2]; number of graphene layers forming CNT walls are respectively (left to right) 5, 2 and 7. b) SWCNT of 1.37 nm in diameter by Iijima *et al.* [3] in 1993, and c) SWCNT of ~1.2 nm in diameter by Bethune *et al.* [4] in 1993. ....2
- Figure 1-2: Schematic showing the structure of a graphite sheet (a.k.a. graphene), a SWCNT and a MWCNT [6]. ....2
- Figure 1-3: a) Intel MOSFET material advances versus years (adapted from [17]), and b) evolution of Intel CPU transistor count and feature sizes as a function of years [7]. ....4
- Figure 1-4: a) CNT target markets as a function of years (adapted from [18]), b) worldwide estimated production of SWCNTs in 2006 (adapted from [19]). ....5
- Figure 1-5: Hybridization process a) promotion of one electron from 2s to a higher energy level and recombination of s and p orbitals into  $sp^2$ , and b) planar orientation of  $sp^2$  orbitals at  $120^\circ$  from each other .....6
- Figure 1-6: a) Schematic of the honeycomb lattice of graphene showing the chiral vector  $\vec{C}_h = n\vec{a}_1 + m\vec{a}_2$  and the translation vector  $\vec{T}$  of the CNT unit cell defined by  $|\vec{T} \times \vec{C}_h|$ . Computational model [23] of b) a (7,0) zigzag SWCNT and c) its unit cell, d) (7,7) an armchair SWCNT and e) its unit cell. ....7
- Figure 1-7: a) First Brillouin zone showing the high symmetry point  $\Gamma$ ,  $K$  and  $M$ , b) energy dispersion of 2D graphite [20], and c) energy dispersion showing the six points of degeneracy corresponding to the junction of  $\pi^* - \pi$  bands at the fermi level. ....10
- Figure 1-8: One dimensional energy dispersion of a) a (7,0) metallic armchair SWCNT and b) a (7,7) direct bandgap semiconducting zigzag SWCNT [23]. Two-dimensional hexagonal Brillouin zone of graphene showing the allowed wavevectors of c) a zigzag (semiconducting) and d) an armchair (metallic) SWCNT [31]. e) Schematic of possible nanotube chiralities defined by the indices  $(n,m)$ . ....13

- Figure 1-9: a)-b) Modeling of the electronic density of states for semiconducting SWCNT [32], and c) experimental measurement of the conductance versus bias of a SWCNT using scanning tunneling microscopy (adapted from [33]). .....14
- Figure 1-10: a) Schematic of a semiconducting SWCNT DOS. Optical emission and absorption are represented by solid lines, while nonradiative relaxation of electrons and holes are depicted as dashed lines [37]. b) Two-dimensional map of the fluorescence intensity versus emission and excitation wavelengths [37].....15
- Figure 1-11: Measured conductance of a metallic SWCNT of a) 4  $\mu\text{m}$  and b) 300 nm in length. Results show conductances approaching the quantum conductance for CNTs and Fabry-Pérot interference at low temperature [41]. .....17
- Figure 1-12: a) Phonon dispersion of a 2D graphite showing: out-of-plane transverse acoustic (oTA), in-plane transverse acoustic (iTA), longitudinal acoustic (LA), out-of-plane transverse optic (oTO), in-plane transverse optic (iTO) and longitudinal optic (LO) mode. b) Phonon density of states of graphene (adapted from [45]) and c) displacement of carbon atom for each mode at  $k=0$  [25].....18
- Figure 1-13: a) Calculated phonon dispersion of a (10,10) armchair SWCNT showing 66 distinct phonon branches and b) its density of states [46]. Schematic of the c) out-of-plane transverse acoustic mode (oTA) in graphene that is linked to RBM in CNTs and d) the coupling of in- and out-of-plane acoustic modes due to nanotube curvature [20]. .....19
- Figure 1-14: a) Typical Raman spectrum of a SWCNT showing its three unique bands labelled as RBM, G-band and D-band (adapted from [51]). Bands from the silicon substrate are also observed in the spectrum. b) Raman spectroscopy of a semiconducting (left) and metallic (right) SWCNT (adapted from [52]);  $G^-$  linewidths are reported in parentheses and are much larger for metallic nanotubes. c) Relation between tube diameter and  $G^-$  and  $G^+$  bands [48] .....22
- Figure 1-15: a) Growth model of a SWCNT: [i] gas feedstock is decomposed into C and H atoms under high temperature, [ii] C atoms diffuse through the catalyst particle by concentration gradient, [iii] the metal particle becomes saturated, thus formation of carbide, and [iv] due to stress SWCNT nucleates from the carbide particle. b) Schematic of base growth mode (left nanotube) and tip growth mode (right nanotube) [28]. .....25

Figure 1-16: Growth rate for SWCNTs synthesized using a) Ni-MgO catalyst particles subjected to $C_2H_2$ gas [55]; sections I, II and III are respectively the incubation, growth and decay periods, and b) Co catalyst particles grown under ethanol vapor [5].	26
Figure 1-17: SEM images of CNT growth from iron nitrate catalyst using a) clean silicon substrate, b) a 3 nm, c) a 4 nm, and d) a 8 nm layer of $SiO_2$ (adapted from [63]). Growth is inhibited with oxide layer below 4 nm.	27
Figure 1-18: SEM of a) liquid catalyst islands patterning for SWCNTs growth [68], b) SWCNTs grown on top of silicon pillars with the help of gas flow that keeps the nanotubes floating above the surface until they reach adjacent pillars [67], and c) SWCNTs grown from Al/Fe/Mo catalyst islands [74].	30
Figure 1-19: SWCNTs aligned on a) sapphire, nanotubes direction is affected by the atomic arrangement of the substrate [77], b) on quartz, SWCNTs are aligned along the atomic steps [82], and c) on quartz, combination of gas flow and atomic steps are used to align SWCNTs [83].	31
Figure 1-20: Preferential alignment of SWCNTs a)-b) along intense electric field [89, 90], and c) orthogonal alignment using electric field and substrate surface [91].	32
Figure 1-21: Schematic of the firsts back-gate CNTFETs using a) gold [92] and b) platinum as electrodes [93]. Electrical measurements of the CNTFETs proposed by c) Martel <i>et al.</i> [92] and d) Tans <i>et al.</i> [93], showing a clear p-type behavior and an on/off ratio between five and six order of magnitude.	34
Figure 1-22: a) Schematic of a on-surface SWCNT-FET [69], and b) typical measured resistance at various temperature and $I-V$ curve for SWCNT-FET with enhanced contact resistance [94].	35
Figure 1-23: a) Schematic of a top-gate SWCNT-FET proposed by Wind <i>et al.</i> [95] and b) its $I-V$ measurements showing a p-type transistor action and a low gate voltage operation.	36
Figure 1-24: Schottky barrier height and on-state current versus single-walled carbon nanotube diameters [42]. Curves from top to bottom correspond respectively to Pd, Ti and Al contacts.	37
Figure 1-25: Band alignment of a Schottky barrier CNTFET showing: a) hole tunneling at negative gate voltages, b) electron tunneling at positive gate voltages, and c) $I-V$ measurements of a Schottky barrier CNTFET exhibiting a strong ambipolar behavior.	37

Figure 1-26: <i>I-V</i> measurements of a n-type CNTFET made by a) annealing the initial p-type nanotube in vacuum at 400 °C, and b) doping the initial p-type nanotube with potassium [99]. .....	38
Figure 1-27: a) Schematic of the first intramolecular inverter using p- and n-type SWCNT (adapted from [99]), and b) electrical behavior of the devices at $V = \pm 2$ V [99]. .....	39
Figure 1-28: Schematic of the optoelectronic device using a Schottky barrier CNTFET [102], and 2D map of the infrared emission for different gate voltage values. (adapted from [100]) .....	40
Figure 1-29: a) Atomic force microscopy and b) schematic of nanotube junction [103], c) <i>I-V</i> measurement of the nanotube junction showing rectification behavior [103], and d) MWCNT interconnect between two metal conductors [6]. Inset in c) is the <i>I-V</i> characterization of the metallic part in of the nanotube. ....	40
Figure 2-1: Schematic of nanosphere self-assembly into hexagonal close packed arrays: a) monolayer and b) bilayer of colloidal spheres. Parameters $a_{xx}$ and $d_{xx}$ are respectively the size of the opening and the distance between two adjacent openings, whereas subscript xx refers either to monolayer (ML) or bilayer (BL) of colloidal spheres. ....	45
Figure 2-2: Scanning electron microscopy of a) the effect of annealing on a colloidal mask using nanospheres of 540 nm in diameter; the initial opening size of 200 nm is decreased down to 25 nm upon annealing, and b) possible structure geometries obtained using different evaporation conditions and an annealed polystyrene mask [115]. ....	47
Figure 2-3: Schematic of SWCNT patterning process using polystyrene nanospheres: i) mask formation using colloidal spheres, ii) evaporation of a thin metal catalyst layer, iii) sphere removal, and iv) SWCNT growth via CVD. ....	47
Figure 2-4: Scanning electron microscope characterization of a colloidal mask [116] a) before and b) after annealing at 105 °C for 300 minutes. ....	49
Figure 2-5: Scanning electron microscope images of the influence of Al support layer and temperature on SWCNT growth: a) Si/ 200 nm SiO <sub>2</sub> / 0.5 nm Co at 750 °C; preheating 2 min under H <sub>2</sub> ; growth at 0.5 bar CH <sub>4</sub> ; b) Si/ 200 nm SiO <sub>2</sub> / 0.5 nm Co at 800 °C; preheating 2 min H <sub>2</sub> ; growth at 0.5 bar CH <sub>4</sub> , and c) Si/ 200 nm SiO <sub>2</sub> / 5 nm Al/ 0.5 nm Co at 750 °C; preheating 2 min H <sub>2</sub> ; growth 0.5 bar CH <sub>4</sub> [132]. ....	50

- Figure 2-6: Schematic of the catalyst multilayer composed of Ti/Au/Al/Co a) as evaporated, b) after the reduction step the active catalyst and support layer are transformed into smaller particles and c) growth of SWCNTs. ....52
- Figure 2-7: Schematic of the chemical vapor deposition furnace used for carbon nanotube growth. ....53
- Figure 2-8: Scanning electron microscopy of straight SWCNTs connecting catalyst islands grown on Si substrate from the multilayer metal catalysts evaporated at low rate. Mask removal is done using a)-b) ethanol and c-e) dichloromethane. Yellow arrows depict loss of alignment of the nanotubes at the edges of the hexagonal array of island catalysts. ....55
- Figure 2-9: Atomic force microscopy of straight SWCNTs on Si substrate connecting catalyst islands done at low evaporation rate. Height profiles b) and d) show typical SWCNT heights between ~1 and ~2 nm. ....56
- Figure 2-10: Atomic force microscopy at the extremity of the hexagonal array showing a SWCNT a)-b) T-junction, and c)-d) L-junctions. Height profiles b) and d) show SWCNT heights of 1-2nm. ....56
- Figure 2-11: Raman spectroscopy of samples done at low evaporation rate showing a) typical RBM, G- and D-bands, and b) a magnification of the G and G<sup>+</sup> bands of a metallic SWCNT. ....57
- Figure 2-12: a)-b) Scanning electron microscope characterizations of SWCNTs connecting catalyst islands grown on Si substrate from the multilayer metal catalysts evaporated at high rate, and c) atomic force microscopy of the post growth triangular catalyst islands. ....58
- Figure 2-13: Scanning electron microscope characterizations of SWCNTs connecting catalyst islands done at low evaporation rate on Si/SiO<sub>2</sub>. Yellow and red arrows denote respectively active and inactive catalyst island. No preferential alignment of SWCNTs within the hexagonal array of catalyst islands is reported and the bright background is due to the electron charging effect of the silicon oxide substrate [68]. ....59
- Figure 2-14: Schematic of the multilayer catalyst islands a) as evaporated, b) during growth and c) electrostatic interaction between a SWCNT and active catalyst islands (grey color). ....61
- Figure 2-15: Synthetic data using the a) extrusive energy and attractive force of the main island only (i.e. nucleation site), b) extrusive energy, attractive force of initial and adjacent island, and c) extrusive energy, van der Waals interaction and attractive force of initial and adjacent island. ....64

Figure 2-16: a)-c) Atomic force microscopy of a possible silicide nanowire directly attached to an aligned SWCNTs on silicon substrate.....	65
Figure 3-1: Concept of direct nanowriting of liquid catalyst using nanopipettes. Inset shows a SEM characterization of a 100 nm opening borosilicate glass nanopipette. ....	69
Figure 3-2: Scanning electron microscope characterizations of Fe-Mo catalyst a) without fumed alumina and b) with 15 mg (0.5 g/L) of fumed alumina (adapted from [155]). ....	70
Figure 3-3: Schematic of a ferritin protein showing a) the subunits, and b) the iron core (adapted from [158])......	71
Figure 3-4: Atomic force microscopy of straight parallel lines of catalyst drawn at 10 $\mu\text{m/s}$ on a)-b) Si substrate using borosilicate glass nanopipette filled with $\text{Al}_2\text{O}_3\text{-FeMo}$ catalyst, and c)-d) on a Si/SiO <sub>2</sub> substrate using quartz nanopipette filled with 1:200 dilution ferritin solution. ....	74
Figure 3-5: AFM image of $\text{Al}_2\text{O}_3\text{-FeMo}$ lines on Si prior to growth (patterned with borosilicate nanopipette). b) Cross-section of $\text{Al}_2\text{O}_3\text{-FeMo}$ lines $\sim 2.5$ nm in height. ....	75
Figure 3-6: Scanning electron microscopy of SWCNTs on a Si substrate grown from the $\text{Al}_2\text{O}_3\text{-FeMo}$ catalyst lines. ....	75
Figure 3-7: Atomic force microscopy of SWNTs grown from $\text{Al}_2\text{O}_3\text{-FeMo}$ lines. Cross-section profiles b) and d) show a height of $\sim 2.5$ nm. ....	76
Figure 3-8: Raman spectra of $\text{Al}_2\text{O}_3\text{-FeMo}$ sample following CVD. a) RBM band of SWNTs at $\sim 155\text{ cm}^{-1}$ , b) G-band at $\sim 1588\text{ cm}^{-1}$ and D-band at $\sim 1309\text{ cm}^{-1}$ of a metallic SWCNT, and c) G-band at $\sim 1590\text{ cm}^{-1}$ of a semiconducting SWCNT.....	77
Figure 3-9: Atomic force microscopy of ferritin catalyst (1:50 dilution) samples following CVD (patterned on silicon dioxide using quartz nanopipette). a) Individual SWNT on sample processed according to procedure (i) described in section 3.3.2. b) Cross-section showing a catalyst line of $\sim 2$ nm in height and a SWNT of $\sim 1$ nm in height. c) SWNT connecting two catalyst lines. ....	78
Figure 3-10: Atomic force microscopy of ferritin catalyst (1:50 dilution) samples following CVD (patterned on silicon dioxide using quartz nanopipette) a) Phase image showing a SWCNT guided between catalyst lines on sample processed using procedure (ii). b) Close-up image of the	

- SWCNTs and catalyst lines. c) Cross-section of a catalyst line of  $\sim 10$  nm in height and a SWCNT of  $\sim 1$  nm in height.....78
- Figure 3-11: Raman spectroscopy of post-growth ferritin samples showing a)-b) D- and G-bands respectively at  $\sim 1300$   $\text{cm}^{-1}$  and  $\sim 1590$   $\text{cm}^{-1}$ , and c) intensity map the G-band (intensity increases from blue to red with red at  $\sim 1590$   $\text{cm}^{-1}$ ).....79
- Figure 3-12: Atomic force microscopy of a) parallel lines drawn using borosilicate nanopipette with  $\text{Al}_2\text{O}_3$ -FeMo at velocities indicated, b) cross-section of 50  $\mu\text{m/s}$  and 10  $\mu\text{m/s}$  drawn lines displaying heights of 1.5 nm and 2.5 nm, respectively, and c) cross-section of 10  $\mu\text{m/s}$  and 5  $\mu\text{m/s}$  lines displaying heights of 2.5 nm and 3.5 nm, respectively. ....80
- Figure 3-13: Atomic force microscopy of a) parallel lines drawn using quartz nanopipette with 1:50 dilution ferritin solution at velocities indicated, b) cross-section of 50  $\mu\text{m/s}$  and 10  $\mu\text{m/s}$  drawn lines displaying heights of 9 nm and 15 nm respectively, and c) cross-section of 50  $\mu\text{m/s}$  and 10  $\mu\text{m/s}$  drawn lines displaying heights of 14 nm and 20 nm respectively.....80
- Figure 3-14: Atomic force microscopy of a) a 4 x 5 dot array drawn using quartz nanopipette filled with ferritin solution (1:200 dilution) for different contact times, b) a zig-zag of  $\text{Al}_2\text{O}_3$ -FeMo, and c)-d) overlapping ferritin lines and its 3D projection showing one catalyst line on top of the other (right).....81
- Figure 3-15: Schematic of the tip-liquid interaction while the nanopipette is retracted. a) The catalyst solution is delivered to the surface for an amount of time  $t$ , b)-c) while retracting the nanopipette the liquid is still delivered to the surface, and d) critical distance at which the meniscus breaks apart from the nanopipette tip. ....82
- Figure 3-16: Atomic force microscopy of a) initial ferritin line drawn on Si/SiO<sub>2</sub> using a quartz nanopipette, b) cross-section of ferritin line of  $\sim 25$  nm in height, c) ferritin line after calcination step displaying catalyst clustering, d) cross-section of ferritin line after calcination, and e) ferritin line depicted in Figure 3-14c) after calcination and f) its cross-section.....84
- Figure 3-17: a)-f) Atomic force microscopy of lines drawn using SWCNT in methanol solution on Si/SiO<sub>2</sub> substrates and a borosilicate nanopipette of 100 nm in diameter. ....87
- Figure 3-18: Patterns drawn using a borosilicate nanopipette of 250 nm in diameter and SWCNT/methanol solution at 10  $\mu\text{m/s}$ . a) Scanning electron microscopy of SWCNT lines on Si substrate. Atomic force microscopy

of SWCNT lines on b) Si, c) Si/SiO<sub>2</sub>, d)-e) close-up of a SWCNT emanating from a bundle on Si, and f) close up of a bundle on Si/SiO<sub>2</sub>. .....87

- Figure 3-19: Patterns drawn on Si substrates using borosilicate nanopipette of 100 nm in diameter and SWCNT/chloroform solution at 10  $\mu\text{m/s}$ . a)-b) Scanning electron microscopy of straight lines. Atomic force microscopy of c) straight lines, d)-e) close-up showing bundles of SWCNTs and f) their profile height. ....88
- Figure 3-20: Schematic of direct-nanowriting of SWCNT solutions showing a) aggregation of SWCNTs within the nanopipette and b) vapor pressure at each extremity. c) Schematic of a fullerene C<sub>60</sub> molecule made entirely of carbon atoms and d) STM of C<sub>60</sub> [168]. ....90
- Figure 3-21: Atomic force microscopy of lines drawn using C<sub>60</sub>/toluene and borosilicate nanopipette of 100 nm in diameter on a) Si, b)-f) Si/SiO<sub>2</sub>. Profile heights c) and f) display a height of  $\sim 2.5$  nm,  $\sim 1.5$  nm and  $\sim 2$  nm, respectively. ....91
- Figure 4-1: Schematic of the NEGF formalism: a) device representation [171] and b) the self-consistent iterative process [171]. Parameters  $E_F = 0$  and  $V_{DS}$  is the drain voltage. ....94
- Figure 4-2: Schematic of the a)  $I-V$  characterization of an isolated SWCNT connected to the drain/source electrodes, and b) its circuit model representation.  $R_C$ ,  $R_{CNT}$ ,  $R_{Sc}$ ,  $R_{op}$ ,  $R_{ac}$ ,  $R_{ch}$  are respectively the contact, nanotube quantum resistance, Schottky barrier, optical, acoustic and elastic resistance. ....100
- Figure 4-3: Numerical simulations of a 1.5 nm diameter CNTFET of 450 nm in length considering : a) ballistic transport, b) elastic scattering, and c) elastic scattering, inelastic scatterings and Schottky barriers. Gate voltages are set respective to 0 V (blue), 0.1 V (green), 0.2 V (red), and 0.3 V (cyan). ....101
- Figure 4-4: a) Schematic of the  $I-V$  characterizations of the post-CVD hexagonal arrays. Optical images of the areas of interest of a post-CVD growth hexagonal catalyst islands on Si substrate b) 10X objective, and c) 50X objective. Scanning electron microscopy of d) the three areas, and e)-f) close-up of the areas showing thin SWCNT films. ....103
- Figure 4-5: Two-terminal  $I-V$  measurements of the post-growth hexagonal array evaporated on Si: a) area 1 (see Figure 4-4c), b) area 2 of Figure 4-4d, and c) area 3 of Figure 4-4d. ....103

Figure 4-6: a) Optical images of the areas of interest of a post-CVD growth hexagonal catalyst islands on Si/SiO <sub>2</sub> substrate 50X objective, and b)-e) scanning electron microscopy of the area of interest showing thin SWCNT films.....	105
Figure 4-7: Two-terminal <i>I-V</i> measurements of the post-growth hexagonal catalyst array evaporated on Si/SiO <sub>2</sub> substrate performed between a) area 1 and 2, b) area 1 and 3, and c) area 4 and 5.....	105
Figure 4-8: Two-terminal <i>I-V</i> measurements performed between post-growth Al <sub>2</sub> O <sub>3</sub> -FeMo catalyst lines.....	106
Figure 4-9: Schematic of a 1.5 μm wide and 4.5 μm long CNT device made using a) parallel SWCNTs connecting gold electrodes, b) randomly distributed SWCNTs on the substrate, and c) SWCNTs grown via the hexagonal array. ....	108
Figure 4-10: Matlab numerical simulations of a 1.5 μm wide and 4.5 μm long CNT device made of 1.5 nm diameter SWCNTs: a) parallel SWCNTs connecting gold electrodes (Figure 4-9a), b) SWCNTs grown via the hexagonal array of (Figure 4-9c), and c) thin film of SWCNTs randomly distributed on the substrate (Figure 4-9b). ....	110
Figure 5-1: Simulation using Surface Evolver [184] of the effect of the wetting properties of the tip surface on the pattern dimensions: a) hydrophobic tip surface, and b) hydrophilic tip surface.....	116
Figure 5-2: Schematic of hexagonal array three-terminal CNTFET devices using a) a back-gate electrode, and b) a top-gate electrode patterned on top of SiO <sub>2</sub> or SiN <sub>4</sub> .....	119

## Acknowledgments

I would like to express my gratitude to my supervisor Dr. Chris Papadopoulos for his guidance and financial support. Without his constant suggestions and discussions this research would not have been possible.

I would like to thank the committee members Dr. Sylvain G. Cloutier, Dr. Thomas E. Darcie, Dr. Daler N. Rakhmatov and Dr. Frank C. J. M. van Veggel for taking the time to be part of my committee.

Above all, I am deeply grateful to my parents, sister and Gina Elizabeth Cragg for their support and constant encouragement during these last four years.

## 1 Background on Carbon Nanotubes

The first evidence of hollow carbon filaments of ~50 nm in diameter was reported as early as 1952 in the Journal of Physical Chemistry of Russia [1]. This discovery, however, went unnoticed for several reasons. First of all, restricted accesses to scientific publications during the cold war prevented the majority of scientists from appreciating the importance of such a finding. Moreover, at that time carbon filaments and nanotubes were solely studied to prevent their formation in coal and steel industry processing and in the coolant channels of nuclear reactors [1]. Thus investigations of their potential purposes and novel characteristics were not carried forward at the time due to lack of interest from the scientific world for these nanoscale structures.

It was only in 1991, owing to a powerful characterization tool known as high resolution transmission electron microscopy (HRTEM), that Sumio Iijima made an astonishing discovery of tiny hollow wires a mere few nanometers in diameter which consisted only of carbon atoms [2] (Figure 1-1a). The structures were initially named helical microtubules by the author but were later referred to as carbon nanotubes (CNTs). Sumio Iijima was able for the first time to distinguish graphene (i.e. single sheet of graphite) layers forming CNT walls and this led to multi-walled carbon nanotubes

(MWCNTs). Shortly thereafter, single-walled carbon nanotubes (SWCNTs) were reported separately by Iijima *et al.* [3] (Figure 1-1b) and Bethune *et al.* [4] (Figure 1-1c) in 1993.

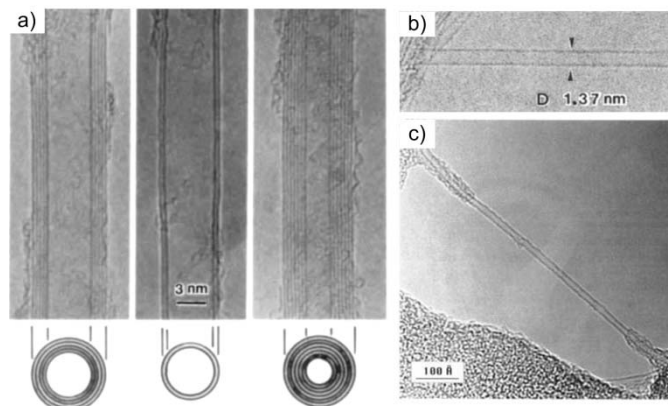


**Figure 1-1:** HRTEM of a) MWCNTs by Sumio Iijima in 1991 [2]; number of graphene layers forming CNT walls are respectively (left to right) 5, 2 and 7. b) SWCNT of 1.37 nm in diameter by Iijima *et al.* [3] in 1993, and c) SWCNT of  $\sim 1.2$  nm in diameter by Bethune *et al.* [4] in 1993.

As its name implies, a SWCNT is a hollow cylinder made by the rolling of a single plane of graphene, and typically has a diameter of 1-2 nm [5] and a length ranging up to several micrometers. A MWCNT on the other hand is composed of several concentric SWCNT shells (Figure 1-2).

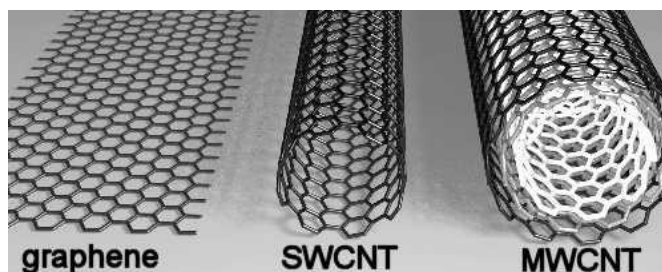


**Figure 1-2:** Schematic showing the structure of a graphite sheet (a.k.a. graphene), a SWCNT and a MWCNT [6].

The discovery of CNTs has brought about interest in many diverse research areas and in particular in the electronics field as the trend toward improving electronic devices by simply scaling down silicon features ended in the early 2000's due to excessive gate oxide leakage [7, 8]. Since then, the emergence of new materials such as strained silicon and gate dielectrics with high dielectric constants (a.k.a. high-k) (Figure 1-3a) have once more pushed the limit of aggressive scaling by respectively increasing carrier mobility and gate capacitance (Figure 1-3b). In 2007, Intel combined these innovations and 193 nm immersion lithography to construct the first 32 nm technology node, and is planning to release the first commercial chip using this technology at the end of 2009 [8-10]. Despite much progress, silicon technology will ultimately reach its limits in the next decade [9-11]. Some forecasts have predicted with the next process generation, the 22 nm technology node, the end of planar complementary metal-oxide semiconductor (CMOS) and the emergence of 3D gates surrounding the channels (a.k.a. tri-gates) [7, 12-15]. Below 20 nm the process of shrinking down silicon devices will no longer be economically viable and will become highly technologically challenging [9, 16]. Ultimately, as the devices shrink down below 10 nm the fundamental physical limits of CMOS technology will be reached and consequently new materials are needed [9, 16]. CNTs are seen as one of the most promising materials available to enhance electronic devices at the nanoscale level due to their unique physical properties and their potential to be integrated in current silicon technology.

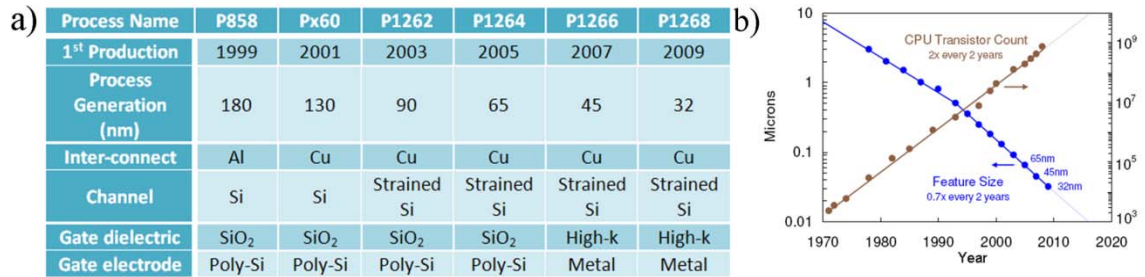


**Figure 1-3: a) Intel MOSFET material advances versus years (adapted from [17]), and b) evolution of Intel CPU transistor count and feature sizes as a function of years [7].**

Recent market analyses have shown a tremendous amount of interest toward CNTs in the last decade. From the initial \$US 6 million in 2004, the CNT market was evaluated as \$US 215 million in 2009 and is expected to reach \$US 1,070 million by the end of 2014 (Figure 1-4a) [18]. For MWCNTs alone, the total production in 2006 was evaluated to 271 tons per year [19]. Their intrinsic properties such as high thermal conductivity, mechanical strength and electrical conductivity make them suitable for sporting equipment, static-dissipative components, conductive body panels for electrostatic painting and flame retardant systems [18]. On the other hand, for the same year, the total production of SWCNTs was estimated at only ~6.9 tons per year (Figure 1-4 b) [20]. This substantial difference is due to the simple growth process of MWCNTs which makes them easier to fabricate at large scale and thus less expensive. However, as new suppliers emerge and control over the growth process is enhanced, the SWCNT market is projected to overtake MWCNTs, and by 2014 it is estimated at \$US 600 million (Figure 1-4a) [18]. The main target markets for SWCNTs are thought to be in transparent electrodes in displays, photovoltaics, molecular wiring in energy applications, biosensors, drug delivery, and semiconductors [18].

a)

\$ Millions	2004	2009	2014
<b>TOTAL DEMAND</b>	<b>\$6</b>	<b>\$215</b>	<b>\$1,070</b>
<b>BY TYPE</b>			
Single-Walled Nanotubes	0	95	600
Multiwalled Nanotubes	6	120	470
<b>BY END USE</b>			
Electronics	0	90	395
Automotive	1	31	165
Aerospace/Defense	0	10	65
Other	5	84	445
<b>BY REGION</b>			
U.S.	2	57	290
Western Europe	1	32	180
Asia/Pacific	3	113	500
Other	0	13	100

b)

Geography	Country	Company	Capacity (g/hr)	Capacity (kg /yr) *
Asia	China	NTP	85	500
Asia	China	Tsinghua (FW)	1000	1500
Asia	Korea	Iijin	1.25	2.4
Asia	Japan	Toray	15	1500
Asia	Japan	Mitsubishi	200	1200
Asia	Japan	Hata	100	600
Europe		Not Disclosed	---	100
North America	USA	CNI	65	113
North America	USA	SWeNT	6	12
North America	USA	Carbolex	100	600
North America	Canada	NRC-CNRC	120	720
North America	USA	Nano-C	2	12
<b>North America</b>			<b>293.0</b>	<b>1457</b>
<b>Europe</b>			<b>0.0</b>	<b>100</b>
<b>Asia</b>			<b>1401</b>	<b>5302</b>
<b>Total Capacity</b>			<b>1694.3</b>	<b>6859</b>

**Figure 1-4: a) CNT target markets as a function of years (adapted from [18]), b) worldwide estimated production of SWCNTs in 2006 (adapted from [19]).**

The tremendous amount of interest in CNTs is due to their unique characteristics and in order to understand their potential, it is important to understand the bonding and properties of the carbon atom.

## 1.1 Carbon Nanotube Structure

Carbon (C) is the sixth element of the periodic table and is responsible for some of the most varied structures in nature including diamond, graphite and living cells. The atomic configuration of carbon as an isolated element consists of six electrons orbiting around a nucleus composed of six protons and six neutrons. Two of the electrons with opposite spins lie within the first quantum state while the remaining four electrons are spread on the second quantum state, thus the ground-state electron configuration of carbon atom is  $1s^2 2s^2 2p^2$ . When carbon atoms are brought close to each other, an excited state labeled as  $1s^2 2s 2p^3$  is followed by recombination of  $2s$  and  $2p$  atomic orbitals to form directional hybrid orbitals (see Figure 1-5). This process, well-known as hybridization [21], is highly favorable as it increases the overlap of orbitals and creates strong and stable covalent bonds between carbon atoms.

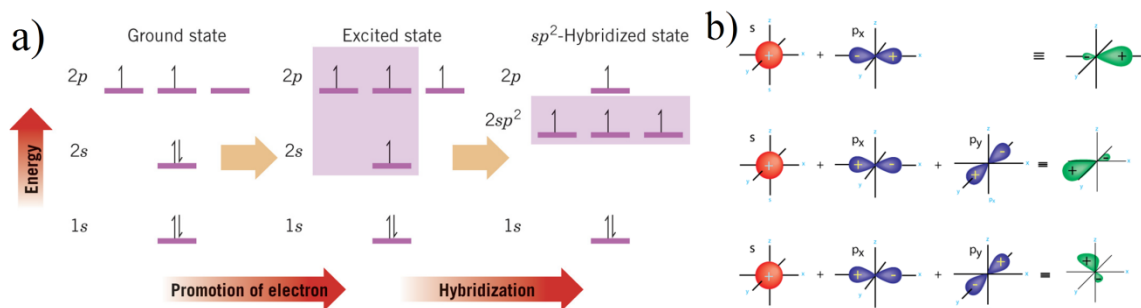


**Figure 1-5: Hybridization process a) promotion of one electron from 2s to a higher energy level and recombination of s and p orbitals into  $sp^2$ , and b) planar orientation of  $sp^2$  orbitals at  $120^\circ$  from each other .**

The wavefunctions for these three  $sp^2$  orbitals are expressed as follows [20]:

$$\begin{aligned}
 |sp_a^2\rangle &= \frac{1}{\sqrt{3}}|2s\rangle + \sqrt{\frac{2}{3}}|2p_x\rangle \\
 |sp_b^2\rangle &= \frac{1}{\sqrt{3}}|2s\rangle - \frac{1}{\sqrt{6}}|2p_x\rangle + \frac{1}{\sqrt{2}}|2p_y\rangle \\
 |sp_c^2\rangle &= \frac{1}{\sqrt{3}}|2s\rangle - \frac{1}{\sqrt{6}}|2p_x\rangle - \frac{1}{\sqrt{2}}|2p_y\rangle
 \end{aligned} \tag{1.1}$$

where  $|2s\rangle$ ,  $|2p_x\rangle$  and  $|2p_y\rangle$  refer respectively to the wavefunctions of 2s,  $2p_x$  and  $2p_y$  orbital. Normalization constants are found by applying orthogonality criteria [20]. Other possible C-C bond configurations are reported along with their respective attributes in Table 1-1.

**Table 1-1: Classification of the different forms of carbon (adapted from [22])**

Crystalline Form	Diamonds	Graphites	Carbynes
Hybridization	$sp^3$	$sp^2$	$sp^1$
Bonding	4	3	2
Dimension	3	2	1
Bond length (Å)	1.54	1.42	1.21
Bond energy (eV/mole)	15	25	35

As seen by the graphene sheet depicted in Figure 1-1, each initial carbon atom undergoes a change in its bonding configuration, that is one  $2s$  and two  $2p$  electrons mix to form three  $sp^2$  orbitals at  $120^\circ$  from each other as shown in Figure 1-5b. These three orbitals overlap head-to-head with adjacent  $sp^2$  orbitals and form planar directional molecular orbitals that are symmetrical around the bond axis (a.k.a.  $\sigma$ -bonds). The remaining  $p$  atomic orbital of each carbon atom combines side-to-side with adjacent  $p$  orbitals to form delocalized molecular  $\pi$ -bonds. This trigonal-planar configuration leads to a honeycomb lattice as depicted in Figure 1-6a. The real space unit vectors  $\vec{a}_1$  and  $\vec{a}_2$  of this hexagonal lattice are [20]:

$$\vec{a}_1 = \frac{\sqrt{3}a_{C-C}}{2}(\sqrt{3}, 1), \quad \vec{a}_2 = \frac{\sqrt{3}a_{C-C}}{2}(\sqrt{3}, -1) \quad (1.2)$$

where  $a_{C-C} = 1.42 \text{ \AA}$  is the distance between two carbon atoms in the graphene lattice [20].

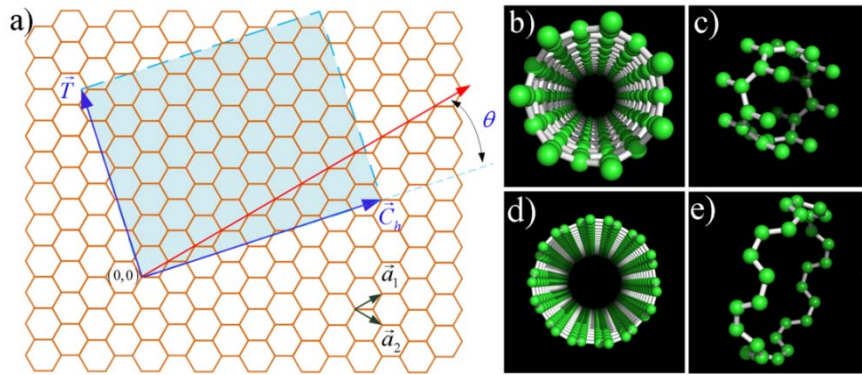


**Figure 1-6:** a) Schematic of the honeycomb lattice of graphene showing the chiral vector  $\vec{C}_h = n\vec{a}_1 + m\vec{a}_2$  and the translation vector  $\vec{T}$  of the CNT unit cell defined by  $|\vec{T} \times \vec{C}_h|$ . Computational model [23] of b) a (7,0) zigzag SWCNT and c) its unit cell, d) (7,7) an armchair SWCNT and e) its unit cell.

A SWCNT is made by rolling up a graphene sheet along a vector  $\vec{C}_h$  called the chiral vector as shown in Figure 1-6a and is written in term of the real space vectors  $\vec{a}_1$  and  $\vec{a}_2$  as follows [20]:

$$\vec{C}_h = n\vec{a}_1 + m\vec{a}_2 \equiv (n, m), \quad (n, m \text{ are integer}) \quad (1.3)$$

The nanotube circumference is thus  $C = |\vec{C}_h| = \sqrt{3}a_{c-c}\sqrt{n^2 + nm + m^2}$  [20]. By rolling up the graphene, the circular curvature causes  $\sigma - \pi$  rehybridization, which leads to  $\sigma$ -bonds out of plane and a more delocalized  $\pi$  orbital outside the tube. The translation vector  $\vec{T}$  is parallel to the CNT axis and takes the following form [20]:

$$\vec{T} = \frac{2m+n}{d_R}a_1 - \frac{2n+m}{d_R}a_2 \quad (1.4)$$

$$\text{where, } d_R = \begin{cases} d & \text{if } n-m \text{ is not a multiple of } 3d \\ 3d & \text{if } n-m \text{ is a multiple of } 3d \end{cases} \quad (1.5)$$

The primitive unit cell of a nanotube (e.g. Figure 1-6c and e) is defined by the area  $|\vec{T} \times \vec{C}|$  and CNTs of different lengths can be constructed by simply translating this primitive cell along  $\vec{T}$ . The angle from the unit vector  $\vec{a}_1$  at which the nanotube will be rolled up along  $\vec{C}_h$  is defined as the chiral angle and takes the following form [20]:

$$\theta = \cos^{-1} \left[ \frac{2n+m}{2\sqrt{n^2 + m^2 + nm}} \right], \quad 0 \leq \theta \leq \pi/6 \quad (1.6)$$

Nanotubes with chiral angles of  $\theta = 0^\circ$  and  $\theta = 30^\circ$  are labeled respectively as  $(n,0)$  zigzag and  $(n,n)$  armchair CNTs due to the shape of their cross-sectional ring as shown in Figure 1-6c and e. On the other hand, nanotubes with  $0^\circ < \theta < 30^\circ$  are referred to as chiral nanotubes, and in contrast to armchair and zigzag CNTs, their mirror image cannot be superposed to the original one [22, 24]. Finally, the nanotube diameter is defined as [20]:

$$d_t = \frac{C}{\pi} = \frac{\sqrt{3}a_{C-C}(m^2 + mn + n^2)^{1/2}}{\pi} \quad (1.7)$$

## 1.2 Electronic Properties of Single-Walled Carbon Nanotubes

The first step to understanding the unique electronic properties of carbon nanotubes is to analyze the band structure of 2D graphite since this is the basic structure of the CNT. The tight binding model [20, 25] is usually used to calculate the graphene valence (bonding) and conduction (anti-bonding) bands commonly referred to as  $\pi^* - \pi$  bands. This is done by considering two  $p_z$  orbitals per graphene unit cell and the nearest neighboring interaction. The first Brillouin zone of graphene in the reciprocal lattice is hexagonal as depicted in Figure 1-7a and the unit vectors  $\vec{b}_1$  and  $\vec{b}_2$  of the reciprocal lattice are [20]:

$$\vec{b}_1 = \frac{2\pi}{3a_{C-C}}(1,1), \quad \vec{b}_2 = \frac{2\pi}{3a_{C-C}}(1,-1) \quad (1.8)$$

The energy dispersion of the  $\pi^* - \pi$  bands of graphene in this region is expressed as follows [20]:

$$E_{G_{\pi^*-\pi}}(k_x, k_y) = \pm \xi_0 \sqrt{1 + 4 \cos\left(\frac{3k_x a_{C-C}}{2}\right) \cos\left(\frac{\sqrt{3}k_y a_{C-C}}{2}\right) + 4 \cos^2\left(\frac{\sqrt{3}k_y a_{C-C}}{2}\right)} \quad (1.9)$$

where (+) and (-) are respectively the conduction and valence bands, and are symmetric near the Fermi point as displayed in Figure 1-7b and c. Parameters  $\xi_0$ ,  $k_x$  and  $k_y$  are respectively the transfer integral that is typically set between -2.5 and -3.0 eV, and the wavevectors along the  $x$  and  $y$  axis. Complex and detailed calculations using multiple orbitals and many adjacent neighbor atoms have also been performed with the conclusion that tight binding approximation is highly reliable at retrieving the energy dispersion near the Fermi point of the graphene sheet. The same process can also be used to get the six  $\sigma - \sigma^*$  bands of graphene in the first Brillouin zone as shown in Figure 1-7b.

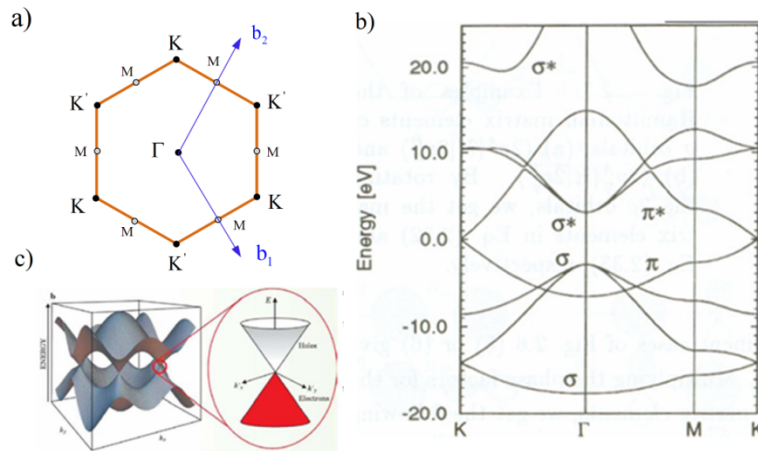


**Figure 1-7: a) First Brillouin zone showing the high symmetry point  $\Gamma$ ,  $K$  and  $M$ , b) energy dispersion of 2D graphite [20], and c) energy dispersion showing the six points of degeneracy corresponding to the junction of  $\pi^* - \pi$  bands at the fermi level.**

The electrical characteristics of CNTs are intimately related to the electronic band structure of graphene. In the Fermi surface of graphene an occupied  $\pi$  and an empty  $\pi^*$  band meet at the Fermi level at six points in the two-dimensional hexagonal Brillouin zone causing the graphene to behave as a zero bandgap semiconductor (Figure 1-7b and c). For low energies near the six  $K$  points, the energy dispersion is linear and is often referred to as a Dirac cone represented by the following relation [26]:

$$E(k_x, k_y) = \hbar v_F \sqrt{k_x^2 + k_y^2} \quad (1.10)$$

where  $\hbar$  and  $v_F$  are respectively the reduced Plank constant and Fermi velocity. This symmetrical linear relation near the  $K$  points leads to a zero effective mass for electrons and holes, and an equivalent mobility for both carriers [26]. When a graphite sheet is rolled along the chiral vector  $\vec{C}_h$  (see Figure 1-6a) to form a nanotube, electrons become confined in the circumferential direction. Therefore, integer numbers of the Broglie waves are permitted around the nanotube rim and consequently only certain wavevectors  $k_\perp$  along the circumferential direction are allowed [27]:

$$C_h \cdot k_\perp = 2\pi q \quad (1.11)$$

where parameter  $q$  is an integer number. These allowed wavevectors depend on the chirality and the diameter of the nanotube [28]. In the reciprocal lattice, vectors  $\vec{C}_h$  and  $\vec{T}$  are substituted by  $\vec{K}_1$  and  $\vec{K}_2$  which denote the discrete vector along the

circumference and along the nanotube axis. These vectors are expressed by the pair of reciprocal lattice vectors  $\vec{b}_1$  and  $\vec{b}_2$  as follows [20]:

$$\begin{aligned}\vec{K}_1 &= \frac{(2n + m)\vec{b}_1 + (2m + n)\vec{b}_2}{N d_R} \\ \vec{K}_2 &= \frac{m\vec{b}_1 + n\vec{b}_2}{N}\end{aligned}\tag{1.12}$$

where  $N = |\vec{C}_h \times \vec{T}| / |\vec{a}_1 \times \vec{a}_2|$  is the number of hexagons in the nanotube unit cell. It should be noted that for long CNTs (i.e. CNT length > 100 nm), the wavevector  $K_2$  is continuous [29], while for shorter CNTs, quantization has been observed [20]. The length of vector  $K_2$ , that is  $2\pi / |T|$ , corresponds to the length of the 1D first Brillouin zone of the nanotube [20]. Furthermore, the total number of allowed wavevectors around the nanotube circumference is found using eq. (1.11) and eq. (1.12) to be  $k_\perp = qK_1$  ( $q = 0, \dots, N-1$ ) and the distance between each one is  $\Delta k_\perp = 2\pi / |C_h| = 2 / d_t$  [30]. Using these parameters, the band structure of a SWCNT can be obtained by zone-folding the two-dimensional graphene energy dispersion using the following relation [20]:

$$E_{CNT_{\pi^*-\pi}}(k_\parallel) = E_{G_{\pi^*-\pi}}\left(k_\parallel \frac{K_2}{|K_2|} + qK_1\right)\tag{1.12}$$

where  $-\pi / |T| < k_\parallel < \pi / |T|$  is the wavevector along the nanotube axis. Due to electron confinement in the circumferential direction, the one-dimensional energy dispersion of

nanotube deviates from the initial zero bandgap semiconductor behavior of graphene and exhibit now either semiconducting or metallic behavior as shown in Figure 1-8.

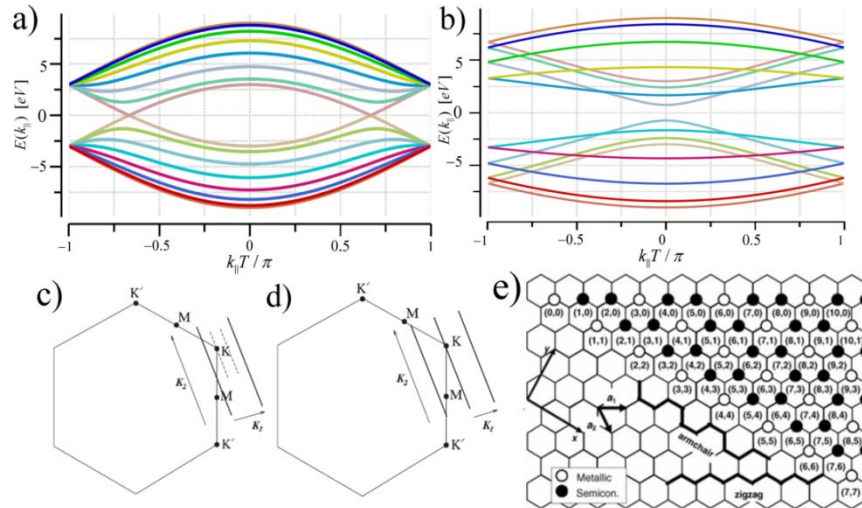


**Figure 1-8: One dimensional energy dispersion of a) a (7,0) metallic armchair SWCNT and b) a (7,7) direct bandgap semiconducting zigzag SWCNT [23]. Two-dimensional hexagonal Brillouin zone of graphene showing the allowed wavevectors of c) a zigzag (semiconducting) and d) an armchair (metallic) SWCNT [31]. e) Schematic of possible nanotube chiralities defined by the indices  $(n,m)$ .**

This behaviour depends on whether or not the allowed wavevectors include the point  $K$  of the two-dimensional hexagonal Brillouin zone of graphene (Figure 1-8a and b). A more general rule for differentiating between metallic and semiconducting SWCNTs is: if  $n=m$  or  $(n-m)/3=integer$  then the tube is metallic, otherwise it is semiconducting [20] (Figure 1-8c and d). The one dimensional electronic nature of SWCNTs is also observed in their density of states (DOS). Hence, DOS calculations of both metallic and semiconducting nanotubes exhibit van Hove singularities (vHs) [20] due to one-dimensional subbands as can be seen in Figure 1-9.

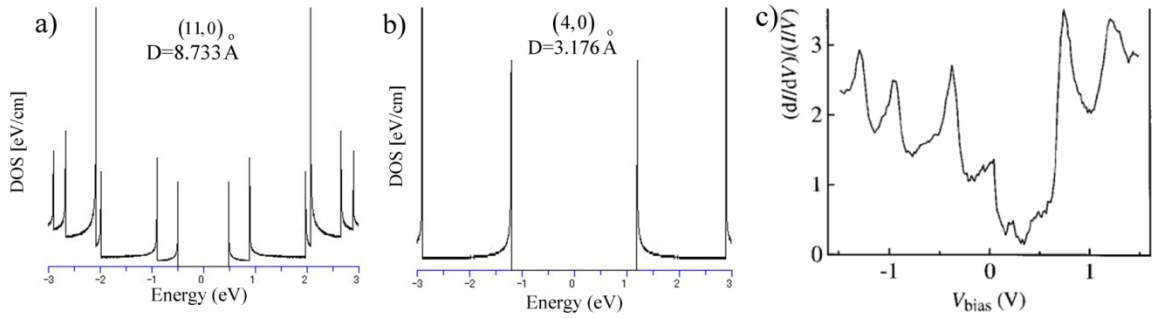


**Figure 1-9: a)-b) Modeling of the electronic density of states for semiconducting SWCNT [32], and c) experimental measurement of the conductance versus bias of a SWCNT using scanning tunneling microscopy (adapted from [33]).**

The semiconducting nanotube direct bandgap is inversely proportional to the nanotube diameter according to the following relation [20]:

$$E_g = \frac{2|\xi_0|a_{C-C}}{d_t} = \frac{4h\nu_F}{3d_t} \quad (1.13)$$

where  $h$  is the Plank constant. For instance, SWCNTs of 1 nm in diameter have  $E_g \approx 0.84$  eV, while for nanotubes of 2 nm in diameter the energy bandgap decreases to  $E_g \approx 0.42$  eV. Experimental verification using scanning tunneling microscopy (STM) have also confirmed vHs in the DOS of SWCNTs as shown in Figure1-9c [33]. However, in contrast to the standard DOS calculations, the results show a shift of the Fermi level toward the valence band which has been attributed to nanotube-substrate interaction and/or adsorption of oxygen molecules on the nanotube sidewalls [34]. Probing of the nanotube band structure has also been conducted by measuring the nanotube capacitance using three terminal devices [35].

Furthermore, due to the unique shape of the DOS of semiconducting carbon nanotubes, one should expect photoluminescence [31-35] from electrons and holes recombination at each joint density of states (JDOS), or in other words, at each transition between the corresponding  $\nu$ Hs singularities in the valence and conduction bands [36] (Figure 1-10a). However in most cases, CNTs form bundles and due to the presence of metallic CNTs that can act as relaxation channels [36], photoluminescence is not observed. One way of dealing with this problem is to sonicate SWCNTs in sodium dodecyl sulphate (SDS) to form uniform suspension of individual SWCNTs [37]. Spectrofluorimetric measurements of SWCNTs in SDS show intense emission at some specific wavelengths corresponding to optical band transmissions between bands as depicted in Figure 1-10b [37].

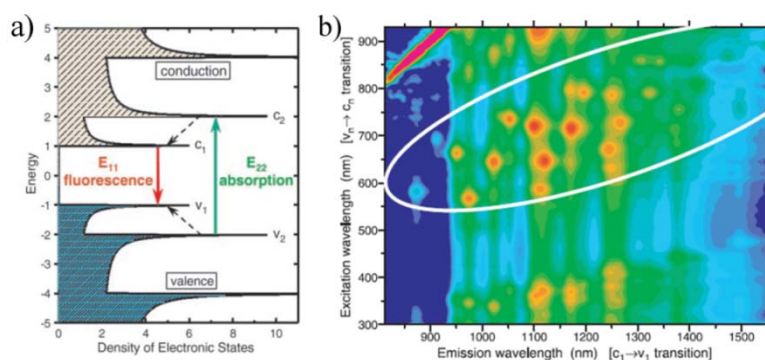


**Figure 1-10:** a) Schematic of a semiconducting SWCNT DOS. Optical emission and absorption are represented by solid lines, while nonradiative relaxation of electrons and holes are depicted as dashed lines [37]. b) Two-dimensional map of the fluorescence intensity versus emission and excitation wavelengths [37].

Intensities within the white oval in Figure 1-10b are due to  $\nu_2$ - $c_2$  absorption and then  $c_1$ - $\nu_1$  relaxation. Shorter excitation wavelengths are attributed to  $\nu_3$ - $c_3$  transition

followed by  $c_I-v_I$  relaxation. These experimental results assess the correlation between the optical properties of CNTs and their structural morphology, hence their chirality.

Electrical transport in SWCNTs is dictated by their long scattering length due to low number of scattering events. Since a nanotube is a 1D structure, scatterings at random angles are inhibited as a consequence of the  $k$ -space confinement [38]. Therefore, only forward and backward propagations in the nanotubes are allowed, and consequently only forward and backscattering are permitted [39]. The scattering process depends on three parameters that are elastic scattering within the nanotube, acoustic and optical phonons inelastic scatterings [40]. The first two have a mean free-path of approximately 1  $\mu\text{m}$  [40] and thus contribute weakly to the scattering process. On the other hand, optical phonons, with their short mean free-paths of  $\sim 20\text{-}30$  nm [40], contribute strongly to the scattering process at elevated carrier energy exceeding  $\sim 180$  meV [40]. It was reported by Mann *et al.* [41] that metallic SWCNTs exhibit ballistic transport over long lengths which implies no heat dissipation in the nanotube and consequently, a large current density is obtained. Measured conductance showed ballistic transport in the nanotube and a conductance close to the quantum limit for CNTs [42] (i.e.  $G_{max} = 4e^2/h$  or  $R_{min} = 6.5$  k $\Omega$ ) as shown in Figure 1-11a and b. The highest measured conductances ( lowest resistances) for SWCNTs at 4 K were reported by Liang *et al.* [43] to be approximately  $G = 3.71e^2/h$  or 7 k $\Omega$ . This small deviation from the quantum limit is attributed to the Schottky barriers created at the nanotube-electrode junctions (see section 1.7.2). Another consequence of these barriers on the electrical transport of CNTs is the appearance of Fabry-Pérot interference at low temperature [43] as displayed in Figure 1-11a and b.

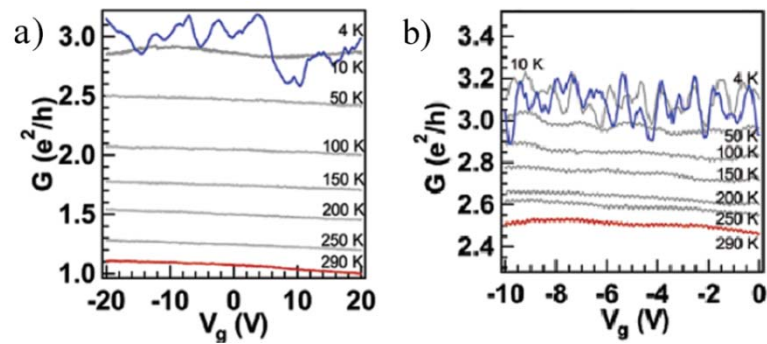


**Figure 1-11: Measured conductance of a metallic SWCNT of a) 4  $\mu\text{m}$  and b) 300 nm in length. Results show conductances approaching the quantum conductance for CNTs and Fabry-Pérot interference at low temperature [41].**

The ballistic behavior in metallic CNTs has since been observed in semiconducting nanotubes over distances of hundreds of nanometers [36-40]. With their ballistic transport and current densities two orders of magnitude higher than copper, metallic nanotubes are seen as nano-interconnects in future integrated circuits (ICs) (see section 1.7). Semiconducting nanotubes with their high current densities and a bandgap defined by the tube diameter are possible replacements for future silicon field effect transistors (FET) which will also be discussed in section 1.7.

Unlike SWCNTs, MWCNTs have received less attention for electronics because of their more complex structure and higher quantity of structural defects. In MWCNTs, each carbon shell may have a different electronic property, chirality and shell to shell interaction making them less practical for use in nanoelectronics [44]. For this reason, only SWCNTs will be explicitly covered in the following sections.

### 1.3 Phonon Properties in Single-Walled Carbon Nanotubes

Phonons provide important information regarding the thermal and electrical conductivity in atomic lattices, and their vibrational spectra determine the elastic and mechanical properties of solids [45]. Since a SWCNT is essentially a rolled-up graphite sheet, a natural starting point for retrieving SWCNT phonon dispersion consists of zone folding the phonon dispersion relation of graphene [20]. 2D graphite has two carbon atoms per unit cell and three spatial tensors giving rise to six phonon branches divided into three acoustic modes starting at  $\omega = 0$ , and three optical modes at  $\omega \neq 0$  as can be seen in Figure 1-12 [15, 37-39].

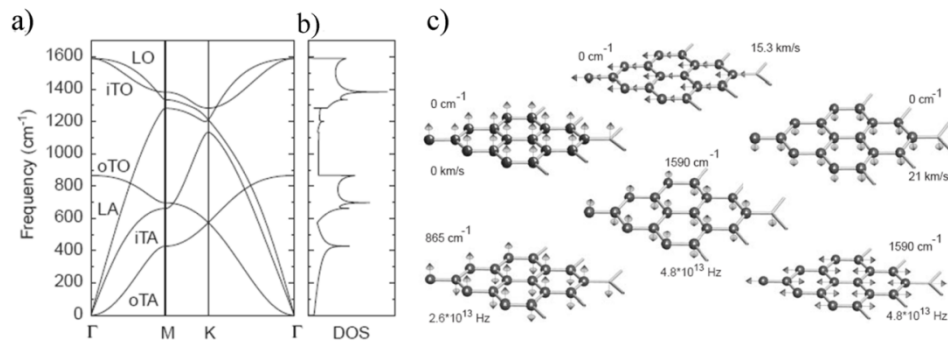


**Figure 1-12: a) Phonon dispersion of a 2D graphite showing: out-of-plane transverse acoustic (oTA), in-plane transverse acoustic (iTA), longitudinal acoustic (LA), out-of-plane transverse optic (oTO), in-plane transverse optic (iTO) and longitudinal optic (LO) mode. b) Phonon density of states of graphene (adapted from [45]) and c) displacement of carbon atom for each mode at  $k=0$  [25].**

The phonon dispersion relation of SWCNTs is found by folding the phonon dispersion of graphene along the chiral vector  $\vec{C}_h$ . This method gives  $6N$  phonon branches (see Figure 1-13a) divided into four acoustic modes and  $6N-4$  optical modes. The one-dimensional nature of SWCNTs is clearly visible in Figure 1-13b. Despite the

fact that zone folding method gives a good estimate of the phonon properties of SWCNTs at high energy, it suffers major drawbacks. For instance, the out-of-plane transverse acoustic mode (oTA) of graphene has  $\omega = 0$  at  $k=0$ , while the associated mode in SWCNTs, labeled as radial breathing mode (RBM), must be  $\omega \neq 0$  since it involves bond stretching (Figure 1-13c) [20, 46]. Another weakness of zone folding is the coupling of in- and out-of-plane acoustic modes introduced by the roll-up of the graphene to form acoustic mode of the SWCNT (Figure 1-13c) [20, 46].

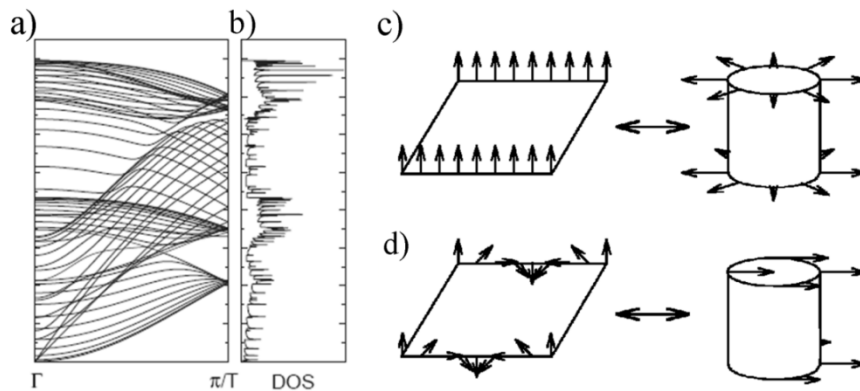


**Figure 1-13: a) Calculated phonon dispersion of a (10,10) armchair SWCNT showing 66 distinct phonon branches and b) its density of states [46]. Schematic of the c) out-of-plane transverse acoustic mode (oTA) in graphene that is linked to RBM in CNTs and d) the coupling of in- and out-of-plane acoustic modes due to nanotube curvature [20].**

Eventually, the zone folding method has to be abandoned and replaced by a direct force-constant calculation [20, 46] in order to produce a more accurate depiction of the phonon dispersion of SWCNTs. The four SWCNT acoustic branches at low energy are directly related to heat transport and charge carrier scatterings [45]. The unique mechanical and thermal properties of SWCNTs compared to some common materials are reported in Table 1-2.

**Table 1-2: Mechanical and thermal properties of SWCNTs compared to other materials [6].**

Material	Young's Modulus (GPa)	Tensile Strength (GPa)	Density (g/cm <sup>3</sup> )	Thermal Conductivity (W/m.K)
SWCNT	1054	150	1.4	6000
Diamond	600	130	3.5	900-2320
Steel	208	~ 0.65-1	7.8	~ 12-45

#### 1.4 Raman Spectroscopy

Raman spectroscopy, named after C. V. Raman [47], is one of the most powerful tools for carbon nanotube characterization as it provides a fast and noninvasive analysis of the object under test. This technique is based on the measurement of inelastic scattering of light that is the scattering of light in which the energy of the photon changes, and consequently corresponds to shifts from the frequency of the incident light. By exposing a sample to a monochromatic beam of light, electrons are excited from the valence to the conduction band by absorbing photons. These electrons will scatter by either emitting or absorbing phonons, and finally relax to the valence band by emitting photons. Most of the scattered light is elastic (i.e. Rayleigh scattering) while only a minority is inelastic (i.e. Stokes or anti-Stokes).

Applied to CNTs, Raman spectroscopy provides unique information regarding the nanotube type (i.e. semiconducting or metallic), diameter and structural quality (i.e. defects). Among the  $6N$  phonon dispersion branches of carbon nanotubes, just few of them are Raman active, and due to energy-momentum conservation, only vectors around  $k=0$  are coupled to the incident light [20]. CNTs have a unique signature that makes them easily recognizable by Raman spectroscopy. Under external illumination, the Raman spectrum of CNTs is characterized by three specific bands involving one phonon

emission: two first order Raman modes labeled respectively as radial breathing mode (RBM) and G-band, and one second order Raman mode referred to as D-band (see Figure 1-14a). The RBM is generally observed between 75 and 300  $\text{cm}^{-1}$ , and provides crucial information on the nanotube diameters according to the following relation [48]:

$$d_t = 248 \text{cm}^{-1} \text{nm} / \omega_{RBM} \quad (1.14)$$

where  $\omega_{RBM}$  is the frequency associated with the RBM band. It should be noted that eq. (1.14) is valid for only individual and isolated SWCNTs, while for SWCNT bundles a shift of  $\sim 14 \text{cm}^{-1}$  due to van der Waals interaction between nanotubes must be considered [49]. The D-band is usually located at 1330-1360  $\text{cm}^{-1}$  and specifically for SWCNTs it is generally related to defects and amorphous carbon on the surface [48], while the G-band corresponds to the stretching mode in the graphite plane and for CNTs, it is located around 1590  $\text{cm}^{-1}$ . The crystalline domain size of the nanotube can be found according to the following equation [50]:

$$L_a = 2.4 \times 10^{-10} \lambda_{laser}^4 \left( \frac{I_G}{I_D} \right) \quad (1.15)$$

where  $\lambda_{laser}$ ,  $I_G$  and  $I_D$  are respectively the laser wavelength, G-band intensity and D-band intensity. In addition, one can differentiate between semiconducting and metallic nanotubes by analyzing the G-band lineshape that consists of two distinct bands labeled as  $G^+$  and  $G^-$ . The first band is associated with the longitudinal optical phonon mode and it is sensitive to dopant additions, while the second band is attributed to the transverse optical mode and its width is sensitive to the nanotube type [45]. More precisely, for

metallic CNTs the  $G^-$  is broad compared to semiconducting tubes as one can notice in Figure 1-14b.

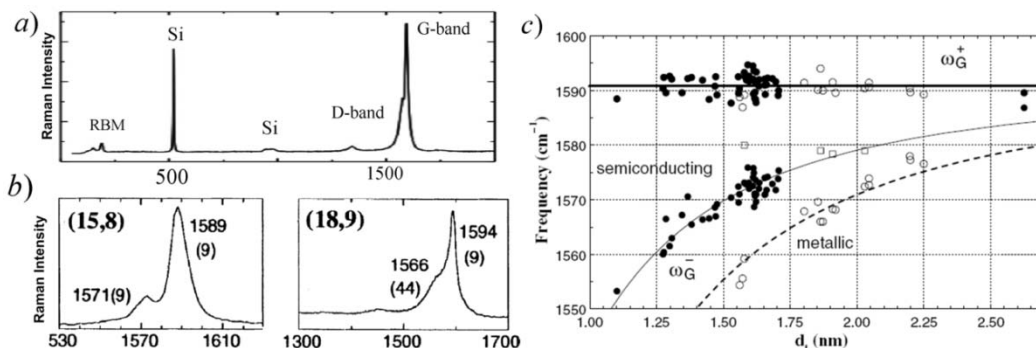


**Figure 1-14:** a) Typical Raman spectrum of a SWCNT showing its three unique bands labelled as RBM, G-band and D-band (adapted from [51]). Bands from the silicon substrate are also observed in the spectrum. b) Raman spectroscopy of a semiconducting (left) and metallic (right) SWCNT (adapted from [52]);  $G^-$  linewidths are reported in parentheses and are much larger for metallic nanotubes. c) Relation between tube diameter and  $G^-$  and  $G^+$  bands [48]

Nanotube diameter can also be approximated using the  $G^-$  and  $G^+$  bands. One can notice in Figure 1-14b that  $G^+$  is independent of tube diameter, while in contrast  $G^-$  is correlated to the diameter [48]. Raman characterization of isolated individual SWCNTs has been proven to be highly challenging because the weak signal radiated by the nanotube is buried by the noise. It is only when the laser energy is in resonance with the SWCNT electronic transition energy that sharp spectrum peaks are observed [48]. Under the condition of resonance, an increase of the peak signals by three orders of magnitude has been reported [45].

## 1.5 Carbon Nanotube Synthesis

Three methods are commonly used to synthesize carbon nanotubes. They can be classified into two distinct categories depending on the temperature of synthesis. Arc-

discharge (AD) and laser ablation (LA) lie within the high temperature synthesis techniques, while chemical vapor deposition (CVD) is a lower temperature method.

### **1.5.1 Arc-Discharge Technique**

In this technique, an arc discharge is generated between two graphite electrodes in a chamber filled with either argon or helium. The temperature reaches 6000 °C causing the graphite to sublime (i.e. direct solid to gaseous state transition). The carbon atoms are ejected from the anode as plasma toward colder zones of the cathode where they accumulate. With this setup, this technique produced only MWCNTs and in his initial work, S. Ijima [2] used arc discharge to produce his nanotubes. SWCNTs can also be synthesized using this technique by adding transition metals such as Fe, Co and Ni to the hot spot (i.e. anode) [22].

### **1.5.2 Pulsed Laser Evaporation Technique**

This synthesis method is based on the same principle as AD that is, sublimation of graphite in a chamber filled with either argon or helium in order to form CNTs [22]. Here, the energy source is either a pulsed laser or continuous laser. The laser is used to evaporate a graphite target in a quartz tube in combination with gas flow that guides the evaporated carbon atom through the high temperature zone to a cooler region. This creates a temperature gradient inside the quartz tube that allows CNT formation. In a different configuration, a graphite target is placed vertically and heated to 3000-3500 K

with a focused laser hitting it directly. Inert gases such as He, Ar and N<sub>2</sub> sweep the product to a cooler zone in the quartz tube and formation of CNTs is then observed.

### 1.5.3 Catalytic Chemical Vapor Deposition

In catalytic chemical vapor deposition (c-CVD), carbon feedstock is decomposed at relatively high temperatures (usually < 900 °C) on a metal particle acting as a pyrolytic decomposition site. Over time, carbon atoms are assembled on the particle and formation of CNTs is observed. One major advantage of c-CVD over the two previous synthesis techniques is it provides better control over SWCNT growth. Moreover, c-CVD requires a lower temperature than both laser ablation and arc-discharge, which makes it compatible with conventional semiconductor processing. Many efforts have been devoted to understand the growth mechanism and the parameters for CNT growth via CVD, as described in the following sections.

#### 1.5.3.1 Carbon Nanotube Growth Model

The most accepted model states that in order for a SWCNT to grow, a transition metal catalyst acting as a seed is needed to assemble carbon fragments into a single graphite layer (Figure 1-15a[ii]). Typical transition metal catalysts used in CVD growth are Ni, Co, Fe or metal salts [50-54]. Mo has also been incorporated to some transition metals to form Fe-Mo and Co-Mo mixtures in order to enhance the CVD growth by stabilizing the catalyst particle [53]. It is energetically favorable for carbon atoms to form the graphene sheet and transform the metal catalyst into carbide [54]. As a direct

consequence, the metal particle (MP) becomes saturated with carbon atoms and formation of a graphene layer on top of the MP occurs (Figure 1-15a[iii]). This step is referred to as the incubation period [5, 55] (see Figure 1-16a section I) and depending on the CVD approach, it ranges from few seconds up to several minutes (Figure 1-16a and b). Once this period has passed and due to stress, a SWCNT nucleates from the graphene layer. The growth lasts as long as carbon atoms diffuse by concentration gradient from the catalyst surface to the SWCNT base [56] or as other theories state through nanotube walls [57] (Figure 1-15a[iv]). At this stage, depending on the strength of interactions between the metal particle and the support layer, the nanotube can either undergo a tip growth for weak interactions or base growth for strong interactions as shown in Figure 1-15b [53].

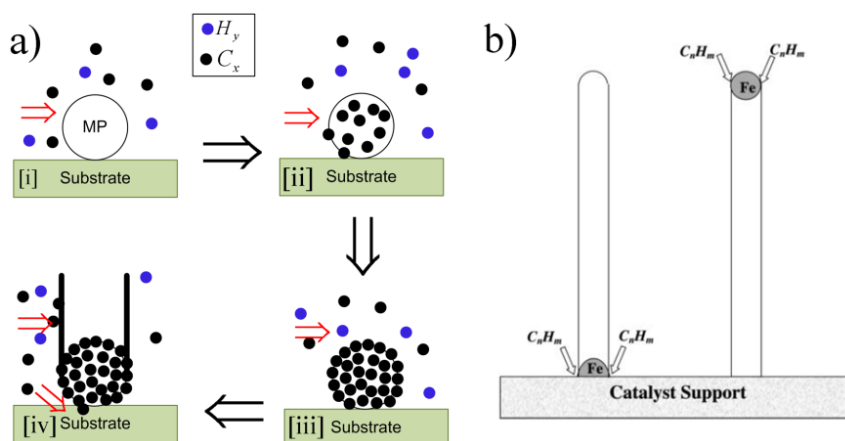


**Figure 1-15: a) Growth model of a SWCNT: [i] gas feedstock is decomposed into C and H atoms under high temperature, [ii] C atoms diffuse through the catalyst particle by concentration gradient, [iii] the metal particle becomes saturated, thus formation of carbide, and [iv] due to stress SWCNT nucleates from the carbide particle. b) Schematic of base growth mode (left nanotube) and tip growth mode (right nanotube) [28].**

However, this model alone does not explain the fact that most of the growth occurs during the first minutes and the growth is either considerably slowed or hindered

as depicted respectively in Figure 1-16a and b. In fact, during CNT growth the viscous forces caused by the surrounding hot gas [54], van der Waals interaction between adjacent CNTs or between surface-nanotube [58] oppose the extrusive force arising from the addition of carbon atoms at the base and/or walls of the nanotube. The CNT growth is then slowed or hindered when these force match up the extrusive force [54]. A more advanced investigation by Ogrin *et al.* [59] revealed that the growth rate is actually different for growth of CNTs parallel to the surface or out from the surface. In the first scenario, the nanotube is subject to all the forces stated above and consequently the growth rate drastically decreases over time. On the other hand, for nanotubes grown out from the surface, there are no surface-nanotube interactions and for isolated CNTs, the growth rate is unrestricted [59].

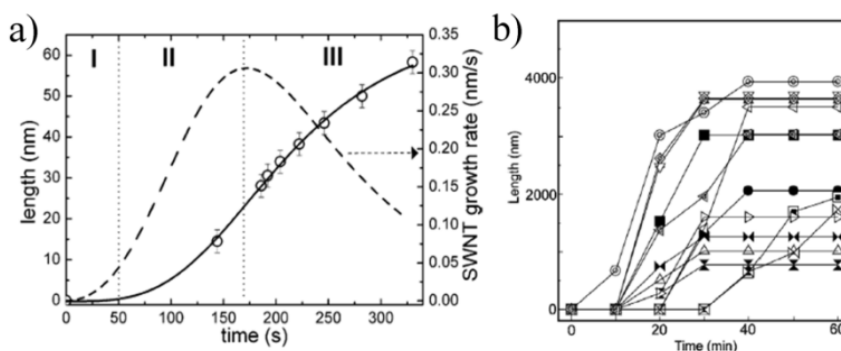


**Figure 1-16: Growth rate for SWCNTs synthesized using a) Ni-MgO catalyst particles subjected to  $C_2H_2$  gas [55]; sections I, II and III are respectively the incubation, growth and decay periods, and b) Co catalyst particles grown under ethanol vapor [5].**

### 1.5.3.2 Catalyst Particle Size and Support Layer

For SWCNT growth, the catalyst particles need to be less than 6 nm [60]. It has been shown that SWCNT diameters are directly correlated to catalyst particle size and thus many efforts have been devoted to ensure well dispersed catalysts during CVD

growth. In fact, at high temperature, the catalyst particles are free to move and form clusters with adjacent particles which hinder SWCNT growth. The choice of a support layer is critical as it prevents catalyst movement. With an appropriate support layer, catalyst coalescence at high temperature is unlikely. Dielectrics such as  $\text{Al}_2\text{O}_3$  or  $\text{SiO}_2$  are commonly used as a support layers. Their high surface roughness prevents catalyst movement and they are also catalytically inactive (i.e. they do not react with the metal catalyst itself to form alloys) [53, 61]. The wetting property of the support layers is another parameter that needs to be considered. Catalyst particles are more spherical on hydrophobic support layers but their sizes are often too large to promote SWCNT growth. Ideally, support layers with optimum wetting properties will yield good catalyst dispersion, while ensuring formation of catalyst particles in the range of SWCNT diameters [62]. It has been shown that SWCNT yield is strongly increased using  $\text{Al}_2\text{O}_3$  compared to  $\text{SiO}_2$  because it possesses higher surface roughness which indicates that the particle sizes is preserved [58]. Support layers also prevent diffusion of catalysts to the substrate layer and thus formation of silicide which poisons the catalyst particles and hinder nanotube growth. When growing CNTs on silica substrates, it has been shown by Simmons *et al.* [63] that the critical oxide thickness to avoid formation of silicide is 4 nm as displayed in Figure 1-17.

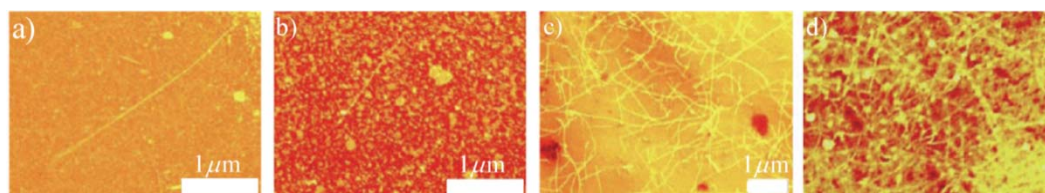


**Figure 1-17: SEM images of CNT growth from iron nitrate catalyst using a) clean silicon substrate, b) a 3 nm, c) a 4 nm, and d) a 8 nm layer of  $\text{SiO}_2$  (adapted from [63]). Growth is inhibited with oxide layer below 4 nm.**

### 1.5.3.3 Temperature and gas feedstock

Controlling carbon flux is crucial in preventing the poisoning of catalysts with excess amorphous carbon. Carbon residues are formed from dehydrogenation of the hydrocarbon molecules on the surface of the catalyst. Coatings of the catalysts by amorphous carbon reduce their activity and lifetime. Methane ( $\text{CH}_4$ ) and carbon monoxide (CO) [64] are usually the cleanest carbon feedstocks. For the gas feedstock used in the scope of this thesis,  $\text{CH}_4$  has a high activation energy and is consequently less prone to catalyst poisoning and growth defects. If desired, hydrogen can be added during the growth to prevent catalyst poisoning. Water was also reported [65] to selectively remove amorphous carbon without damaging the nanotubes. In many CNT growths processes a temperature of  $\sim 900$  °C is often used as it is a good compromise between the formation of the metal carbide, cleavage of the C-H bonds and formation of the C-C framework [53], although efficient CVD growth of SWCNTs/CNTs has been achieved for temperatures as low as 500 °C [62, 66].

## 1.6 Control of Carbon Nanotube Growth

Despite the potential of CNTs and the advance in the nanotube synthesis, many issues still have to be addressed before CNTs can be widely integrated in current electronics. Precise control of tube diameter and chirality along with length, position and orientation are difficult at present. Nevertheless, many efforts have been deployed to overcome these difficulties by either using patterned catalyst or simply the substrate

properties to guide CVD growth. External parameters such as gas flow and electric field have also been used to align CNTs.

### 1.6.1 Catalyst Patterning

Controlling CNT orientation involving predefined geometries of Fe salt catalyst were initially performed by Dai group [67-69]. They were able to pattern liquid catalyst islands using photolithography on Poly(methyl methacrylate) (PMMA) and alumina supported iron catalyst in methanol. Growth of SWCNTs with diameters ranging between 0.5-1.7 nm were achieved [69] as shown in Figure 1-18a. The growth however did not show any preferential alignment but instead some random SWCNTs connecting the catalyst islands. In addition, the yield compared to the amount of catalyst was fairly low. This group also used silicon pillars to pattern SWCNTs. The catalyst was made by dissolving  $\text{AlCl}_3$ , triblock copolymer, and iron and molybdenum chlorides in a mixed ethanol and butanol solution. This method achieved some degree of alignment as the majority of SWCNTs were suspended and not many were in contact with the substrate. Franklin *et al.* [67] stated that such alignment is due to the gas flow that keeps SWCNT bundles floating until they get in contact with the pillars in the vicinity as depicted in Figure 1-18b. Recently, some groups [70-73] were also able to use gas flow direction to orient SWCNTs on silica and silicon wafers in more than one direction by wafer rotation. This technique, however, cannot be used to pattern complex structures of SWCNTs.

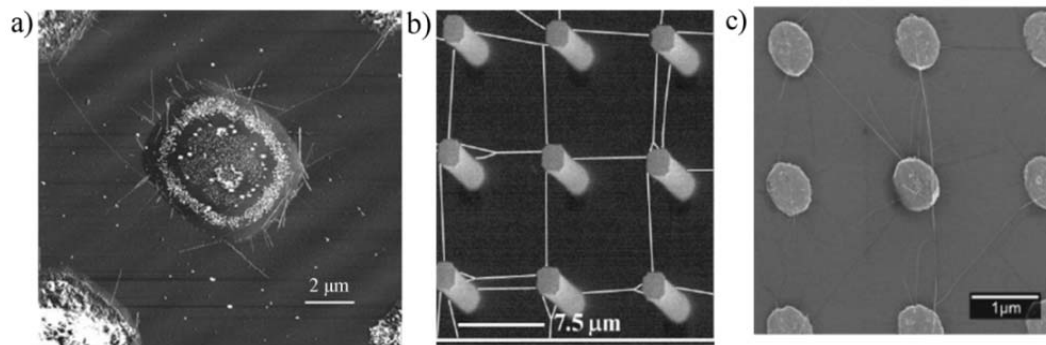


**Figure 1-18: SEM of a) liquid catalyst islands patterning for SWCNTs growth [68], b) SWCNTs grown on top of silicon pillars with the help of gas flow that keeps the nanotubes floating above the surface until they reach adjacent pillars [67], and c) SWCNTs grown from Al/Fe/Mo catalyst islands [74].**

Other types of catalysts have also been used to promote alignment of SWCNTs during CVD growth. Wang *et al.* [75] used photolithography to pattern thin Ni square dots of 2.5  $\mu\text{m}$  on  $\text{SiO}_2/\text{Si}$ . Results showed only bundles of MWCNTs with no preferential alignment. Lacerda *et al.* [74] employed a triple layer catalyst composed of Al/Fe/Mo and a lithography step to pattern dot arrays. The growth was performed using CVD of acetylene. SWCNTs with a diameter of  $\sim 1.3$  nm and a length in the range of 5-10  $\mu\text{m}$  were obtained (Figure 1-18c). In this study, some nanotubes were able to bridge between two catalyst dots. Seidel *et al.* [76] used a multilayer of Ti/Au/Al/Co to pattern the both metals catalyst and the electrodes. SWCNTs connecting two separated catalyst strips were achieved.

### 1.6.2 Substrate surface

It was thought that in order to grow long and aligned nanotubes one should minimize van der Waals interactions between the nanotubes and the surface as it hinders

the growth. However many results were obtained where researchers took advantage of substrates and SWCNTs interactions to influence growth orientation. Strong interaction between the substrates and the nanotubes can align the SWCNTs along specific crystalline directions [77-81]. The first attempt [77, 79] was made using a sapphire ( $\text{Al}_2\text{O}_3$ ) wafer soaked in a liquid solution of cationized ferritin. The sample was oxidized at a high temperature in order to remove the organic outer shell of ferritin leaving an iron core catalyst of about 4 nm in diameter. This step was followed by CVD in mixtures of  $\text{CH}_4$  and  $\text{H}_2$ . Results showed alignment of SWCNTs along the crystal lattice of the substrate over long distance as depicted in Figure 1-19a. Such a strong alignment of SWCNTs on sapphire has been attributed to the creation of Al-O dipoles moment due to oxygen depletion at the surface of the substrate [79].

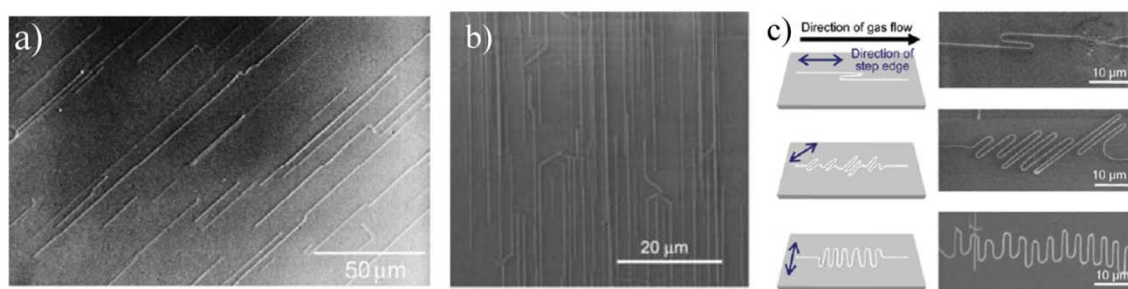


**Figure 1-19:** SWCNTs aligned on a) sapphire, nanotubes direction is affected by the atomic arrangement of the substrate [77], b) on quartz, SWCNTs are aligned along the atomic steps [82], and c) on quartz, combination of gas flow and atomic steps are used to align SWCNTs [83].

Similar results were obtained using ferritin and metal nanoparticles on quartz substrates [82-85] (see Figure 1-20b). Kocabas *et al.* [82] found that SWCNT alignment on quartz is directly correlated to substrate surface morphology. Atomic steps of 0.7 to 1 nm in height were reported on quartz surface [82]. In a more complex approach,

combination of quartz atomic steps and gas flow was used to obtain serpentine-like alignment [83, 85-87] (Figure 1-19c).

### 1.6.3 Electric Field

Electric fields have also been widely used to control SWCNT growth. Ural *et al.* [88] employed alumina supported Fe/Mo on Mo electrodes to control the orientation of SWCNTs during growth. Electrodes were patterned on a SiO<sub>2</sub> surface using photolithography and e-beam evaporation. An electrical field was generated between the Mo electrodes by biasing them at 10 V during the CVD process. Results revealed that in the presence of electric fields, aligned SWCNTs are able to grow from one electrode to the adjacent electrodes at 10 μm apart [88]. Nojeh *et al.* [89] confirmed that SWCNTs tend to orient along intense electric fields (Figure 1-20a). Direct current electric field was also used by Zhang *et al.* [90] to align SWCNTs grown between poly-silicon electrodes on top of a quartz substrate (Figure 1-20b).

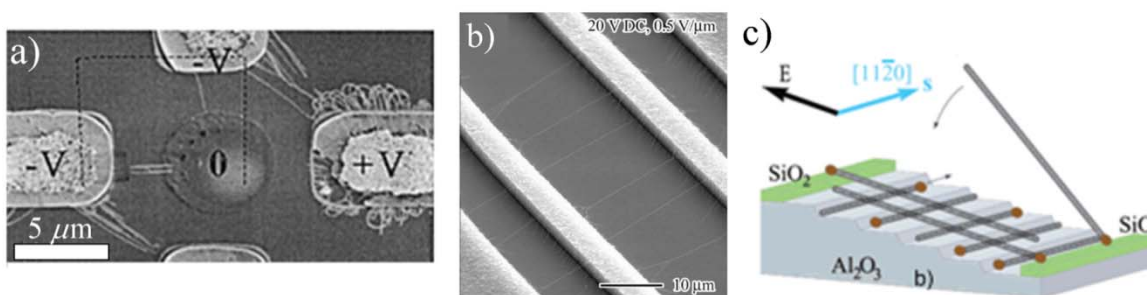


**Figure 1-20: Preferential alignment of SWCNTs a)-b) along intense electric field [89, 90], and c) orthogonal alignment using electric field and substrate surface [91].**

Ismach *et al.* [91] combined both electric field and substrate atomic arrangement to align SWCNTs in a orthogonal patterns using ferritin catalyst (Figure 1-20c). Sapphire

was used as a template to align nanotubes in one direction while an electric field was used to bridge nanotubes orthogonally between two gold islands. These results showed that nanotubes interacting with the dipole moments of sapphire are unaffected by the external electric field. Consequently, the authors concluded that the alignment is due to a strong interaction between nanotubes and the sapphire surface [91].

## **1.7 Carbon Nanotube Electronic Devices**

### **1.7.1 Carbon Nanotube Field-Effect Transistor**

The unique electronic properties of SWCNTs have propelled a great amount of interests from the electronic world. The first CNT field-effect transistors (CNTFETs) were reported separately in 1998 by Martel *et al.* [92] from IBM (Figure 1-21a) and Tans *et al.* [93] (Figure 1-21b). The design of the first CNTFETs was quite simple: i) gold [92] or platinum [93] electrodes serving as sources and drains patterned on top of Si/SiO<sub>2</sub> wafers, ii) CNT solution synthesized by laser ablation were dispersed on top of the electrodes, and iii) the underlying heavily doped silicon was used as a gate. Electrical measurements on these devices displayed in Figure 1-21c and d showed clear p-type transistor action and a modulation of the conductance by more than five orders of magnitude by varying the gate voltage [92, 93]. More specifically, Martel *et al.* reported transconductance and hole mobility of 1.73 nS and 20 cm<sup>2</sup>/V s, respectively. The total resistance between source and drain of the back-gate geometry was estimated at several MΩ due to the contact resistance. This problem arises from the weak van der Waals coupling between the nanotube and the electrodes.

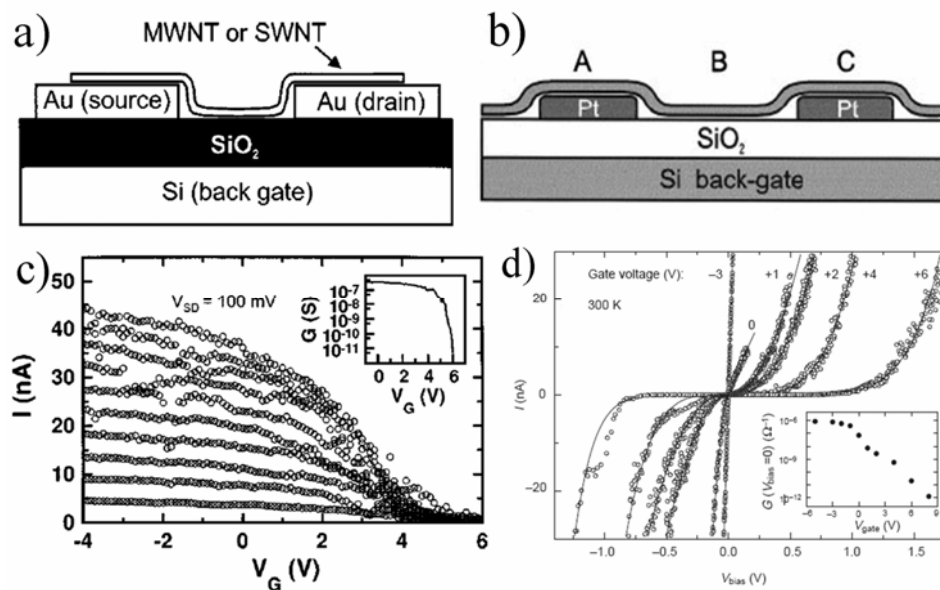


**Figure 1-21: Schematic of the firsts back-gate CNTFETs using a) gold [92] and b) platinum as electrodes [93]. Electrical measurements of the CNTFETs proposed by c) Martel *et al.* [92] and d) Tans *et al.* [93], showing a clear p-type behavior and an on/off ratio between five and six order of magnitude.**

Enhancement of the contact resistance and thus the conductance of the CNTFETs was achieved a year later by Kong *et al.* [69] in 1999 (Figure 1-22a). They used their island catalyst technique to build a SWCNT field-effect transistor. In this approach, electrodes of Ti/Au (15/60 nm) were deposited on top of the islands. The silicon substrate was used as a back-gate (Figure 1-22). *I-V* measurements showed a strong p-type semiconducting field-effect transistor. In contrast with the van der Waals connected CNTFET, contact resistance has been drastically decreased from several M $\Omega$  to  $\sim$ k $\Omega$  as reported in Figure 1-22b. Notable increases in the device performance were also observed by Franklin *et al.* [94] with a transconductance of 90 nS and carrier mobility of 10 000 cm<sup>2</sup>/V s [94].

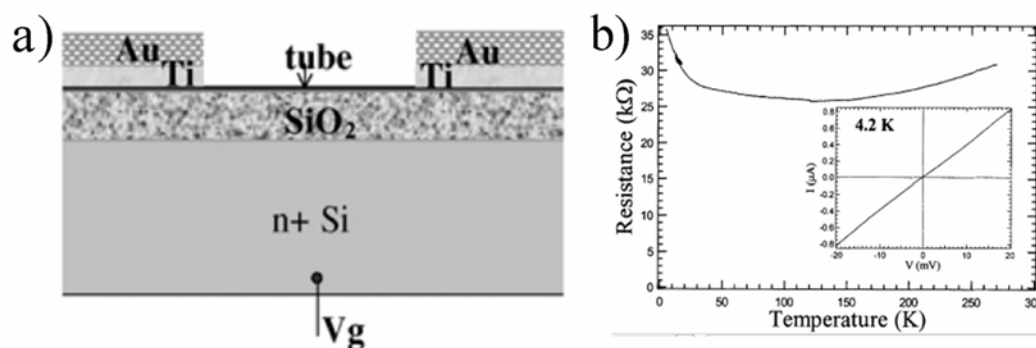


**Figure 1-22: a) Schematic of a on-surface SWCNT-FET [69], and b) typical measured resistance at various temperature and  $I$ - $V$  curve for SWCNT-FET with enhanced contact resistance [94].**

Despite all these promising results, the back-gate design suffered some major drawbacks that make it less attractive for advanced electronic integration. The thick gate dielectric (100 nm or more) requires fairly high gate voltages for channel modulation. A further disadvantage is the idea of using the underneath substrate as a gate, which implies that the transistors cannot be turned on/off independently. To confront these issues, a top-gate CNTFET design has been proposed by Wind *et al.* [95] in 2002 (Figure 1-23a). In this approach, Ti electrodes were patterned at each end of the nanotube using e-beam lithography and liftoff. A further enhancement of contact resistance was obtained by heating the sample at 850 °C for 100 s to form titanium carbide (TiC) at the nanotube-contact junctions. Subsequently, a Ti or Al gate was deposited on a thin film of oxide (~15 nm in thickness) on top of the CNT and Ti layers.

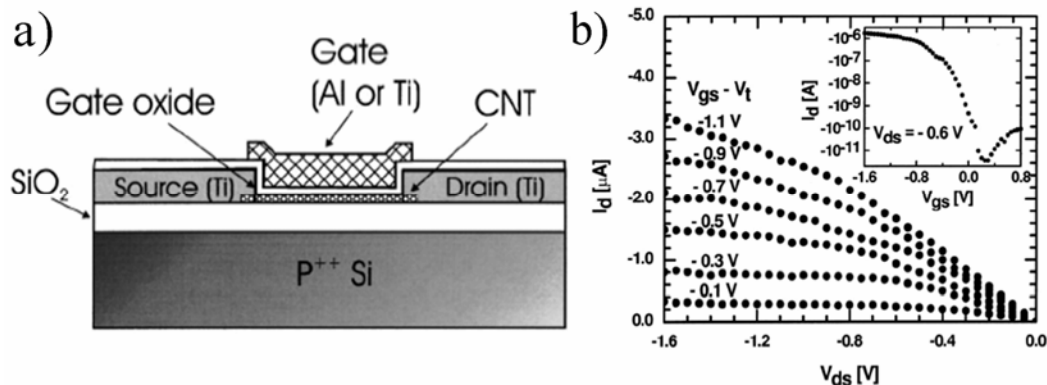


**Figure 1-23: a) Schematic of a top-gate SWCNT-FET proposed by Wind et al. [95] and b) its I-V measurements showing a p-type transistor action and a low gate voltage operation.**

As expected,  $I$ - $V$  characterizations revealed a strong p-type transistor behavior as one can notice in Figure 1-23b. In comparison to previous CNTFET devices, top-gate design significantly increases device performance. As an example, the gate voltage is much lower than the previous design owing to a thinner gate oxide layer. The maximum transconductance was also measured to be 3.25  $\mu\text{S}$ , which is extremely high for CNTFETs at that time [95].

### 1.7.2 Effects of Metal Contacts on Carbon Nanotube Field-Effect Transistors

When a SWCNT is connected to a metal electrode, two types of barriers that affect device performance are created: i) interface contact barriers due to imperfect interfaces between the metal and the CNTs [96], and ii) Schottky barriers caused by band alignment at the interface of metal-semiconducting tubes [42]. Metals such as Ti, Au and Pd have been shown to make the best contact due to their ability to easily wet CNT walls [96]. However, the presence of a Schottky barrier at the nanotube-contact junction has been observed in most of the CNTFET devices [42] and ohmic contacts have only been

achieved using Pd for tube diameters greater than 1.5 nm. For nanotubes with diameters less than 1.5 nm, systematic Schottky barriers have been observed [42] (Figure 1-24).

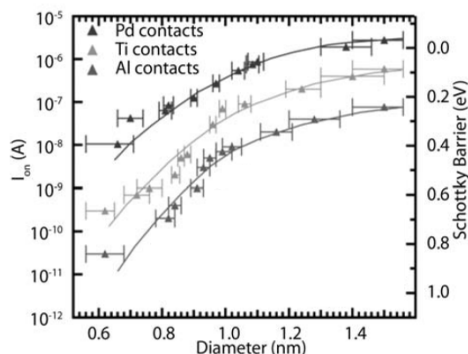


**Figure 1-24: Schottky barrier height and on-state current versus single-walled carbon nanotube diameters [42]. Curves from top to bottom correspond respectively to Pd, Ti and Al contacts.**

For one dimensional structures such as SWCNTs, the Schottky barrier width is very thin and thus tunneling of carriers are often possible [97, 98]. For this reason, early CNTFETs exhibit primarily ambipolar behaviors [97, 98] (Figure 1-25): at negative gate voltages holes are injected into the valence band (Figure 1-25a), while at positive gate voltages electrons are injected into the conduction band (Figure 1-25b). Typical  $I$ - $V$  curves for an ambipolar Schottky barrier CNTFETs are seen in Figure 1-25c.

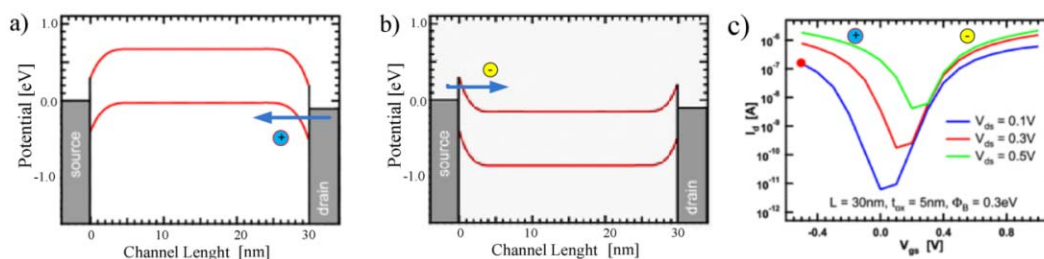


**Figure 1-25: Band alignment of a Schottky barrier CNTFET showing: a) hole tunneling at negative gate voltages, b) electron tunneling at positive gate voltages, and c)  $I$ - $V$  measurements of a Schottky barrier CNTFET exhibiting a strong ambipolar behavior.**

Recently, a new CNTFET design called conventional CNTFET (cCNTFET) has been proposed to tackle the problem of ambipolar CNTFETs and to give devices characteristic that are more unipolar [97, 98]. Tunneling phenomenon in 1D structures has also been exploited by Appenzeller *et al.* [97] to make CNTFET devices based on band to band tunneling (tCNTFET) in which conduction of high energy carriers is prevented [98].

### 1.7.3 Beyond Carbon Nanotube Field-Effect Transistors

The ability to make p-type and n-type CNTFETs opened up the way for the first carbon nanotube CMOS circuit. In their work, Derycke *et al.* [99] transformed an originally p-type SWCNT into a n-type by either using vacuum annealing at 400 °C or doping with potassium.  $I$ - $V$  characterizations of the nanotube subjected to the two methods show a drastic change of the CNTFET behavior as shown in Figure 1-26a and b.

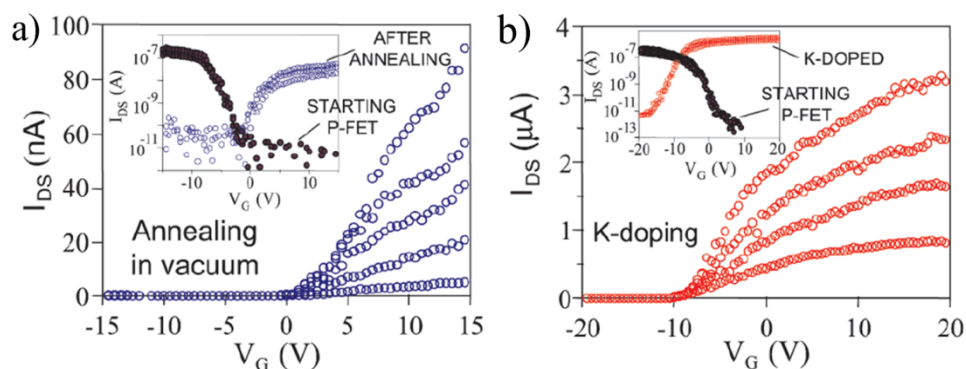


**Figure 1-26:**  $I$ - $V$  measurements of a n-type CNTFET made by a) annealing the initial p-type nanotube in vacuum at 400 °C, and b) doping the initial p-type nanotube with potassium [99].

This CNT type modification concept was used to create the first intramolecular inverter (logic NOT gate) in 2001 [99]. Once the n-type transformation was achieved,

PMMA was used to protect half of the nanotube from a subsequent step of oxygen or air exposure. This transforms the unprotected half to p-type, while the other half retained its n-type behavior as shown in Figure 1-27a.

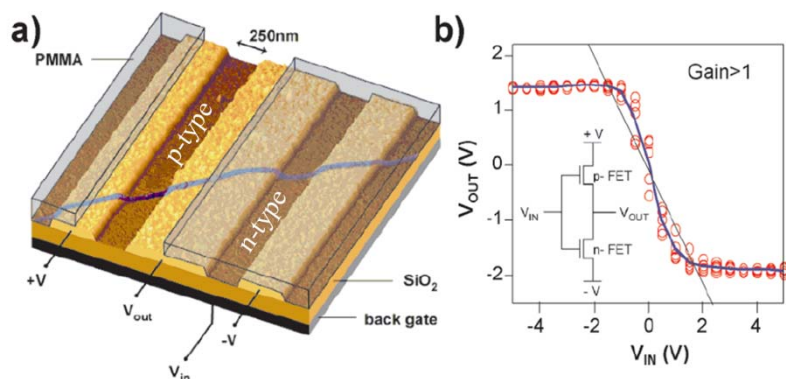


**Figure 1-27: a) Schematic of the first intramolecular inverter using p- and n-type SWCNT (adapted from [99]), and b) electrical behavior of the devices at  $V = \pm 2$  V [99].**

The highly doped silicon substrate was used as a back-gate for the input signal, while, simultaneous bias voltages of opposite signs were applied at the input of the p- and n-type SWCNT as depicted in Figure 1-27a. The common contact output shows a typical CMOS inverter behavior that is: at negative input voltages the p-type device is ON resulting in the transmission of the positive bias voltage, while at positive input voltages, the n-type is ON and the negative bias voltage is transmitted (Figure 1-27b).

Optoelectronic devices using SWCNTs have also been demonstrated by Freitag *et al.* [100] (Figure 1-28a). They used the unique characteristics of Schottky barrier CNTFETs as hole-electron gate dependant devices, to inject simultaneous electrons and holes respectively in the conduction and valence band. It was achieved by grounding the source electrode and setting  $V_g = V_d / 2$  [100, 101]. This biasing configuration results in equal but opposite signs gate-induced fields at the source and drain electrodes. By

sweeping the gate voltage, Freitag *et al.* were able to control the location of holes-electrons recombination and thus the position of the infrared emission along the SWCNT as shown in Figure 1-28b.

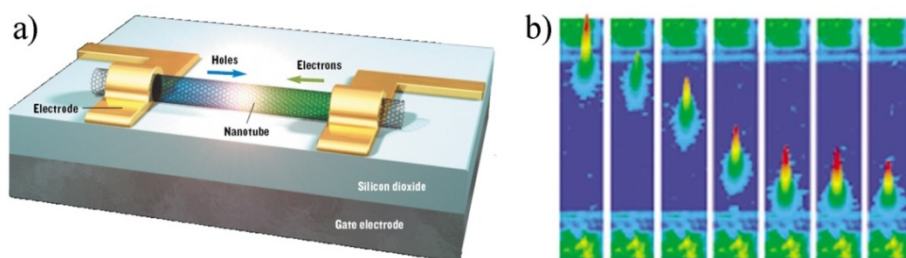


**Figure 1-28: Schematic of the optoelectronic device using a Schottky barrier CNTFET [102], and 2D map of the infrared emission for different gate voltage values. (adapted from [100])**

Another way carbon nanotubes have been integrated into electronic devices includes the creation of metal-semiconducting junctions. For example, Yao *et al.* [103] employed atomic defects in SWCNTs to make metal-semiconducting junctions. A pentagon-heptagon (5-7) defect in a nanotubes leads to a  $40^\circ$  kink (Figure 1-29a and b). The voltage across this kink was reported to be highly nonlinear with a rectifying diode-like behavior as shown in Figure 1-29c.

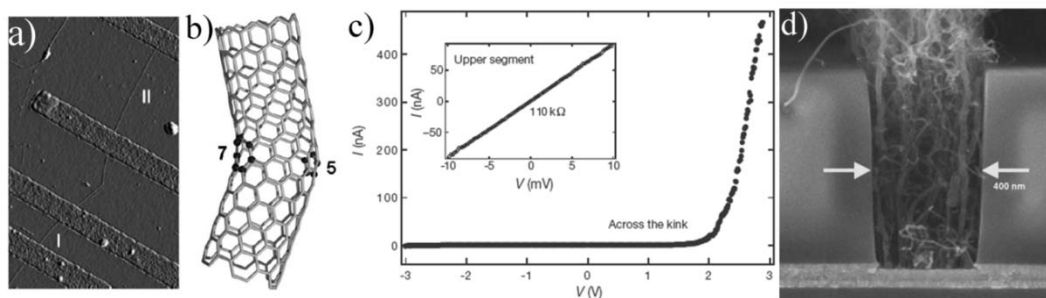


**Figure 1-29: a) Atomic force microscopy and b) schematic of nanotube junction [103], c)  $I$ - $V$  measurement of the nanotube junction showing rectification behavior [103], and d) MWCNT interconnect between two metal conductors [6]. Inset in c) is the  $I$ - $V$  characterization of the metallic part in of the nanotube.**

As traditional copper interconnect width decreases, a drastic increase in resistivity due to surface roughness and grain boundary is expected [104]. Therefore, metallic CNTs are seen as the ideal future interconnects due to their large conductivity and current carrying capability of  $>10^9$  A/cm<sup>2</sup> [105]. However, due to their intrinsic resistance of 6.5 k $\Omega$  individual metallic SWCNTs cannot be used alone as interconnects and thus bundles and ropes of metallic SWCNTs in parallel should be used as interconnects [104]. On the other hand, MWCNTs can have metallic shells and are often proposed as interconnects [6].

## **1.8 Scope of the Research and Thesis Outline**

Despite the fact that much progress has been made during the last decade in understanding carbon nanotube growth mechanisms and in controlling nanotube orientation through the use of different techniques, many problems still need to be addressed. Up to now, it remains highly challenging to precisely control nanotube orientation on Si and Si/SiO<sub>2</sub> even when using an external electric field or gas flow. In addition, controlling carbon nanotube location, catalyst geometry and its effect on periodicity of the nanotube location and orientation have not been fully understood. This thesis investigates and develops new techniques for the controlled growth and assembly of carbon nanotubes as a way to address some of these challenges.

In chapter 2, we demonstrate a new approach for SWCNT catalyst patterning. Colloidal lithography is employed to achieve large arrays of SWCNT catalysts on Si and Si/SiO<sub>2</sub> substrates. Catalyst size and geometry can be easily varied by changing colloidal

mask parameters such as nanosphere sizes and annealing time. Following growth, aligned SWCNTs on undoped Si substrates were observed within the hexagonal catalyst array, while on Si/SiO<sub>2</sub>, SWCNTs connect the catalyst islands. Colloidal lithography for carbon nanotube growth is an inexpensive and rapid process for reliably patterning periodic and nanoscale catalyst islands as required for future nanoelectronics.

In chapter 3, we present a novel patterning method that consists of direct-writing liquid catalyst via nanopipettes. Complex catalyst geometries at the nanoscale level using this method have been achieved on both Si and Si/SiO<sub>2</sub> substrates. Post-growth characterizations of Al<sub>2</sub>O<sub>3</sub>-FeMo and cationized ferritin catalyst samples show SWCNTs in the patterned regions. To show the versatility of the nanowriting approach, we also explored direct patterning of SWCNTs and C<sub>60</sub> molecules on Si and Si/SiO<sub>2</sub> substrates. Nanowriting is an effective method for the direct-writing of carbon nanotube catalysts and other nanostructures. Such precise control over the shape and location of the patterns makes it useful for nanoelectronic devices.

In chapter 4, we present a brief survey on CNTFET modeling techniques, followed by numerical calculations of single SWCNT channels. Two-terminal *I-V* measurements on post-growth colloidal lithography and nanowriting samples were performed. Based on the numerical and experimental data, device performance has been attributed primarily to the contact resistance that includes Schottky barrier resistances and an interface resistance. Electronic transport results on colloidal lithography and nanowriting samples show the efficiency of these techniques for CNT device fabrication.

Finally, chapter 5 concludes the thesis and presents some directions and recommendations for future research. This research has led to contributions in SWCNT patterning using colloidal lithography [106, 107] and nanowriting [108-110]. Indirectly, patterning of SWCNT ring arrays using colloidal lithography has also been demonstrated [111, 112].

## 2 Colloidal Lithography for Carbon Nanotube Catalyst Patterning

In this chapter, we present a new technique for single-walled carbon nanotube catalyst patterning. Colloidal lithography is introduced as a way of patterning large areas of metal catalysts with high periodicity and reliable control over the catalyst size [106, 107]. This method allows us to investigate the effects of catalyst size, geometry and distribution on nanotube growth.

### 2.1 Overview of Colloidal Lithography

Periodic arrays of nanoparticles have become of great interest in applications such as biosensors, chemical sensors and optical devices [113]. The most common way to fabricate these nanostructures is via electron beam lithography and focused ion beam lithography due to their excellent control over size, shape and spacing of the array [113]. However, these techniques are typically expensive and the fabrication process is often serial in nature which makes them inadequate for large scale fabrication. An alternative approach that is parallel in nature and based on a bottom-up approach has been used for nanostructure fabrication: colloidal lithography (CL) [113-121] makes use of polystyrene,

silica, noble-metal or semiconductor nanospheres [114], acting as a shadow mask during metal evaporation for patterning large two-dimensional areas of periodic nanostructures.

The basic concept of CL is based on the way nanospheres self-assemble in close-packed hexagonal arrays [113-122] upon drying on substrates (Figure 2-1). This leaves small openings between the nanospheres that can be used to deposit nanoscale amount of metal catalyst between the colloidal spheres. The self-assembly behavior of colloidal spheres has been attributed to the combination of the following forces: i) capillary force caused by the surrounded liquid [114, 121, 122], ii) friction force due to nanospheres-substrate interaction [114], and iii) Lennard-Jones potential related to the combination of repulsive and van der Waals interactions between adjacent spheres [114, 121]. The spring model proposed by Jarai-Szabo *et al.* [114] and based on the interaction of these three forces predicted that the self-assembly behavior of the nanospheres and the shape of the resulting layer are influenced by the substrate type and the evaporating liquid as they are directly responsible for the friction and capillary force respectively.

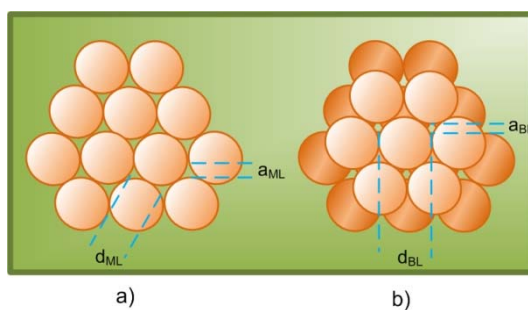


**Figure 2-1: Schematic of nanosphere self-assembly into hexagonal close packed arrays: a) monolayer and b) bilayer of colloidal spheres. Parameters  $a_{xx}$  and  $d_{xx}$  are respectively the size of the opening and the distance between two adjacent openings, whereas subscript  $xx$  refers either to monolayer (ML) or bilayer (BL) of colloidal spheres.**

It should be noted that only monolayers (MLs) and bilayers (BLs) are useful for surface patterning while higher layer ordering prevents the evaporated metal from reaching the substrate. Upon nanosphere removal, by sonication in solvents and/or dissolution in dichloromethane ( $\text{CH}_2\text{Cl}_2$ ) [118, 123], the substrate is left with either triangular nanostructures in the case of monolayers or hexagonal nanostructures for bilayers [123] as depicted in Figure 2-1. Hulteen *et al.* [123] gave a detailed characterization of these nanostructure sizes as a function of colloidal sphere diameters ( $D$ ). The distance between each triangular nanostructure in a monolayer is given by  $d_{\text{ML}} = 0.577D$  and their size is  $a_{\text{ML}} = 0.233D$ , while for bilayers, the distance between each hexagonal nanostructure is given by  $d_{\text{BL}} = D$  and their size is  $a_{\text{BL}} = 0.155D$ . Based on these results, the opening size of the colloidal mask can be controlled by changing the size of the nanospheres, which makes it a tunable shadow mask.

Polystyrene spheres are sensitive to heat treatments. Consequently, the annealing of polystyrene colloidal mask prior to metal evaporation has also been widely used to control nanostructure sizes. In their work, Kosiorek *et al.* [115] investigated the behavior of polystyrene nanospheres of 540 nm in diameter when subjected to annealing via microwave pulses. Results depicted in Figure 2-2a show that the opening size of the shadow mask decreases from the initial value of 200 nm down to 25 nm. Colloidal lithography can also be used to pattern more complex geometries by combining annealing time/temperature and evaporation angle. By varying these parameters, Kosiorek *et al.* [115] were able to demonstrate a wide variety of geometries as reported in Figure 2-2b

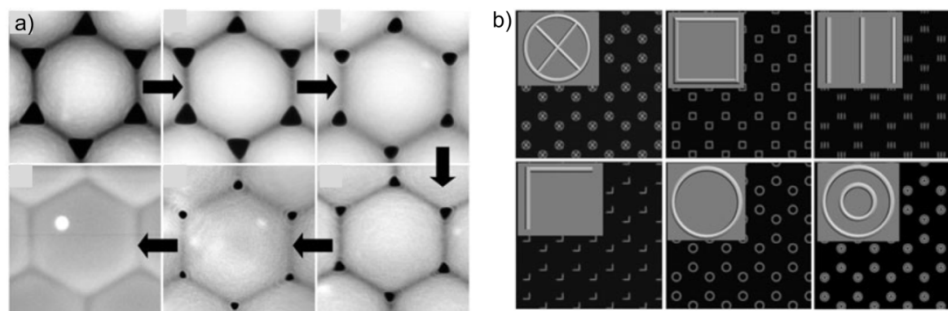


**Figure 2-2: Scanning electron microscopy of a) the effect of annealing on a colloidal mask using nanospheres of 540 nm in diameter; the initial opening size of 200 nm is decreased down to 25 nm upon annealing, and b) possible structure geometries obtained using different evaporation conditions and an annealed polystyrene mask [115].**

Colloidal lithography has some advantages over conventional lithographic processes such as electron-beam lithography and photolithography for patterning large areas of nanoscale metal catalyst. Colloidal polystyrene spheres cost approximately \$10.5 /ml [124] and since a minute amount of solution is needed, it can be far cheaper than lithography masks. Additionally, it does not require any complex process and therefore the mask formation is straightforward and fast. In the following section, we propose a new technique based on colloidal lithography for patterning large and periodic arrays of catalyst islands in order to create preferential aligned SWCNTs [106, 107]. The process used in the scope of this thesis is depicted in Figure 2-3 and each step will be discussed in detail in the following sections.

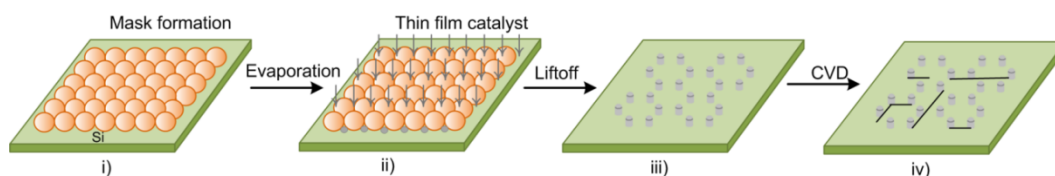


**Figure 2-3: Schematic of SWCNT patterning process using polystyrene nanospheres: i) mask formation using colloidal spheres, ii) evaporation of a thin metal catalyst layer, iii) sphere removal, and iv) SWCNT growth via CVD.**

## 2.2 Mask Formation

450 nm polystyrene nanospheres in aqueous suspension were purchased from Interfacial Dynamics Corporation (surfactant-free white carboxyl latex). Due to the poor wetting properties of aqueous solution on Si and Si/SiO<sub>2</sub> which causes aggregation and multilayer formations, nanospheres suspension was not directly used on these substrates. Consequently, mask formations were made by dropping 1-3  $\mu$ L of nanosphere suspension on a freshly cleaved mica substrate as the wetting properties of this material are high [125, 126]. The mica sample was then allowed to dry at room temperature followed by immersion in DI water. This causes the monolayer to strip off of the mica surface and to remain at the water surface [127]. Afterwards, the transfer of the colloidal mask was achieved by placing the desired substrate in contact with the water surface. It should be noted that all the substrates used in the scope of this thesis are (100) Si (undoped, Silicon Quest International, Inc.) and/or Si/SiO<sub>2</sub> (undoped, 1  $\mu$ m thermal oxide, Silicon Valley Microelectronics, Inc.). No effort was made to remove the native oxide layer from the Si wafer.

At this stage the colloidal mask on Si or Si/SiO<sub>2</sub> substrate was either used as it was or placed in a glass Pyrex dish and annealed in a convection oven at 105 °C for 100-700 minutes in order to control the opening size [116]. Typical results of a hexagonal array obtained with 450 nm diameter colloidal spheres using this approach before and after annealing are depicted in the SEM characterization in Figure 2-4.

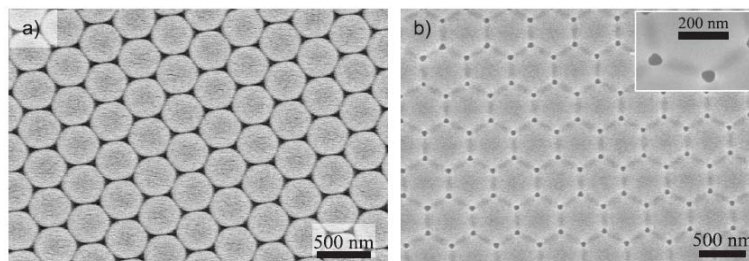


**Figure 2-4: Scanning electron microscope characterization of a colloidal mask [116] a) before and b) after annealing at 105 °C for 300 minutes.**

### 2.3 Catalyst Composition

Once the colloidal mask was made, the next step consists of evaporating a thin film of metal catalysts on top of the shadow mask. The catalyst composition and thickness were chosen carefully as growth can easily be hindered [57, 76, 128-130]. Typical metal catalysts for SWCNTs are Fe, Ni and Co as their respective  $d$  orbitals have the right symmetry to overlap with graphene lattice [54]. Compared to Ni and Fe, Co can give SWCNTs with better quality. Henardi *et al.* [131] found that the graphitization and structures of nanotubes were much better with Co than Fe even if the latter gives much higher yield. It should be noted that the growth temperature for these three metals was in agreement with the order of the melting temperature of the bulk material (Ni = 1450 °C; Co = 1490 °C and Fe = 1540 °C). However, typical SWCNT growths were done at temperatures much lower than the bulk material melting point. Theoretical calculations and experimental works have shown that for nanoparticles, the melting point decreases considerably compared to bulk material [53]. The lower melting point of Ni causes the atoms to diffuse easily and coalesce into clusters which explain the typical low SWCNT yield of this metal [57]. More recently, Yuan *et al.* [84] stated that less common metals

such as Au, Pt, Pd, Cu, Mn, Mo, Cr and Sn can also promote SWCNT growth on quartz substrates.

During CVD, the geometry of the thin film of metal catalyst changes considerably from the initial state. During the preheating step that consists of heating the sample from room temperature up to the 600-900 °C under H<sub>2</sub>, the oxidized metal catalyst obtained after evaporation is reduced and breaks into small particles that would eventually promote SWCNTs. This time sensitive step [132] is primordial for CNT growth as it activates the particle and allows the assembly of carbon fragments on the surface of the metal nanoparticles. Ideally, one expects the size of these nanoparticles to be identical to the diameter of SWCNTs (i.e. ~1-2 nm). However due to poor surface interaction, these particles can freely move and form bigger clusters that inhibit SWCNT. In their work, Seidel *et al.* [132] showed that during the CVD growth, the initial thin catalyst films of Co break into smaller particles and due to lack of surface interaction, SWCNT growth was inhibited (Figure 2-5a and b). The same observations were reported by Yoon *et al.* [130] during the reduction step for Co directly deposited on top of substrates.

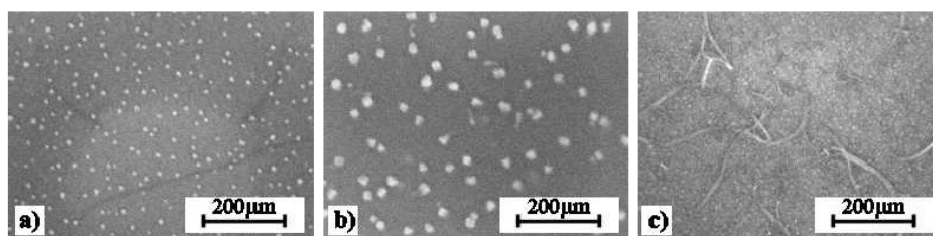


**Figure 2-5: Scanning electron microscope images of the influence of Al support layer and temperature on SWCNT growth: a) Si/ 200 nm SiO<sub>2</sub>/ 0.5 nm Co at 750 °C; preheating 2 min under H<sub>2</sub>; growth at 0.5 bar CH<sub>4</sub>; b) Si/ 200 nm SiO<sub>2</sub>/ 0.5 nm Co at 800 °C; preheating 2 min H<sub>2</sub>; growth at 0.5 bar CH<sub>4</sub>, and c) Si/ 200 nm SiO<sub>2</sub>/ 5 nm Al/ 0.5 nm Co at 750 °C; preheating 2 min H<sub>2</sub>; growth 0.5 bar CH<sub>4</sub> [132].**

In order to prevent catalyst movement and thus formation of large catalyst clusters that would eventually inhibit SWCNT growth, a support layer is usually added underneath the thin film metal catalyst. The roughness of the support is the predominant factor that influences the SWCNT growth. Typically,  $\text{SiO}_2$  or an evaporated thin film of Al is used as a support layer. It should be noted that in the latter case, the surface of Al is actually transformed into  $\text{Al}_2\text{O}_3$  upon interaction with ambient air. This has been confirmed by Zhang *et al.* [128] using X-ray photoelectron spectroscopy to report formation of thermally stable  $\text{Al}_2\text{O}_3$ . They attribute the transformation of Al into  $\text{Al}_2\text{O}_3$  to the absorption of residual oxygen molecules inside the furnace and/or from the underneath  $\text{SiO}_2$  layer. It is well known that this dielectric is stable and will retain its composition under CVD [53]. For CVD using Al as support layer, results reported by Seidel *et al.* [132] in Figure 2-5c show no clustering of catalyst particles and a clear growth of SWCNTs. Furthermore, support layers have also the purpose of blocking the catalysts from diffusing to the substrate and consequently causing silicide formation.

Based on these previous observations, we employed multilayer of catalyst composed of Ti/Au/Al/Co (5/50/10/~1 nm) as depicted in Figure 2-6a. This thin multilayer film was evaporated through the opening of a colloidal mask using an e-beam evaporator at the Advanced Materials and Process Engineering Laboratory at UBC (AMPEL-UBC). In this configuration, cobalt acts as catalyst layer for SWCNT growth, while aluminum is used as a support layer for Co, preventing it from diffusing into the underlying layers and causing catalyst poisoning. It has been shown that Co of ~1 nm gives the right range of nanoparticle diameters for SWCNT growth [132]. Precise control

over the catalyst thickness is thus crucial during the evaporation step. Regarding, the additional catalytically inactive Au and Ti layers, they are not for SWCNT growth but are rather useful respectively as electrodes and adhesion layers. During chemical vapor deposition, the two top layers composed of the catalyst and support layer will be transformed respectively to nanoparticles and small droplets [128] as depicted in Figure 2-6b and c. As long as the catalyst thickness is in the range of 1 nm, the nanoparticles size will be in the range of SWCNT diameters. The preheating step as discussed previously will have a direct effect of the size of the droplets [57, 76].

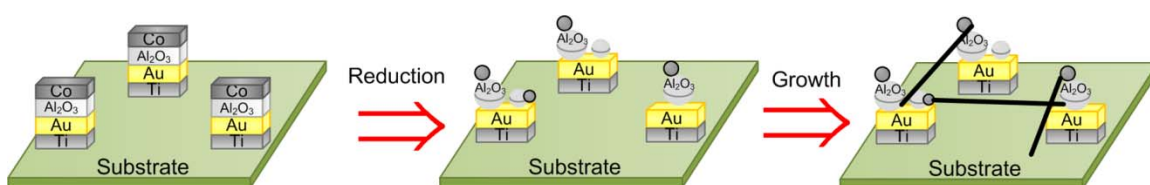


**Figure 2-6: Schematic of the catalyst multilayer composed of Ti/Au/Al/Co a) as evaporated, b) after the reduction step the active catalyst and support layer are transformed into smaller particles and c) growth of SWCNTs.**

Once the evaporation of the multilayer catalyst film is completed, colloidal sphere removal is performed by either sonication of the sample in dichloromethane ( $\text{CH}_2\text{Cl}_2$ ) or ethanol ( $\text{C}_2\text{H}_5\text{OH}$ ). This step should be done carefully as  $\text{CH}_2\text{Cl}_2$  is known to chemically etch polystyrene spheres and consequently low sonication power and time is recommended, whereas  $\text{C}_2\text{H}_5\text{OH}$  does not chemically attack polystyrene and higher power and/or time can be used. Sonication power should also be selected according to the quality of the multilayer catalyst adhesion to the substrate since poor adhesion and high sonication power will cause liftoff of the catalyst layer during mask removal. Once this

step completed, the sample is left with hexagonal arrays of catalyst particles (c.f. Figure 2-3iii).

## 2.4 Single-Walled Carbon Nanotube Growth

Growth of SWCNTs from the hexagonal arrays of multilayer catalyst particles is done via chemical vapor deposition using a tube furnace operating at atmospheric pressure. The schematic depicted in Figure 2-7 shows the main parts of the CVD furnace used in this work:

- A 3" quartz tube,
- A quartz loader holding the samples,
- Heating elements, and
- A metallic shield.

The available input gases are: methane ( $\text{CH}_4$ ), ethylene ( $\text{C}_2\text{H}_4$ ) and hydrogen ( $\text{H}_2$ ), and two inert gases: nitrogen ( $\text{N}_2$ ) and argon ( $\text{Ar}$ ).

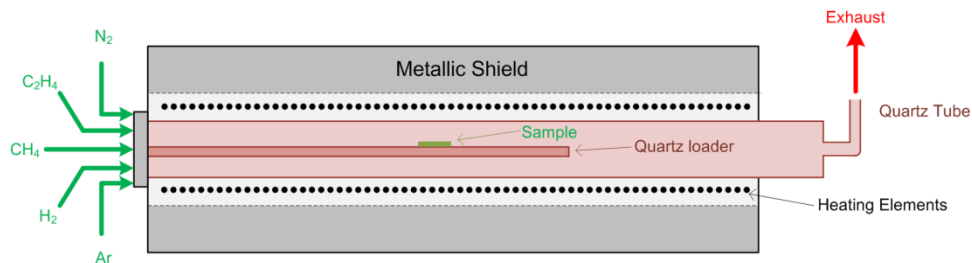


**Figure 2-7: Schematic of the chemical vapor deposition furnace used for carbon nanotube growth.**

Turning now to the growth parameters used for the hexagonal arrays of multilayer catalyst particles, the samples are loaded via the quartz loader into the 3” quartz furnace and the chamber is briefly purged with 10,000 sccm (standard cubic centimeters per minute) of Ar. It is followed by heating of the sample from room temperature to 900 °C under 500 sccm of H<sub>2</sub> which has an effect of reducing the catalyst as described in section 2.3. Finally, growth of SWCNTs is achieved using 1000 sccm of pure CH<sub>4</sub> feedstock (UHP grade) during 10 min, following by a cooling down under 1000 sccm of Ar [28, 29].

## **2.5 Experimental Results and Discussion**

Initially, Si substrates were used to evaporate the multilayer metal catalyst through a 450 nm diameter colloidal sphere mask. The evaporation was done at a low evaporation rate of  $\sim 0.2\text{-}0.5 \text{ \AA/s}$  under an operating pressure of  $\sim 1.8 \text{ \mu Torr}$ . Annealing of the polystyrene colloidal mask was omitted for this trial. A subsequent step of sphere removal was performed by sonication in either ethanol or dichloromethane, and then the samples were subjected to CVD. Results showed alignment of what appear to be SWCNTs along two perpendicular directions as seen in the SEM images of Figure 2-8.

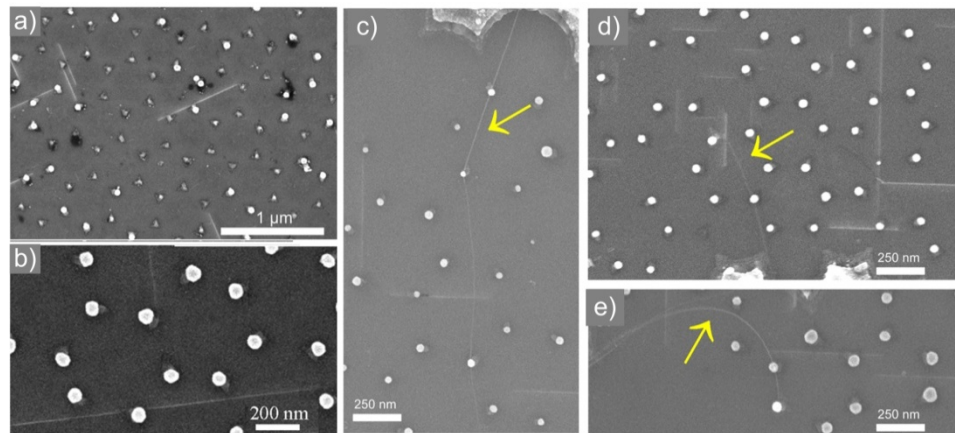


**Figure 2-8: Scanning electron microscopy of straight SWCNTs connecting catalyst islands grown on Si substrate from the multilayer metal catalysts evaporated at low rate. Mask removal is done using a)-b) ethanol and c-e) dichloromethane. Yellow arrows depict loss of alignment of the nanotubes at the edges of the hexagonal array of island catalysts.**

Based on these results, one can notice that the choice of solvent for mask removal does not affect the alignment of these nanostructures during growth. We found that most of the SWCNTs inside the hexagonal array are well-aligned along the two directions, while at the edges of the hexagonal pattern the tubes lose alignment as depicted in Figure 2-8c-e. A closer investigation revealed that these aligned SWCNTs are oriented along the  $\langle 110 \rangle$  family of the silicon substrate and one of these orientations coincides with the direction of the gas flow (see page 64). The samples were then subjected to height investigation via atomic force microscopy (AFM, Nanonics MV-1000) using Nanonics glass fiber probes in tapping mode. These glass probes are of  $\sim 10$  nm in tip diameter. Post CVD growth AFM results show heights between  $\sim 1$  and  $\sim 2$  nm, which is the typical diameter range for SWCNTs [5] (Figure 2-9).

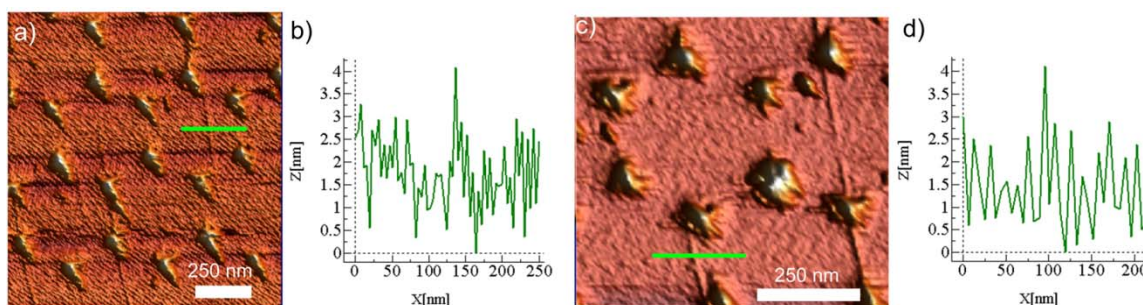


**Figure 2-9: Atomic force microscopy of straight SWCNTs on Si substrate connecting catalyst islands done at low evaporation rate. Height profiles b) and d) show typical SWCNT heights between  $\sim 1$  and  $\sim 2$  nm.**

Several height profile cross-sections on the post growth catalyst multilayer were also taken. Initially, the evaporated catalyst layer was  $\sim 66$  nm in height. This decreased to  $\sim 20$  nm after growth which is probably attributed to the spreading of the catalyst due to the relatively high growth temperature. Besides well-aligned SWCNTs inside the hexagonal array, T- and L-junctions are also sometimes seen in the SEM images of Figure 2-8, and other geometries have also been observed. AFM characterizations on these nanostructures revealed a typical height of 1-2 nm as shown in Figure 2-10.

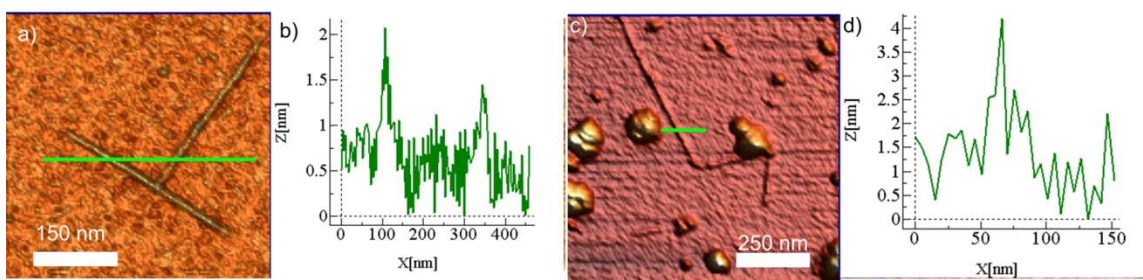


**Figure 2-10: Atomic force microscopy at the extremity of the hexagonal array showing a SWCNT a)-b) T-junction, and c)-d) L-junctions. Height profiles b) and d) show SWCNT heights of 1-2nm.**

Based only on AFM and SEM characterizations it was difficult to assess with certainty that these nanostructures are SWCNTs only, as Ci *et al.* [133] have reported

double-walled carbon nanotubes (DWCNTs) with less than 2 nm in diameters. Consequently, additional verifications are needed and for this purpose we performed Raman spectroscopy (632.8 nm HeNe laser excitation, custom Raman system) on our samples. The measured spectrum depicted in Figure 2-11a shows the presence of typical SWCNT bands that are a radial breathing mode (RBM), D-band and G-band (see section 1.4). In comparison with SWCNT spectrum, the RBM of DWCNTs is much richer and ranges from 100 to 400  $\text{cm}^{-1}$  [133-136] which is not the case in Figure 2-11a. As discussed in section 1.4, nanotube diameters can be found directly from the RBM band using eq. (1.14) and gives an average diameter of  $\sim 1.60 \pm 0.16$  nm, which agrees with the AFM measurements. A typical Raman spectrum of a metallic SWCNT showing the  $G^-$  and  $G^+$ -bands can be seen in Figure 2-11b. Using Figure 1-14c, the nanotube diameter is found to be  $\sim 1.85 \pm 0.10$  nm (see section 1.4 for details). Finally, it should be noted that the Raman of Figure 2-11a can either be a spectrum of an individual resonant SWCNT or bundles of SWCNTs.

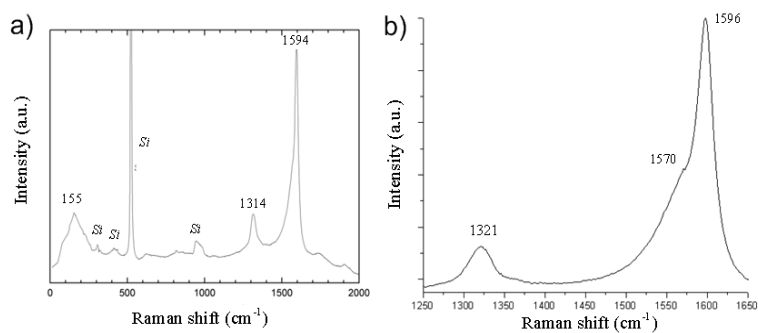


**Figure 2-11: Raman spectroscopy of samples done at low evaporation rate showing a) typical RBM, G- and D-bands, and b) a magnification of the  $G^-$  and  $G^+$  bands of a metallic SWCNT.**

Following the low evaporation rate sample, silicon substrates with multilayer catalyst done at higher evaporation rate were also subjected to CVD. The thin film catalyst was evaporated at a rate of  $\sim 2\text{-}2.5 \text{ \AA/s}$  under an operating pressure of  $\sim 1.8 \mu\text{Torr}$ . A subsequent step of sphere removal of the unannealed colloidal mask was performed by ultrasound sonication in either ethanol or dichloromethane, and then the samples were subjected to CVD. Post growth shows no preferential nanotube alignment on the silicon substrates (Figure 2-12a and b). Compared to the low evaporation rate samples, the higher evaporation rate results in higher SWCNT yield as seen in Figure 2-12a and b. For these samples, the catalyst island shapes (Figure 2-12c) are triangular due to a strong adhesion of the thin film on the silicon substrate and have  $\sim 40 \text{ nm}$  heights.

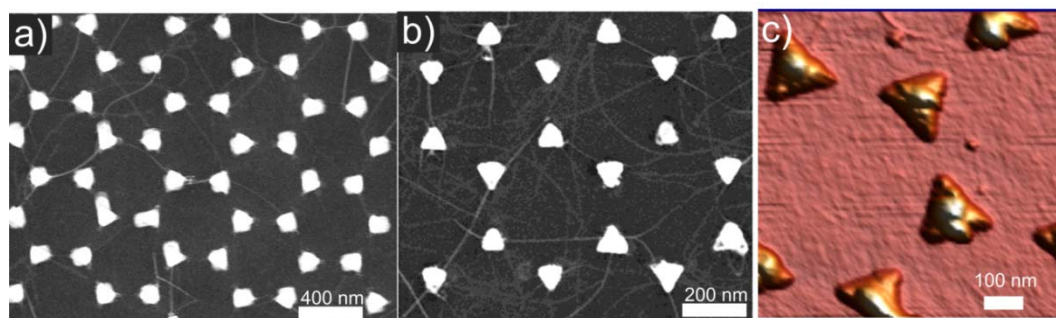


**Figure 2-12: a)-b) Scanning electron microscope characterizations of SWCNTs connecting catalyst islands grown on Si substrate from the multilayer metal catalysts evaporated at high rate, and c) atomic force microscopy of the post growth triangular catalyst islands.**

Turning now to Si/SiO<sub>2</sub> samples prepared at a low evaporation rate shown in Figure 2-13, no preferential alignment of SWCNTs within the hexagonal array of catalyst islands is evident. However, some SWCNTs connecting the catalyst islands are clearly seen in Figure 2-13a and b. From Figure 2-13 it seems that the island-island connections are dictated by whether the catalyst islands are “active” (bright islands) or “inactive”

(dark islands). One probable assumption is that the “active” state of some catalyst islands is caused by the nanotubes connecting them to the bulk catalyst pads and consequently they are at the same potential. However, based on Figure 2-13b-d, some islands appear “inactive” even if they are connected to nanotubes (red arrows), while on the other hand some islands are totally isolated from the bulk catalyst pads even though they are “active” (yellow arrows). Coupling between nearby structures can also dictate this behavior.

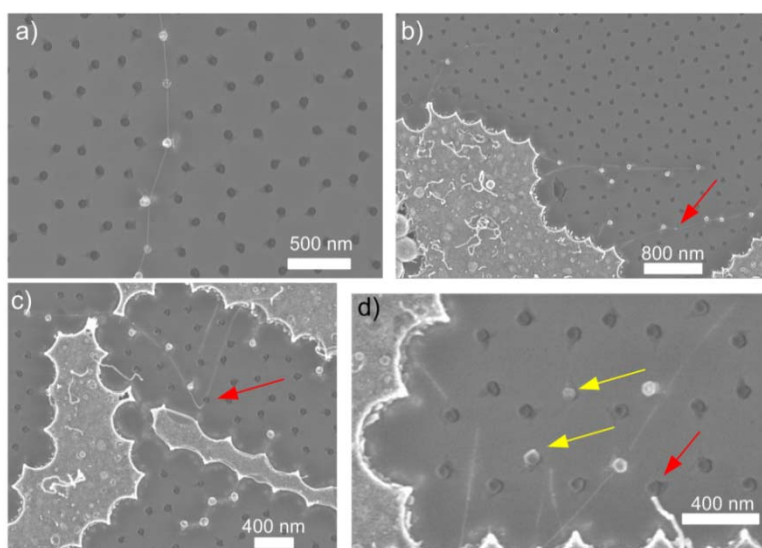


**Figure 2-13: Scanning electron microscope characterizations of SWCNTs connecting catalyst islands done at low evaporation rate on Si/SiO<sub>2</sub>. Yellow and red arrows denote respectively active and inactive catalyst island. No preferential alignment of SWCNTs within the hexagonal array of catalyst islands is reported and the bright background is due to the electron charging effect of the silicon oxide substrate [68].**

Based on these observations, it is possible that nanotube growth on SiO<sub>2</sub>/Si substrates is governed by electrostatic forces. In order to assess this hypothesis, we present a growth model based on the following experimental and theoretical facts:

- i. For multilayer metal catalyst carried out at low evaporation rates, the Al layer is readily oxidized to form dielectric  $\text{Al}_2\text{O}_3$  [137, 138] (Figure 2-14a) and it is well-known that this dielectric interface possesses uniform negative charge densities of  $\sim 1 \times 10^{12} - 6 \times 10^{12} \text{ e cm}^{-2}$  [139, 140].
- ii. Electric charges get transferred from the metal catalyst particles to the SWCNTs due to different work functions (SWCNT =  $\sim 4.8 - 5.4 \text{ eV}$  and cobalt =  $5 \text{ eV}$ ) [79]. This causes the catalyst particles to be positively charged while the SWCNTs negatively charged [79]. Due to the large dipole moment at high growth temperature of CNTs [90], the nanotube is assumed to be negatively charged nearby the catalysts while positively charged at the tip ends as depicted in Figure 2-14b.
- iii. During a base-growth mechanism the addition of a dimer ( $\text{C}_2$ ) into a SWCNT was estimated to an energy drop of  $\sim 10 \text{ eV/dimer}$  [54] at high temperature. This energy can also be used as the mechanical work required to extrude a SWCNT from the surface [54].
- iv. The van der Waals force that arises from nanotube-H-passivated Si surface interaction was estimated using numerical and experimental calculation to  $1 \text{ eV/nm}$  for a  $1 \text{ nm}$  in diameter SWCNT [141]. Although, this parameter is specific to the type of surface, and thus can be larger or smaller than  $1 \text{ eV/nm}$ , it gives a good approximation of the quantities involved [142].

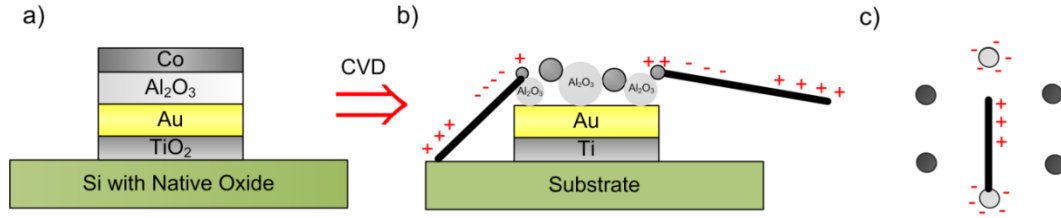


**Figure 2-14: Schematic of the multilayer catalyst islands a) as evaporated, b) during growth and c) electrostatic interaction between a SWCNT and active catalyst islands (grey color).**

From this information and assuming a base-growth mechanism, we can propose that initially during CVD growth, the nanotube is negatively charged, and consequently is pushed away from the initial catalyst by the extrusive force that arises from the addition of dimers and the repulsive force of the negatively charged catalyst island. Ultimately after a certain length a dipole moment is created along the nanotube which causes the tip to be positively charged and is then likely to be attracted by the nearest active catalyst (Figure 2-14c). Considering the experimental and theoretical facts described above, we can write an overall growth model equation as follows:

$$\begin{aligned}
 E(r) &= nE_{ext} \pm E_{elec} - E_{vdW} - E_{var} \\
 &= n \cdot \frac{10 \text{ eV}}{\text{dimer}} \pm \frac{Q}{4\pi\epsilon_0 r} eV - r_{cont} \cdot \frac{1 \text{ eV}}{nm} - E_{var}
 \end{aligned} \tag{2.1}$$

where  $n$ ,  $Q$ ,  $E_{ext}$ ,  $E_{elec}$ ,  $E_{vdW}$  and  $r_{cont}$  are respectively the number of dimers incorporated along the circumference of the tube, the electric charge due to the uniform negative charge densities ( $1 \times 10^{12} \text{ e cm}^{-2}$ ), the extrusive energy caused by dimer addition, the electrostatic attractive energy due to the initial (-) or adjacent (+) catalyst island, the restrictive van der Waals energy and the portion of the nanotube in contact with the substrate. Parameter  $E_{var}$  represents other phenomena that can randomize or change the orientation of SWCNTs during growth: viscous force of the hot carbon gas [54] or gas

flow direction [67, 70-73]. Gas flow direction has been proven to be a reliable way to orient SWCNT during growth [67, 70-73] and one can consider this one responsible for orienting CNTs along one direction but it fails to explain the mechanism of growth that governs nanotubes in other directions. As there is no actual experimental and/or theoretical data on the magnitude of the force/energy involved in the alignment of nanotube using gas flow, we choose to omit it and set  $E_{var} = 0$ . The extrusive energy ( $E_{ext}$ ) in eq. 2.1 indicates the maximal mechanical work that can be accomplished by the system [54], therefore assuming the catalyst particle stays active, the SWCNT will grow indefinitely. By adding the contribution of the latter forces, SWCNT growth will last as long as  $E(r) > 0$ , which indicates sufficient energy is available to “push” the nanotube out of the initial catalyst island (i.e. nucleation site).

To assess the growth model, we first need to find a starting value for the number of dimer added along the circumferential direction of the nanotube. Based on [23, 32], one can notice that tube indices ( $n.m$ ) are proportional to the nanotube diameter and hence to the number of dimers forming the circumferential direction. AFM height profiles show SWCNTs of 1-2 nm in diameter. Regardless of the nanotube type, the smallest extrusive energy occurs with a 1 nm diameter nanotube of indices (7,7). Therefore, seven dimers make up the circumference of the nanotube. Some one-dimensional numerical calculations were performed using  $n = 7$  and considering:

- i. The extrusive energy and the attraction of a positively charged nanotube tip by the negatively charged initial catalyst island (Figure 2-15a),

- ii. We then added the electrostatic attraction by the nearest active catalyst island located at 450 nm from the initial catalyst island (Figure 2-15b),
- iii. Finally, we considered the effect of nanotube-surface interaction (Figure 2-15c).

The result depicted in Figure 2-15a shows clearly that the electrostatic attraction created by the initial catalyst island where the nanotube nucleates is smaller than the mechanical work done by the system to promote SWCNT growth. Consequently, unrestricted and very long nanotubes are able to grow, which agrees with Ogrin *et al.* [59] observations (see Section 1.5.3.1). By adding the electrostatic attraction of the nearest active island (Figure 2-15b), an increase of the available energy near the active catalyst island for nanotube growth is observed. This indicates that the nanotubes are likely to be oriented toward the active catalyst island. On the other hand, if we consider the nanotube to be continuously in contact with the substrate, the restrictive van der Waals force (Figure 2-15c) stops the growth prematurely at  $\sim 58$  nm, which also agrees with Ogrin *et al.* [59] observations (see Section 1.5.3.1). Now, if we consider an electric field greater than  $0.1 \text{ V}/\mu\text{m}$  is needed to align the nanotubes [88], we found that the maximum distance at which the adjacent catalyst island should be located is  $\sim 480$  nm. Therefore, greater distances will weaken the electrostatic interaction between the catalyst islands and the nanotubes. Consequently SWCNT alignment between catalyst islands is unlikely to occur. Although the gas flow has not been included in the numerical simulations, it remains one of the major factors that can affect nanotube alignment and expand the limit at which the nearest adjacent catalyst islands should be located. Tube-

tube interaction is another restrictive factor that can influence nanotube alignment. Due to a strong van der Waals interaction between the nanotubes, these can either remain aligned if the surrounding CNTs are aligned within the hexagonal array or be attracted in random directions by individual and bundles of CNTs in the vicinity. Finally, the one-dimensional growth model presented here can be extended to a full two-dimensional model that considers multiple catalyst neighbors made of uniform and/or nonuniform catalyst composition.

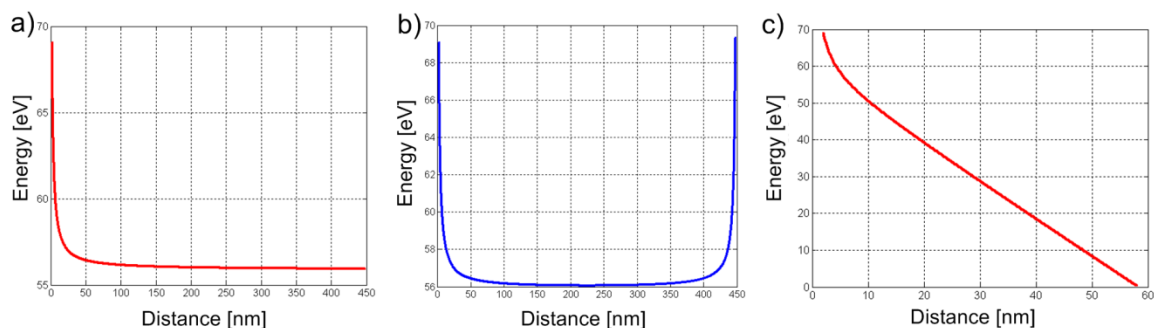


**Figure 2-15: Synthetic data using the a) extrusive energy and attractive force of the main island only (i.e. nucleation site), b) extrusive energy, attractive force of initial and adjacent island, and c) extrusive energy, van der Waals interaction and attractive force of initial and adjacent island.**

The growth mechanism responsible for the alignment of SWCNTs on silicon substrate is not well-understood yet but can possibly be due to the combination of the interactions discussed above and other phenomena such as nanotube-substrate interactions and silicide formation. Hydrogen passivation of silicon substrates is known to produce aligned semiconducting SWCNT as confirmed by TEM characterizations [78, 143-147]. However, in our case this is less likely to occur as it requires very low chamber pressures of 2  $\mu$ Torr. Another possible alignment mechanism is the coexistence of nanotube-silicide interaction during growth. Recently, works done by Tayebi *et al.* [148]

have reported that silicide align SWCNTs along the  $\langle 110 \rangle$  family of the silicon (100) substrates. In some AFM images of the samples done at low evaporation rates (Figure 2-16a-c), nanostructures with size that seems to agree with silicide nanowire sizes (i.e.  $\sim 2\text{-}5$  nm) were observed. This however cannot be verified at this point due to limited equipment resources as it requires advanced characterization tools (see chapter 5.1).

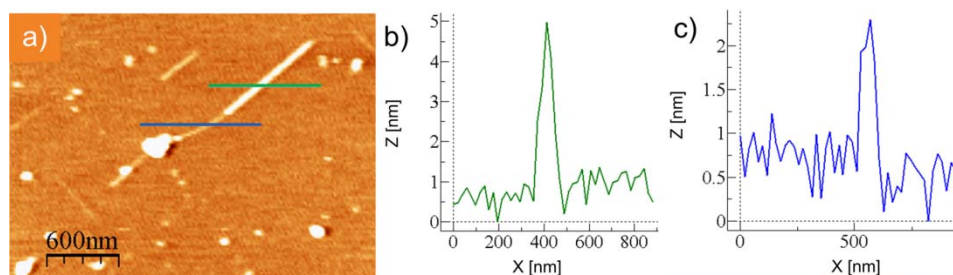


**Figure 2-16: a)-c) Atomic force microscopy of a possible silicide nanowire directly attached to an aligned SWCNTs on silicon substrate.**

For Si/SiO<sub>2</sub> substrates depicted in Figure 2-13, the 1  $\mu\text{m}$  thick oxide layer prevents silicide formation [63] and nanotube-surface interaction, and thus we can consider tube-catalysts islands electrostatic interaction, gas flow direction and van der Waals interaction as plausible alignment mechanisms. This explains the results of Figure 2-13 showing that aligned SWCNTs are connecting the catalyst islands. For the high yield samples depicted in Figure 2-12a-b, tube-tube interactions due to van der Waals force likely predominate and hinder electrostatic interactions between nanotube and substrate-catalyst islands. The yield difference between the two evaporation conditions is likely due to the composition of the adhesion layer. At low evaporation rate ( $< 1 \text{ \AA/s}$ ) and poor operation pressure ( $> 5 \text{ uTorr}$ ), Ti layers combine readily with O<sub>2</sub> and water in the evaporation chamber to form titanium oxide [138], whereas high evaporation rate prevents TiO<sub>2</sub> formation and consequently adhesion to the substrate is drastically

enhanced as shown in Figure 2-12c. This allows the formation of small catalyst particles [118] and it also prevents the subsequent metal layers from retracting and forming large catalyst clusters during the heating step.

## 2.6 Summary

In summary, colloidal lithography has been used to pattern SWCNT catalyst on Si and Si/SiO<sub>2</sub> substrates. Nanospheres have been used as a shadow mask during metal catalyst evaporation which resulted in large areas of periodic catalyst islands. CVD growth shows well-aligned SWCNTs on Si substrates within the hexagonal catalyst, while on Si/SiO<sub>2</sub>, SWCNTs connect the catalyst islands. Although the mechanism of such alignment is not fully understood, a numerical model of the growth mechanism has been presented and combination of electrostatic interaction, van der Waals interaction, tube-substrate interaction and gas flow direction are the most plausible candidates for such SWCNT alignment. AFM of the post-growth samples show SWCNTs of 1-2 nm in diameter. This agrees with the RBM spectrum. Based on the Raman spectroscopy, a mixture of individual and bundles of metallic and semiconducting nanotubes were observed. Due the advantages of colloidal lithography being an inexpensive and fast process that allows high control over the mask opening, it may be a reliable method of patterning periodic nanoscale catalyst islands for carbon nanotube growth that is suitable for large scale integration of CNTs in nanoelectronic systems.

### 3 Direct-Writing of Single-Walled Carbon Nanotube Catalysts

In this chapter, we present a novel AFM-based technique for patterning single-walled carbon nanotube catalyst in liquid form [108-110]. These types of catalyst are widely used to grow SWCNTs owing to their convenient and inexpensive processing. However, the amount of catalyst typically deposited from solution is large and difficult to control using conventional patterning approaches, and compatibility of the liquid solution with the patterning process need also to be considered [88]. Recently, nanowriting using nanopipettes [17-20] and dip-pens (DPNs) [21, 22] has been developed to deliver solution-based materials onto surfaces and/or modify substrates with nanoscale resolution.

#### 3.1 Background on Nanowriting

The versatility of DPN has also been demonstrated in making biological nanoarrays. More precisely, Lee *et al.* [149] used DPN to fabricate a template of arrays of mercaptohexadecanoic acid (MHA) for anti-p24 antibody immobilization. This array was then used to detect human immunodeficiency HIV-1 virus (HIV-1) p24 antigen. Applied to SWCNT growth, DPN has been used by Li *et al.* to generate cobalt patterns on SiO<sub>2</sub>/Si

substrates ranging from few micrometers down to 70 nm in size [150]. Their method consists of coating an AFM tip with cobalt nanoparticles by dipping it into an ink solution prior to the drawing process. Results show precise control over catalyst location and SWCNT growth was successfully achieved using carbon monoxide (CO) as carbon feedstock.

Contrary to DPN, nanopipettes can deliver solutions in a continuous way without refilling. This makes it a more convenient technique for large and long patterning processes. As an example, nanopipettes have been used by Sokuler *et al.* [151] to fabricate microlenses by delivering micro amount of a monomer mixture composed of 20  $\mu\text{L}$  of trimethylolpropane trimethacrylate (TRIM), 30  $\mu\text{L}$  of 2-methoxyethylether and 1 mg of 2,2-dimethoxy-2-phenylacetophenone (DPAP/DMPA) on glass substrates. Microlenses of 4-9  $\mu\text{m}$  in diameters were then obtained by polymerizing the monomer drops in argon atmosphere using a 6 W UV lamp of 254 nm. Other useful applications of nanopipettes have been demonstrated by Lewis *et al.* [152]. In their work, they used nanopipettes to chemically etch chrome using a solution of  $\text{K}_3\text{Fe}(\text{CN})_6 + \text{KOH}$  in a ratio of 3:2 saturated in water. Etched lines of approximately 1  $\mu\text{m}$  wide and  $\sim 16 \mu\text{m}$  in length were obtained. Furthermore, nanopipettes possessing two barrels with incorporated Ag/AgCl electrodes have also been used to pattern arbitrary shapes of DNA and protein [153]. Overall, nanowriting provides direct and precise control over surface patterning without requiring complex lithography processing. These advantages have not been exploited for CNT liquid catalyst patterning. In this section, we propose a new technique

based on direct nanowriting of SWCNT catalysts in liquid form via nanopipettes [108-110].

### 3.2 Apparatus and Materials

The nanowriting setup employed in the scope of this research consists of quartz and borosilicate glass nanopipettes with openings of 50 nm and 100 nm diameter (Nanonics Imaging Ltd) respectively mounted to an atomic force microscopy (AFM, Nanonics Imaging Ltd MV-1000) operating in contact mode. The liquid catalyst is introduced into the nanopipettes and it flows by capillary forces and accumulates near the pipette opening due to surface tension [17]. A schematic of the nanowriting process is shown in Figure 3-1.

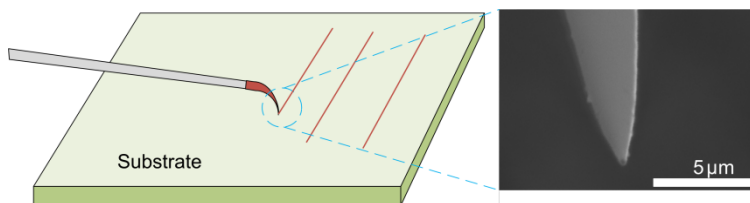


**Figure 3-1: Concept of direct nanowriting of liquid catalyst using nanopipettes. Inset shows a SEM characterization of a 100 nm opening borosilicate glass nanopipette.**

#### 3.2.1 Type of Catalysts Used

The type of liquid catalyst that will be used to fill the nanopipettes should be chosen carefully as the growth can be hindered. One of the widely used types of liquid catalysts is metal salts and they are divided into two distinct categories that is monometallic and bimetallic. In the first case, metal salt particles of Fe, Co or Ni as  $\text{Fe}(\text{NO}_3)_3 \cdot 9\text{H}_2\text{O}$ ,  $\text{Fe}(\text{SO}_4)_3 \cdot 9\text{H}_2\text{O}$ ,  $\text{Ni}(\text{NO}_3)_2 \cdot 6\text{H}_2\text{O}$  or  $\text{Co}(\text{NO}_3)_2 \cdot 6\text{H}_2$  are used as catalysts

for CNT growth [53]. On the other hand, bimetallic salts are a combination of the latter metals salts with either Mo or Ru which increase catalytic activity of the nanoparticles [53]. Under CVD, these metal salts undergo a change in their composition, as an example  $\text{Fe}(\text{NO}_3)_3$  that is transformed to iron oxide  $\text{Fe}_2\text{O}_3$  by the following relation  $(4\text{Fe}(\text{NO}_3)_3 \rightarrow 2\text{Fe}_2\text{O}_3 + 12\text{NO}_2 + 3\text{O}_2)$  [154]. It should be noted that a support material as  $\text{Al}_2\text{O}_3$ ,  $\text{SiO}_2$  or  $\text{Al}_2\text{O}_3\text{-SiO}_2$  is added to prevent catalyst coalescence during both catalyst preparation and CVD growth. In their work, Jodin *et al.* [155] reported Fe-Mo catalyst aggregations of several hundreds of nanometers in the absence of  $\text{Al}_2\text{O}_3$  support layer during catalyst preparation, while the catalyst morphology is unchanged with  $\text{Al}_2\text{O}_3$  support layer as depicted in Figure 3-2.

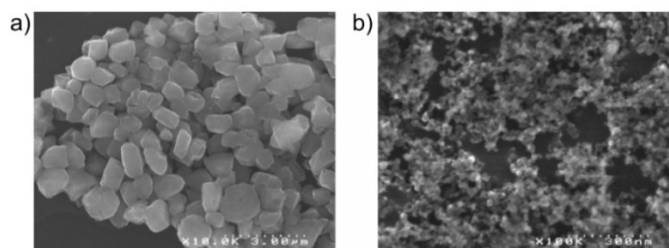


**Figure 3-2: Scanning electron microscope characterizations of Fe-Mo catalyst a) without fumed alumina and b) with 15 mg (0.5 g/L) of fumed alumina (adapted from [155]).**

For the most used metal salt (i.e.  $\text{Fe}(\text{SO}_4)_3 \cdot 9\text{H}_2\text{O}$ ), Cassell *et al.* [156] performed quantitative measurements of the weight gained by the sample after CVD and found that the addition of Mo increases the weight by 2.5 folds. Growth temperature of metal salts is another important parameter that needs to be carefully selected. Consequently, Klinker [154] used monometallic salts  $\text{Fe}(\text{NO}_3)_3 \cdot 9\text{H}_2\text{O}$ ,  $\text{Ni}(\text{NO}_3)_2 \cdot 6\text{H}_2\text{O}$  and  $\text{Co}(\text{NO}_3)_2 \cdot 6\text{H}_2\text{O}$  on  $\text{Si}/\text{SiO}_2$  substrates without support material to study the effect of growth temperature on the CNT yield. Results show metal catalyst coalescence and the hindering of carbon nanotube growth.

Discrete metal nanoparticles can also be obtained using proteins. Ferritin is commonly used for SWCNT growth and consists of an iron storage protein of  $\sim 12$  nm in size (Figure 3-3). More precisely, it contains up to 4500 iron ions ( $\text{Fe}^{+3}$ ) stored as ferrihydrite ( $5\text{Fe}_2\text{O}_3 \cdot 9\text{H}_2\text{O}$ ). This oxidized iron core of  $\sim 5$  nm depicted in Figure 3-3b has been shown to promote SWCNT with narrow diameter distribution during CVD growth [157]. The outer shell of ferritin is composed of twenty-four polypeptide subunits that will eventually be eliminated in a pre-CVD step of calcination. In the same manner as  $\text{Fe}(\text{NO}_3)_3$  get transformed into  $\text{Fe}_2\text{O}_3$  upon CVD, ( $5\text{Fe}_2\text{O}_3 \cdot 9\text{H}_2\text{O}$ ) will undergo the same process. The final product is thus dispersed nanoparticles of iron oxide.

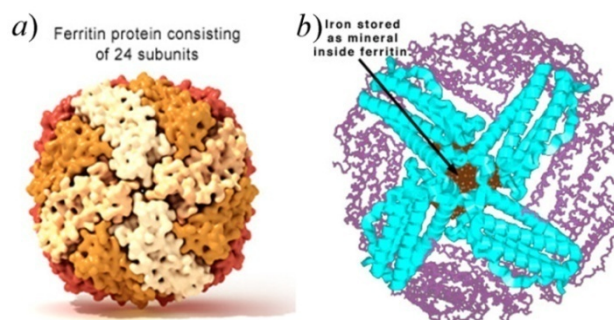


**Figure 3-3: Schematic of a ferritin protein showing a) the subunits, and b) the iron core (adapted from [158]).**

### 3.2.2 $\text{Al}_2\text{O}_3$ -FeMo Catalyst

One of the liquid catalysts used in the scope of this thesis is  $\text{Al}_2\text{O}_3$ -FeMo. The suspensions were formed by mixing respectively [13]:

- 40 mg of iron (III) nitrate nonohydrate ( $\text{Fe}(\text{NO}_3)_3 \cdot 9\text{H}_2\text{O}$ ),
- 3 mg bis(acetylacetonato)-dioxomolybdenum ( $[\text{CH}_3\text{COCH}=\text{C}(\text{O}^-)\text{CH}_3]_2\text{MoO}_2$ ),

- 30 mg of aluminum oxide C (fumed-alumina, 13 nm average primary particle size, Aerosil), and
- 30 ml of methanol.

Quantitative and qualitative characterization using TEM, SEM and weight gain calculations have shown that this type of catalyst gives high yield compared to other Fe catalyst salts [156]. This is due to the combination of catalytic enhancer, Mo, and support layer, Al. Furthermore,  $\text{Al}_2\text{O}_3\text{-FeMo}$  can be used directly on Si and Si/SiO<sub>2</sub> substrates without silicide formation and catalyst poisoning. It was also reported that the growth mechanism for this catalyst is predominately base-growth [156].

### **3.2.3 Cationized Ferritin Catalyst**

For the second liquid catalyst, we employed cationized ferritin [79, 82, 83, 159-162] solution (10 mg/ml in 0.15 M of NaCl, Sigma-Aldrich Co.) prepared by coupling horse spleen ferritin with *N,N*-dimethyl-1,3-propanediamine (DMPA). Ferritin catalyst was used as received and diluted 200, 50 and 20 times with deionized (DI) water [23]. Contrary to  $\text{Al}_2\text{O}_3\text{-FeMo}$ , Ferritin does not have a support layer and consequently only substrates with diffusion barriers such as Si/SiO<sub>2</sub> can be used.

## **3.3 Single-Walled Carbon Nanotube Growth**

SWCNT growth was carried out in a 3-inch quartz tube furnace operating near atmospheric pressure as described in Section 2.4.

### 3.3.1 Al<sub>2</sub>O<sub>3</sub>-FeMo Catalyst

For Al<sub>2</sub>O<sub>3</sub>-FeMo patterned samples, they were first heated under Ar at a flow rate of 1000 sccm from room temperature to 900 °C, followed by co-flowing 1080 sccm of CH<sub>4</sub> and 125 sccm of H<sub>2</sub> for 20 min. The samples were then cooled under Ar flowing at 1000 sccm.

### 3.3.2 Cationized Ferritin Catalyst

Growth of ferritin patterns began with a 10 min calcination step at 900 °C in air in order to remove the organic outer shell from the inorganic iron core (Fe<sub>2</sub>O<sub>3</sub>) of ferritin. Following calcination, the samples were either:

- i. reduced under 500 sccm of H<sub>2</sub> from room temperature to 900 °C and allowed to soak in 1000 sccm of H<sub>2</sub> for 1 min, followed by 1440 sccm of CH<sub>4</sub> and 75 sccm of H<sub>2</sub> for 10 min; or
- ii. reduced under 1000 sccm of H<sub>2</sub> from room temperature to 900 °C and allowed to soak in 1000 sccm of H<sub>2</sub> for 10 min, followed by 1440 sccm of CH<sub>4</sub> and 40 sccm of H<sub>2</sub> for 30 min.

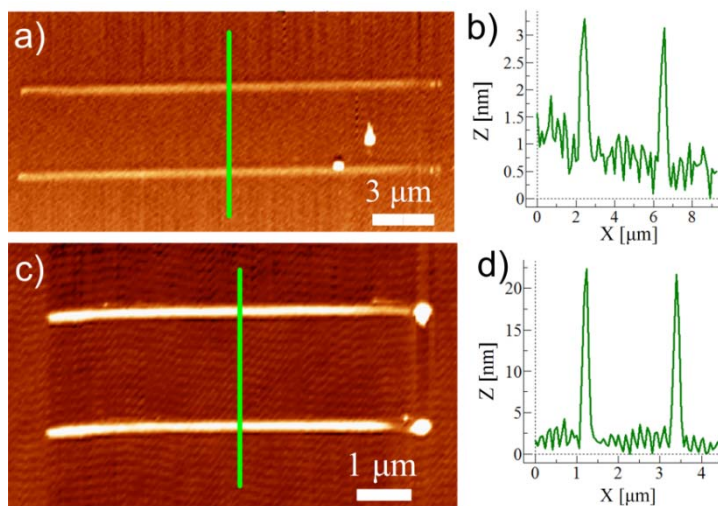
In both case, the samples were subsequently cooled under Ar flowing at 1000 sccm.

## 3.4 Experimental Results and Discussion

At first, simple parallel lines of each catalyst were drawn on Si and Si/SiO<sub>2</sub> substrates in order to assess the reliability of this method to deliver catalyst solutions in a controlled way. It should be noted that prior to nanowriting, the substrates were sonicated

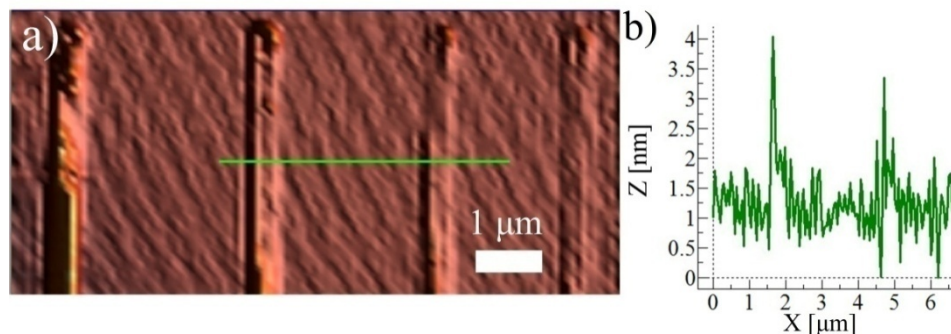
for 1 min in acetone followed by rinsing in isopropanol, DI water and drying in flowing  $N_2$  gas. Nanowriting was initiated by filling a borosilicate glass nanopipette of 100 nm opening with  $Al_2O_3$ -FeMo solution via a pipettor, and a quartz nanopipette of 50 nm opening with of 1:200 dilution of cationized ferritin solution using a syringe. Direct nanowriting of liquid catalyst was performed at a constant speed of  $10 \mu\text{m/s}$  on Si substrates for  $Al_2O_3$ -FeMo and Si/SiO<sub>2</sub> substrates for ferritin solution.

Figure 3-4a displays  $Al_2O_3$ -FeMo lines with good uniformity and the cross-section profile in Figure 3-4b indicates a height of approximately 3 nm and a width of 300 nm. Similar results were obtained using quartz nanopipettes filled with 1:200 dilution cationized ferritin solution as shown in Figure 3-4c. Based on the cross-section profile of Figure 3-4b, the lines in this case are approximately 100 nm wide and  $\sim 20$  nm in height, indicating a thickness of about 2 monolayers of ferritin.



**Figure 3-4: Atomic force microscopy of straight parallel lines of catalyst drawn at  $10 \mu\text{m/s}$  on a) Si substrate using borosilicate glass nanopipette filled with  $Al_2O_3$ -FeMo catalyst, and c) on a Si/SiO<sub>2</sub> substrate using quartz nanopipette filled with 1:200 dilution ferritin solution.**

In some instances, we noticed a nonuniformity during the nanowriting as displayed in Figure 3-5. This is probably due to a nonuniform catalyst solution and/or to a damaged nanopipette. The straight  $\text{Al}_2\text{O}_3$ -FeMo lines are however approximately 2.5 nm in height, which is consistent with the initial results.



**Figure 3-5: AFM image of  $\text{Al}_2\text{O}_3$ -FeMo lines on Si prior to growth (patterned with borosilicate nanopipette). b) Cross-section of  $\text{Al}_2\text{O}_3$ -FeMo lines  $\sim 2.5$  nm in height.**

Multiple parallel lines were drawn using  $\text{Al}_2\text{O}_3$ -FeMo catalyst on a Si substrate at the above writing parameters and then subjected to CVD growth. Post-CVD characterizations using SEM shows what seem to be SWCNTs connecting the catalyst lines as depicted in Figure 3-6a-c.

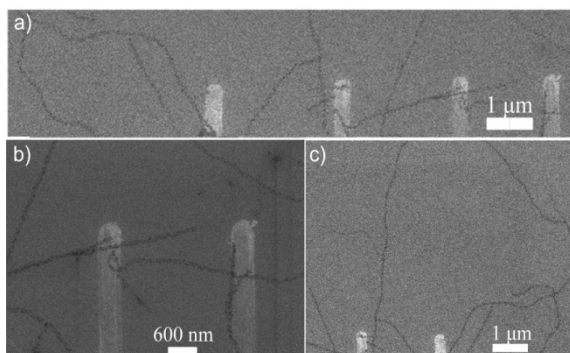


**Figure 3-6: Scanning electron microscopy of SWCNTs on a Si substrate grown from the  $\text{Al}_2\text{O}_3$ -FeMo catalyst lines.**

Upon closer inspection using AFM, we found that these nanostructures are of 2-4 nm in diameter as shown Figure 3-7, indicating that they are either bundles of SWCNTs or MWCNTs.

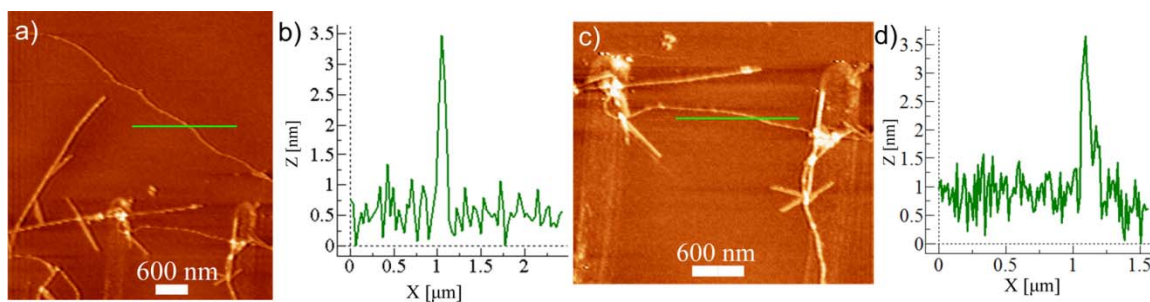


**Figure 3-7: Atomic force microscopy of SWCNTs grown from  $\text{Al}_2\text{O}_3$ -FeMo lines. Cross-section profiles b) and d) show a height of  $\sim 2.5$  nm.**

For additional verification of the structural composition of these nanostructures, we performed Raman spectroscopy (632.8 nm, Renishaw inVia Raman microscope) on the patterned regions. The spectrum in Figure 3-8 displays typical SWCNT bands that are a radial breathing mode at  $155.6 \text{ cm}^{-1}$  (Figure 3-8a), a D-band at  $\sim 1300 \text{ cm}^{-1}$  and a G-band at  $\sim 1590 \text{ cm}^{-1}$  (Figure 3-8b and c) arising from the graphitic C-C bonds of CNTs. Using eq. (1.14) and the RBM value, the average nanotube diameter is found to be  $\sim 1.59 \pm 0.16$  nm. Further information regarding the type of nanotube (semiconducting or metallic) and its diameter can be retrieved by a careful analysis of the G-band. Based on Figure 1-14c, the spectrum of Figure 3-8b is one of a metallic SWCNT due to its large G-band and its diameter is  $\sim 1.65 \pm 0.05$  nm, while in Figure 3-8c, the spectrum is one of a semiconducting nanotube with a diameter of  $\sim 1.55 \pm 0.20$  nm. This agrees with the diameter value found using the RBM band. Although, the spectra show either metallic or semiconducting nanotube type, the nanostructures exposed to the laser can be bundles of

tubes or a mixture of both nanotube types, and only some specific SWCNTs are in resonance with the incident laser energy (see section 1.4).

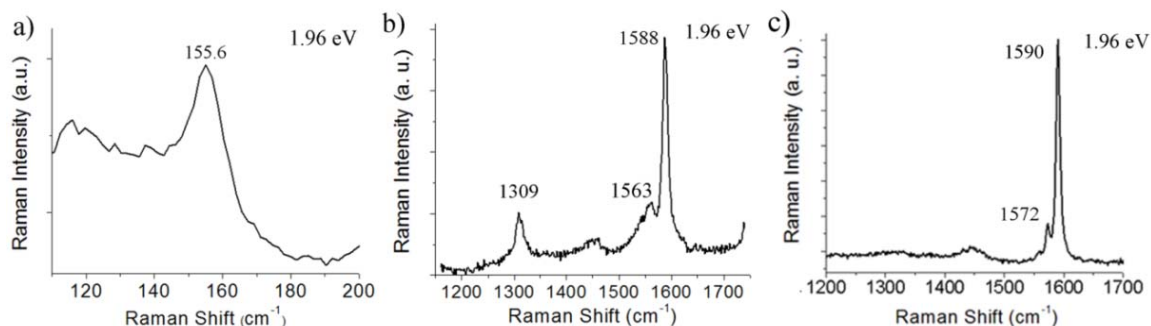


**Figure 3-8: Raman spectra of  $\text{Al}_2\text{O}_3\text{-FeMo}$  sample following CVD. a) RBM band of SWCNTs at  $\sim 155 \text{ cm}^{-1}$ , b) G-band at  $\sim 1588 \text{ cm}^{-1}$  and D-band at  $\sim 1309 \text{ cm}^{-1}$  of a metallic SWCNT, and c) G-band at  $\sim 1590 \text{ cm}^{-1}$  of a semiconducting SWCNT.**

Following the  $\text{Al}_2\text{O}_3\text{-FeMo}$  samples, Si/SiO<sub>2</sub> substrates were patterned with 1:50 diluted cationized ferritin solution and then subject to CVD growth under either condition (i) or (ii) described in section 3.3.2. Figure 3-9a depicts an individual SWCNT emanating from a catalyst line on a sample that was processed according to procedure (i). The cross-section profile in Figure 3-9b indicates the nanotube is approximately  $1.0 \pm 0.3 \text{ nm}$  in diameter. One can also notice that the height of the catalyst line decreases along most of its length from the initial value of approximately 20 nm to  $\sim 2 \text{ nm}$  after growth. Figure 3-9c shows another example of an individual SWCNT between the catalyst lines as well as a similar change in catalyst morphology.

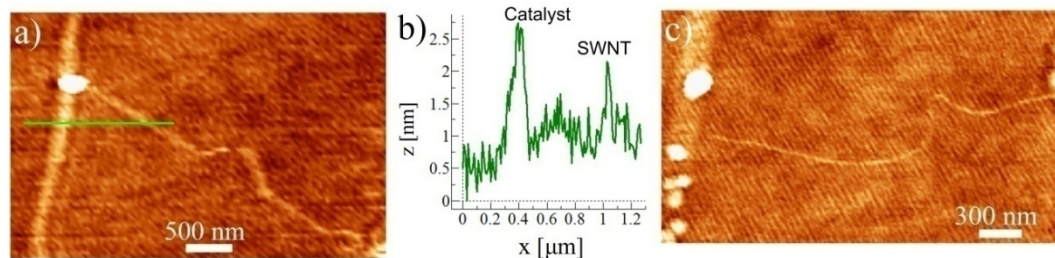


**Figure 3-9: Atomic force microscopy of ferritin catalyst (1:50 dilution) samples following CVD (patterned on silicon dioxide using quartz nanopipette). a) Individual SWNT on sample processed according to procedure (i) described in section 3.3.2. b) Cross-section showing a catalyst line of  $\sim 2$  nm in height and a SWNT of  $\sim 1$  nm in height. c) SWNT connecting two catalyst lines.**

Results obtained with samples processed using procedure (ii) are shown in Figure 3-10 and clearly show a SWCNT guided between the catalyst lines. In addition, large catalyst aggregations appear to have formed along the catalyst lines. Overall, we found significant changes in the ferritin catalyst distribution for both procedures and this will be addressed later in this section.

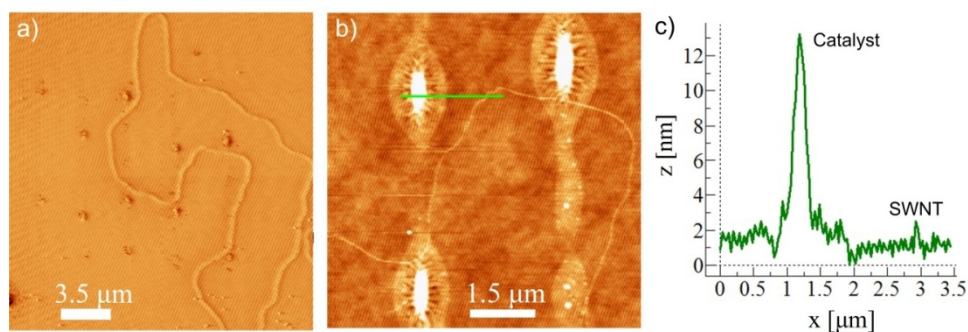


**Figure 3-10: Atomic force microscopy of ferritin catalyst (1:50 dilution) samples following CVD (patterned on silicon dioxide using quartz nanopipette) a) Phase image showing a SWCNT guided between catalyst lines on sample processed using procedure (ii). b) Close-up image of the SWCNTs and catalyst lines. c) Cross-section of a catalyst line of  $\sim 10$  nm in height and a SWCNT of  $\sim 1$  nm in height.**

Additional verifications were performed on the patterned regions of the post-growth ferritin sample using Raman spectroscopy (632.8 nm, Renishaw inVia Raman

microscope). The spectra depicted in Figure 3-11 show typical CNT bands that are a G-band at  $1590\text{ cm}^{-1}$  and a D-band at  $1300\text{ cm}^{-1}$ .

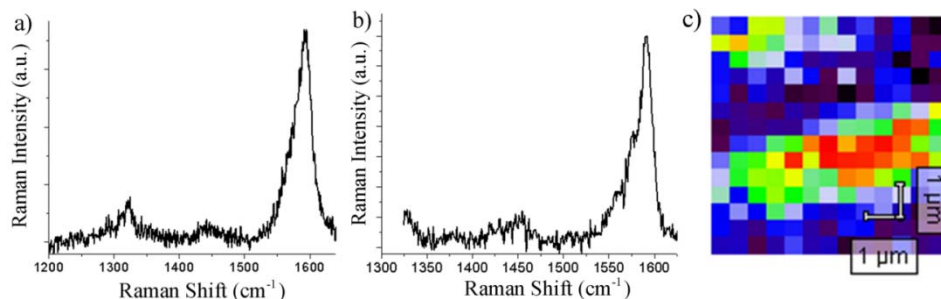


**Figure 3-11: Raman spectroscopy of post-growth ferritin samples showing a)-b) D- and G-bands respectively at  $\sim 1300\text{ cm}^{-1}$  and  $\sim 1590\text{ cm}^{-1}$ , and c) intensity map the G-band (intensity increases from blue to red with red at  $\sim 1590\text{ cm}^{-1}$ ).**

We found that in general the  $\text{Al}_2\text{O}_3\text{-FeMo}$  lines drawn with nanopipettes were wider than ferritin lines drawn under similar conditions. We attribute this behavior to the relatively large contact angle of the aqueous ferritin solution with silicon dioxide, which reduces that amount of liquid spreading on the surface and contributes to the narrower lines observed. Other drawing parameters that directly affect nanowriting resolution and the amount of catalyst deposited include tip velocity and contact time. Consequently, we investigated the effect of the tip velocity on catalyst morphology by drawing lines at  $50\text{ }\mu\text{m/s}$ ,  $10\text{ }\mu\text{m/s}$ ,  $5\text{ }\mu\text{m/s}$  using both types of catalyst. Figure 3-12 shows an AFM scan of parallel lines on Si substrates drawn using a borosilicate nanopipette with  $\text{Al}_2\text{O}_3\text{-FeMo}$  catalyst. It is clear from this image that the amount of catalyst deposited increases as the tip velocity decreases. The cross-section AFM line scans in Figure 3-12b and c indicate that catalyst height increases from  $1.5\text{ nm}$  to  $3.5\text{ nm}$  by changing nanopipette velocity from  $50\text{ }\mu\text{m/s}$  to  $5\text{ }\mu\text{m/s}$ .

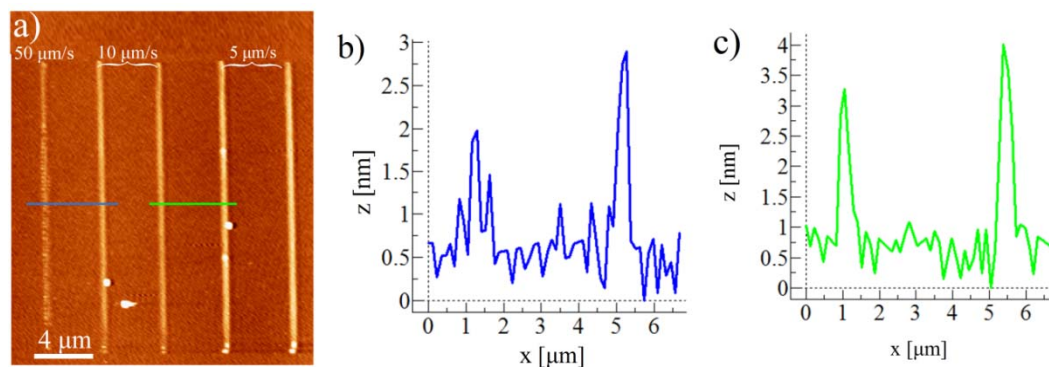


**Figure 3-12: Atomic force microscopy of a) parallel lines drawn using borosilicate nanopipette with  $\text{Al}_2\text{O}_3\text{-FeMo}$  at velocities indicated, b) cross-section of  $50\ \mu\text{m/s}$  and  $10\ \mu\text{m/s}$  drawn lines displaying heights of 1.5 nm and 2.5 nm, respectively, and c) cross-section of  $10\ \mu\text{m/s}$  and  $5\ \mu\text{m/s}$  lines displaying heights of 2.5 nm and 3.5 nm, respectively.**

Similar results were obtained for ferritin lines (Figure 3-13) in which catalyst height increased from 9 nm ( $\sim$  monolayer) to 20 nm when tip velocity was changed from  $50\ \mu\text{m/s}$  to  $5\ \mu\text{m/s}$ .

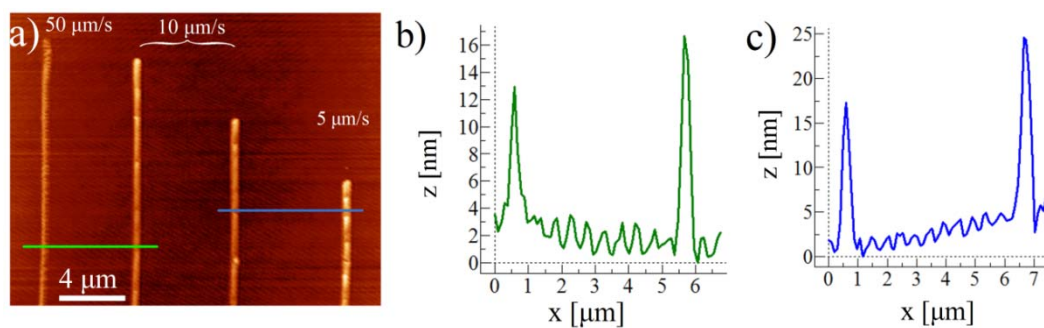


**Figure 3-13: Atomic force microscopy of a) parallel lines drawn using quartz nanopipette with 1:50 dilution ferritin solution at velocities indicated, b) cross-section of  $50\ \mu\text{m/s}$  and  $10\ \mu\text{m/s}$  drawn lines displaying heights of 9 nm and 15 nm respectively, and c) cross-section of  $50\ \mu\text{m/s}$  and  $10\ \mu\text{m/s}$  drawn lines displaying heights of 14 nm and 20 nm respectively.**

Based on data from several sets of nanowriting experiments, the arithmetic mean of catalyst height at each tip velocity for  $\text{Al}_2\text{O}_3\text{-FeMo}$  and 1:50 diluted ferritin solution is

reported in Table 3-1. It should be noted that the uncertainty was calculated using the largest variation compared to the arithmetic mean.

**Table 3-1: Catalyst height as a function of tip velocity**

	Tip velocity		
	50 $\mu\text{m/s}$	10 $\mu\text{m/s}$	5 $\mu\text{m/s}$
$\text{Al}_2\text{O}_3\text{-FeMo}$	$1.3 \pm 0.5 \text{ nm}$	$2.4 \pm 0.4 \text{ nm}$	$3.5 \pm 0.6 \text{ nm}$
<b>1:50 Ferritin</b>	$11.0 \pm 1.8 \text{ nm}$	$15.0 \pm 2.2 \text{ nm}$	$21.0 \pm 3.7 \text{ nm}$

These results show the correlation between tip velocity and catalyst height, and highlight nanowriting as an effective technique for depositing precise amounts of CNT catalyst. We also examined the effect nanopipette contact time had on the nanowriting process. For example, ferritin dots drawn with different contact times were patterned into arrays as depicted in Figure 3-14a.

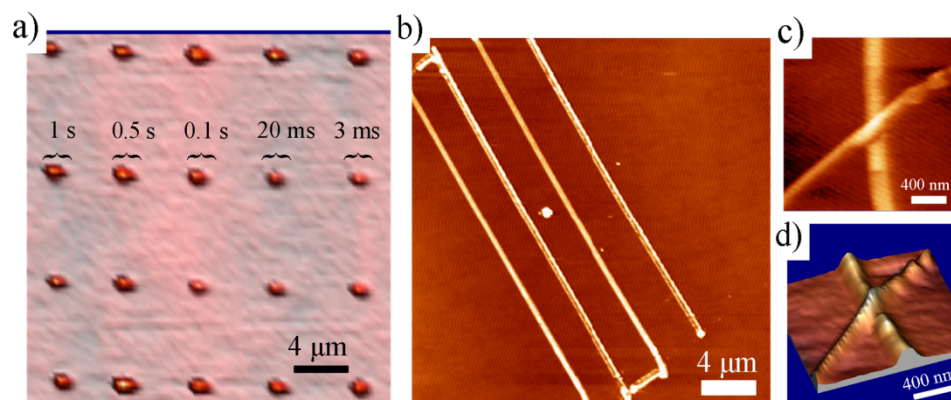


**Figure 3-14: Atomic force microscopy of a) a 4 x 5 dot array drawn using quartz nanopipette filled with ferritin solution (1:200 dilution) for different contact times, b) a zig-zag of  $\text{Al}_2\text{O}_3\text{-FeMo}$ , and c-d) overlapping ferritin lines and its 3D projection showing one catalyst line on top of the other (right).**

As expected, there is an overall trend indicating that more catalyst is deposited for longer contact time, however the rapid release of liquid surface tension at the initial point of contact with the substrate makes control more difficult in this case compared to

adjusting the drawing speed. While retracting the nanopipette, the surface tension causes the solution to be continuously delivered to the surface until a critical distance is reached at which the liquid breaks apart from the tip (Figure 3-15). As a consequence, the actual contact time during the retraction of the tip is greater than expected and therefore an additional amount of solution to the surface is delivered. This behavior can be seen at the end of the parallel catalyst lines of Figure 3-4 and Figure 3-12.

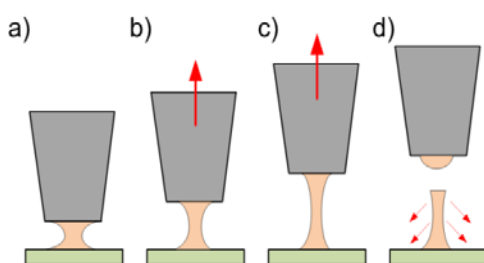


**Figure 3-15: Schematic of the tip-liquid interaction while the nanopipette is retracted. a) The catalyst solution is delivered to the surface for an amount of time  $t$ , b)-c) while retracting the nanopipette the liquid is still delivered to the surface, and d) critical distance at which the meniscus breaks apart from the nanopipette tip.**

To achieve a better control over the amount of delivered catalyst a pressure regulator may be attached to the nanopipette [17]. From analysis of the experiments we found that ferritin catalyst dot widths are directly correlated to the contact times. Table 3-2 shows experimental data obtained from Figure 3-14a.

**Table 3-2: Ferritin catalyst widths as a function of contact time**

	Contact Time				
	3 ms	20 ms	0.1 s	0.5 s	1 s
<b>Experimental data [nm]</b>	505 ± 38	512 ± 45	564 ± 40	605 ± 33	643 ± 35

To show the versatility of the nanowriting approach for creating catalyst distributions, more complex geometries were also patterned. Figure 3-14b-d show various

patterns done with ferritin (1:200 dilution) and  $\text{Al}_2\text{O}_3\text{-FeMo}$  solution. These patterns demonstrate the control afforded by the nanowriting approach for creating custom catalyst patterns for nanotube growth with minimal preparation time, suitable for device prototypes.

An examination of nanotube yield from the nanowritten catalyst patterns provided insight into both the nanopipette catalyst writing process and CNT growth from the catalyst patterns. In particular, we found that dot array patterns did not yield any nanotubes, regardless of the catalyst type or CVD process used. Generally, a reduced yield would be expected for the dot patterns since less catalyst is being deposited relative to the extended line distributions. However, this does not explain the complete absence of CNTs on the dot arrays across several process trials.

The size of the catalytic  $\text{Al}_2\text{O}_3\text{-FeMo}$  clusters in liquid suspension may contribute to the lower yield observed. If the clusters are comparable in size to the opening of the nanopipette this would reduce the probability that active catalyst particles are deposited on the substrate, thereby lowering overall yield. Future studies using larger diameter nanopipettes should be able to address this issue. In the case of ferritin, we observed that the catalyst patterns displayed changes in height and aggregation into larger clusters as shown in Figure 3-10. On the one hand, the change in height can be attributed to the calcination step, which removes the organic shell of the ferritin molecule. However, movement and aggregation of the remaining inorganic iron oxide clusters can also occur during the subsequent high temperature reduction and CVD steps, which would lower SWCNT yield.

In order to better understand the surface behavior of ferritin catalyst and its affect on nanotube yield, we performed AFM on samples after the calcination step. Figure 3-16 shows a ferritin line patterns before and after calcination. Initially the ferritin is uniformly distributed along the line (Figure 3-16a) with an average height of  $\sim 25$  nm, as shown in the cross-section profile of Figure 3-16b.

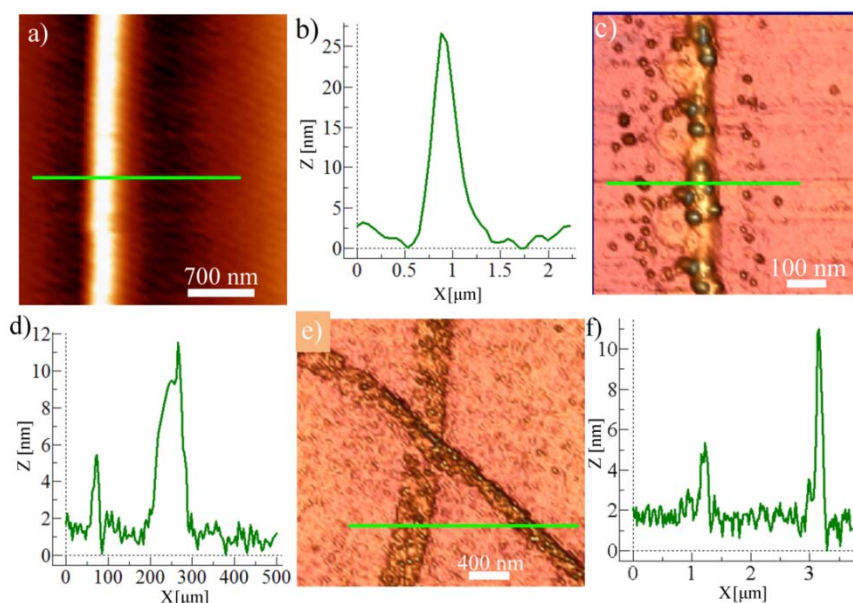


**Figure 3-16: Atomic force microscopy of a) initial ferritin line drawn on Si/SiO<sub>2</sub> using a quartz nanopipette, b) cross-section of ferritin line of  $\sim 25$  nm in height, c) ferritin line after calcination step displaying catalyst clustering, d) cross-section of ferritin line after calcination, and e) ferritin line depicted in Figure 3-14c) after calcination and f) its cross-section.**

After calcination however, catalyst particles from a few nanometer to  $\sim 12$  nm in height are visible, with some particles diffused away from the edges. This is likely the result of Fe<sub>2</sub>O<sub>3</sub> particles movement after the removal of their outer organic shell, with some particles clustering together while others diffuse away from the original catalyst pattern. Although the ferritin catalyst pattern definitely changes during calcination, the

AFM images depicted in Figure 3-10 indicate that additional changes likely occur during the reduction and/or CVD steps.

Finally, nanotube alignment during CVD growth on the patterned regions (Figure 3-6 and Figure 3-10) can be influenced by a number of factors. Electrostatic interaction with the catalyst patterns in vicinity is unlikely to be the main driving force for nanotube alignment because: i) the patterned lines are separated by larger distances and ii) the composition of ferritin catalyst does not include  $\text{Al}_2\text{O}_3$ . This may explain why the SWCNTs observed in the AFM images are not as straight as in chapter 2 images. Other possible factors include the gas flow direction (see section 1.6) and inter-tube interaction.

### **3.5 Direct-Patterning of Nanostructures Using Nanopipettes**

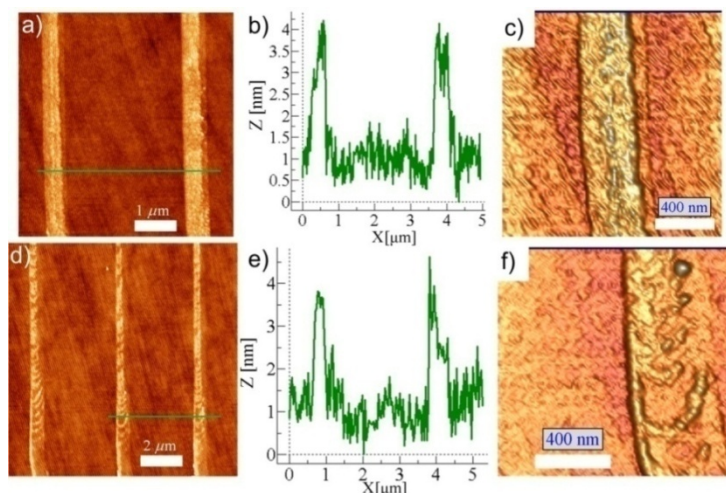
Besides patterning SWCNT catalysts in liquid form, nanowriting can be employed to directly deliver carbon based materials as CNTs or buckyballs ( $\text{C}_{60}$ ) on different substrates. Direct-writing of CNTs using DPN and nano/micro fountains has received little attention from the scientific world. It is only in 2008 that Baba *et al.* [163] and Schwamb *et al.* [164] demonstrated the first concept of nanowriting involving patterning CNTs using respectively microchannels and DPNs, and borosilicate micropipettes of 1, 10 and 100  $\mu\text{m}$  in diameter. Only sporadic agglomerations of CNTs were demonstrated.

The nanowriting setup consists of borosilicate nanopipettes of 100 and 250 nm in diameters (Nanonics Imaging Ltd). The CNT solutions were made by sonication of

SWCNTs purchased from SouthWest NanoTechnologies (SWeNT CG 100,  $0.87 \pm 0.3$  nm in diameter) in either methanol or chloroform as follows:

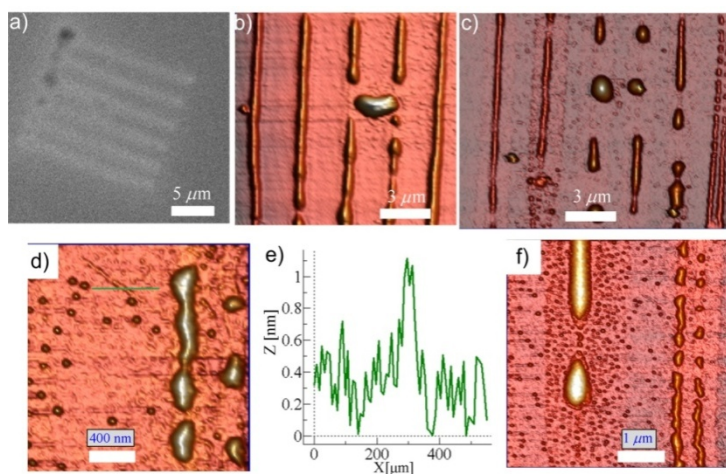
- SWCNTs/methanol solution:
  - 1 mg of SWeNT was mixed with 2.5 ml of methanol in a borosilicate glass vials, sonicated for 30 min and then allowed to settle for 10 min before use.
- SWCNTs/chloroform solution:
  - 1.6 mg of SWeNT was mixed with 80 ml of chloroform in a Pyrex flask with a glass stopper, sonicated for 30 min and then allowed to settle for 5 min before use.

Afterwards, the supernatant from each solution was used to fill the nanopipettes. A logical choice of solvent would have been to use 1,2-dichlorobenzene (oBCB) because of its high SWCNT solubility [165]. However, during sonication, this solvent is well-known to form polymer (a.k.a. sonopolymer) [166, 167]. Chemical compatibility of the solvent with the nanowriting setup materials needs also to be considered. We found methanol and chloroform appropriate for the direct-writing of SWCNTs. At first, a borosilicate nanopipette of 100 nm in diameter filled with SWCNT/methanol was used to pattern simple straight lines on Si/SiO<sub>2</sub> substrates at 10  $\mu\text{m/s}$ . Results in Figure 3-17 show long and uniform lines of  $\sim 3$  nm in heights.



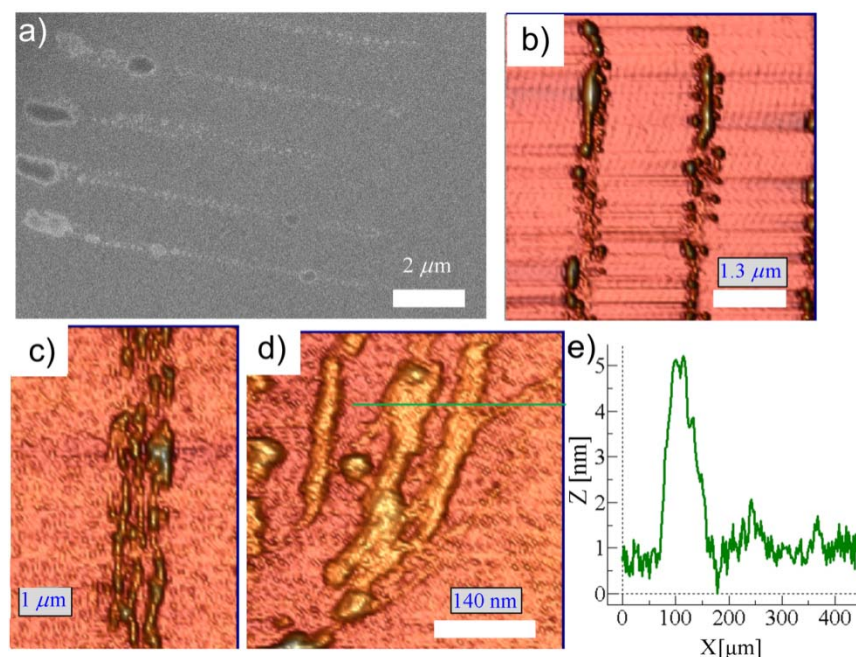
**Figure 3-17:** a)-f) Atomic force microscopy of lines drawn using SWCNT in methanol solution on Si/SiO<sub>2</sub> substrates and a borosilicate nanopipette of 100 nm in diameter.

Closer AFM investigations of the lines revealed what look like bundles of SWCNTs as depicted in Figure 3-17f. As we did not perform any centrifugation or filtration of the CNT solution, we expect the patterned lines to contain some aggregations of metal catalyst and carbon residue. Similar results were obtained on Si and Si/SiO<sub>2</sub> substrates using borosilicate nanopipettes of 250 nm opening (Figure 3-18).



**Figure 3-18:** Patterns drawn using a borosilicate nanopipette of 250 nm in diameter and SWCNT/methanol solution at 10 μm/s. a) Scanning electron microscopy of SWCNT lines on Si substrate. Atomic force microscopy of SWCNT lines on b) Si, c) Si/SiO<sub>2</sub>, d)-e) close-up of a SWCNT emanating from a bundle on Si, and f) close up of a bundle on Si/SiO<sub>2</sub>.

An examination of the patterns using SEM provided no information regarding the composition of the lines (Figure 3-18a). Further characterization using AFM (Figure 3-18b and c) revealed discontinued lines on Si and Si/SiO<sub>2</sub> substrate, and catalyst particles are also clearly visible in Figure 3-18d and f. We also observed what is likely to be an individual SWCNT emanating from one of the patterned lines as seen in Figure 3-18d. Thereafter, a borosilicate nanopipette of 100 nm in diameter filled with SWCNT/chloroform was used to pattern simple straight lines on Si substrates at 10  $\mu\text{m/s}$ . Here too, SEM (Figure 3-19a and b) did not provide detailed information about the patterned lines and AFM characterizations were required.



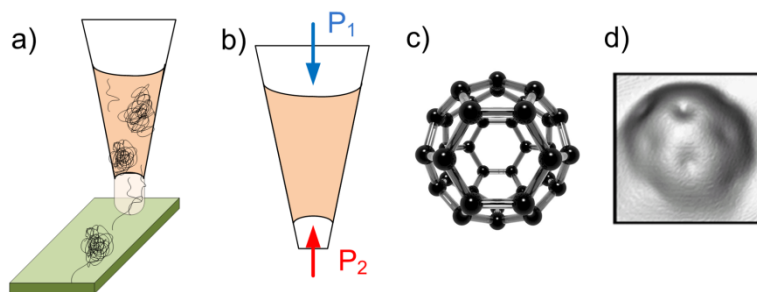
**Figure 3-19: Patterns drawn on Si substrates using borosilicate nanopipette of 100 nm in diameter and SWCNT/chloroform solution at 10  $\mu\text{m/s}$ . a)-b) Scanning electron microscopy of straight lines. Atomic force microscopy of c) straight lines, d)-e) close-up showing bundles of SWCNTs and f) their profile height.**

Figure 3-19c shows discontinued lines and upon close inspections we found that the lines are composed of what appear to be individual and bundles of SWCNTs (Figure 3-19d-f) of respectively  $\sim 4$  nm and  $\sim 1$  nm in height. Nanowriting of SWCNT/chloroform lines on Si/SiO<sub>2</sub> was also performed but no patterned lines were observed.

These inconsistencies in the uniformity of the CNT lines are due likely to several factors. Firstly, with both solutions, we have experienced a systematic clogging of the nanopipettes after several uses. This behavior was also sometimes observed after drawing just a couple of lines. We have attempted many cleaning steps consisting of filling the nanopipette with either methanol or chloroform and drawing straight lines, but without clear success. From these observations, we concluded that the nanotubes are getting tangled within the nanopipettes due to their long length. For large nanopipette openings, sporadic amounts of tangled CNTs are able to reach the surface (Figure 3-20a) resulting in nonuniform lines in Figure 3-18. On the other hand, small nanopipette openings act as filters, preventing tangled CNTs to reach the surface and thus the uniform patterned lines seen in Figure 3-17.

Now comparing both solvents at the same drawing conditions (Figure 3-17 vs Figure 3-19), chloroform lines yield better SWCNT dispersion on the substrate with however less uniformity and very small amounts. As different solvent type are involved, different vapor pressure are in play due to different evaporation rate (evaporation rate of chloroform is twice higher than methanol). In fact, for some liquid solutions, the vapor pressure at the small nanopipette end ( $P_2$  in Figure 3-20b) is larger than the vapor

pressure at the large nanopipette end ( $P_1$  in Figure 3-20b). This creates a negative pressure on the liquid that pushes it away from the opening. This vapor pressure issue was observed during the nanowriting process with chloroform. Patterning trials involving chloroform yield no patterns on Si substrate. Covering the large nanopipette end with Teflon tape to create a positive pressure on the liquid from the large end appeared to solve this problem.



**Figure 3-20: Schematic of direct-nanowriting of SWCNT solutions showing a) aggregation of SWCNTs within the nanopipette and b) vapor pressure at each extremity. c) Schematic of a fullerene  $C_{60}$  molecule made entirely of carbon atoms and d) STM of  $C_{60}$  [168].**

Further demonstrations of the nanowriting capabilities were done using  $C_{60}$  molecules [169]. To our knowledge, direct-writing of  $C_{60}$  molecules via DPN or nanopipette has not been achieved thus far.  $C_{60}$  is a  $\sim 1$  nm diameter soccer ball shaped molecule made entirely of carbon atoms [169, 170] (Figure 3-20c and d). For nanowriting, borosilicate nanopipettes of 100 nm in diameter filled with  $C_{60}$  diluted in toluene were used to pattern straight lines on Si and Si/SiO<sub>2</sub> substrates at a constant tip velocity of 10  $\mu\text{m/s}$ . Figure 3-21 shows nonuniform  $C_{60}$  lines caused by aggregation of fullerene molecules upon drying on the surface. Height profiles depicted in Figure 3-21c and f display heights of  $\sim 1.5$ - $2.5$  nm, which corresponds respectively to a monolayer and

bilayer of  $C_{60}$ . Larger aggregations of  $\sim 20$  nm in heights are also clearly visible in the AFM images.

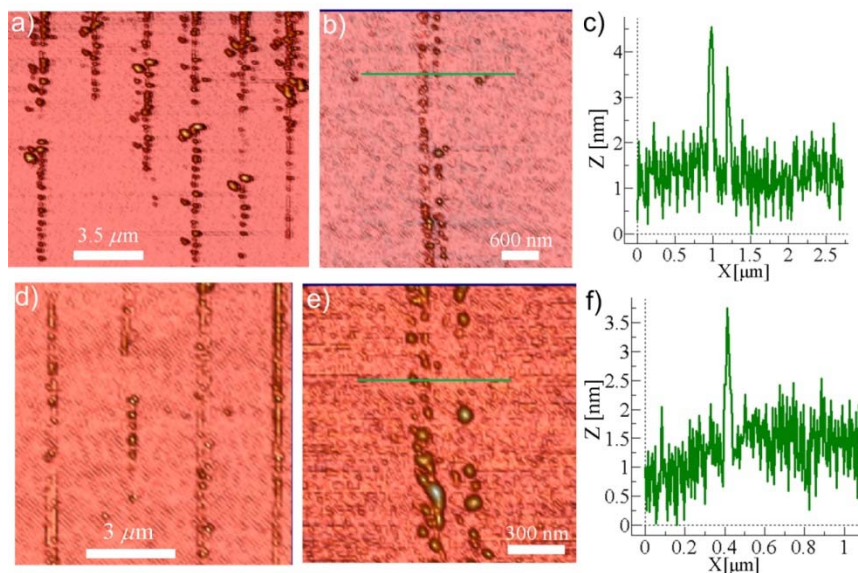


**Figure 3-21: Atomic force microscopy of lines drawn using  $C_{60}$ /toluene and borosilicate nanopipette of 100 nm in diameter on a) Si, b)-f) Si/SiO<sub>2</sub>. Profile heights c) and f) display a height of  $\sim 2.5$  nm,  $\sim 1.5$  nm and  $\sim 2$  nm, respectively.**

### 3.6 Summary

The abilities of direct nanowriting of liquid catalyst have been demonstrated as a reliable technique to produce nanoscale catalyst geometries as required for CNT growth and applications. CVD growth of the patterned regions resulted in individual and bundles of SWCNTs which was later been confirmed by Raman spectroscopy of the samples, giving metallic and semiconducting SWCNTs of  $\sim 1$ - $2$  nm in diameter. Our results highlight nanowriting as an effective method to directly write precise catalyst shapes for nanotube growth, in a convenient manner that is not specific to a particular type of catalyst. Furthermore, nanowriting was also used to pattern carbon based materials such

as SWCNTs and  $C_{60}$  molecules on Si and Si/SiO<sub>2</sub>. Nanowriting allows the controlled nanoscale deposition of catalyst into predefined patterns for the creation of functional CNT architectures and their integration into nanoelectronic devices.

## **4 Electronic Properties and Applications of Produced Single-Walled Carbon Nanotube Structures**

In this chapter, electronic characterizations of the colloidal lithography and nanowriting samples are presented. First, a brief survey on CNTFET models is introduced which subsequently allow us to better understand the electronic transport in the nanotube samples and help predict the effects of various parameters such as contact resistance, elastic and inelastic scatterings on device performance.

### **4.1 Survey of Carbon Nanotube Field-Effect Transistor Modeling Tools**

A far as carbon nanotube field-effect transistors are concerned, most of the research in this field has been aimed toward device fabrication and demonstrating the merits of CNTs in future electronics. Few design tools have been proposed to predict CNT device performances and to explore practical devices with a high level of complexity. In order to be minimally accurate and realistic, the CNTFET model must contain some essential device physics:

1. Backscattering due to Schottky barrier, and scattering from optical and acoustic phonons, and
2. Charge screening between CNTs for bundles or parallel CNT arrays.

One of the most widely used techniques for CNTFET modeling is the non-equilibrium Green's formalism (NEGF). This powerful approach has been employed to simulate a wide variety of electronic devices from conventional Si MOSFETs, CNTFETs and molecular transistors [171]. Applied to CNTFETs, the approach is to solve the following Green's function under perturbation from the drain, source and gate [171]:

$$G(E) = [EI - H - \Sigma_1 - \Sigma_2 - \Sigma_S]^{-1} \quad (4.1)$$

where  $I$  and  $H$  are respectively the identity matrix and the Hamiltonian matrix for an isolated SWCNT channel describing the interaction between carbon atoms using tight-binding approximation with nearest neighbor coupling. The self-energy matrices  $\Sigma_1$ ,  $\Sigma_2$  and  $\Sigma_S$  describe how the ballistic channel couples to the metal contacts (Figure 4-1a) and to the scattering process. For a SWCNT channel made of  $N$  carbon atoms, the dimensions of the Hamiltonian matrix are  $N \times N$  [171].

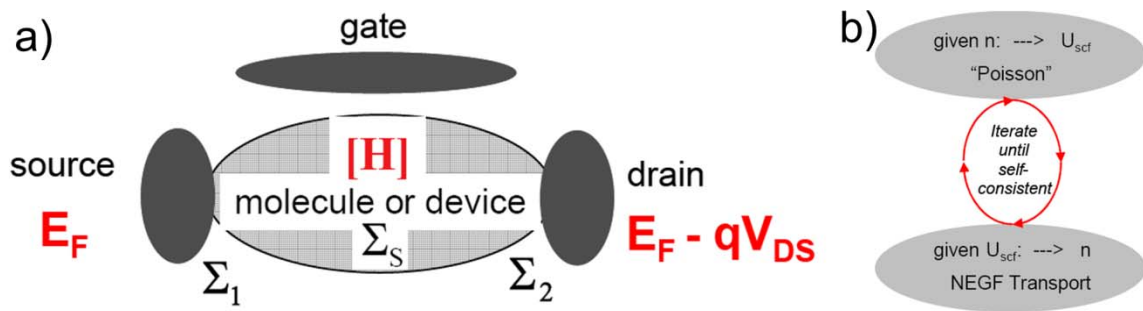


**Figure 4-1: Schematic of the NEGF formalism: a) device representation [171] and b) the self-consistent iterative process [171]. Parameters  $E_F = 0$  and  $V_{DS}$  is the drain voltage.**

Solving eq. (4.1) is not straightforward as it involves an iterative process between the Poisson equation describing the electrostatic potential in the nanotube ( $U_{scf}$ ) and the

NEGF transport equation as depicted in Figure 4-1b. Once the Green's function is known, the source-drain current is then computed as follows [171]:

$$I = \frac{4q}{h} \int \text{Trace}(\Gamma_1 G \Gamma_2 G^*) [f_S(E) - f_D(E)] dE \quad (4.2)$$

where  $\Gamma_{1,2} = i(\Sigma_{1,2} - \Sigma_{1,2}^*)$

where superscript (\*) and parameter  $i$  being the conjugate transpose and the imaginary number. Parameters  $f_{S,D}$  and  $q$  are respectively the source/drain Fermi levels for a given temperature of device operation and electron charge. Simplification of the recursive NEGF model has been achieved using the method of moments [29]. The electrostatic potential is then computed only at the nanotube surface and metal electrodes, and the space between the gate electrode and the CNT surface can be ignored. Further simplifications are achieved by considering CNTFETs to be coaxial [38, 171]. The charge density becomes invariant around the nanotube. Even though this atomistic process reproduces the behavior of the channel accurately, the metal/nanotube junctions are however based on assumptions. To be accurate the NEGF needs to include first principle calculations of the metal/CNT interface [171]. Furthermore incorporation of charge screening effects and coupling between arrays of CNTFETs requires large numbers of unknowns and thus the computation time make it unrealistic for large scale CNTFET analysis and design, at present.

As an alternative to the NEGF approach, various compact models have been reported in recent years [16, 38, 172-176]. The Stanford University CNTFET model introduced by Deng *et al.* [38, 172] allows circuit level implementation of CNTFETs

with a high level of complexity. It opened up the way to circuit design via HSPICE of arrays of CNTFETs in parallel and/or in series in a fast and convenient way. Multiple parameters such as Schottky barriers, screening effects and scattering are also incorporated in the circuit model. This approach however has two major drawbacks. Firstly, it employs a top-gate architecture in which the gate acts only on the central part of the nanotube and away from the drain/source contacts. Compared to most of the current CNTFETs it is unrealistic. Secondly, the central nanotube under the top-gate electrode is connected to the drain/source electrodes via heavily doped CNTs in order to achieve conventional CNTFET behaviors.

A further simplification of the compact models has been achieved by Raychowdhury *et al.* [16]. They used polynomial curves to describe the behavior of the electrostatic potential at the nanotube surface, which alleviates the need to compute the complex Poisson equation. This approach has been validated using numerical models such as NEGF and has been proven to accurately predict device performance [16]. However, the major drawback of this compact model is it relies on fitting parameters at gate voltages above the first conduction band ( $V_g \geq E_{cl}$ ) that are specific for each nanotube diameter and gate insulator thickness/type. Recently, more extreme simplification approaches based on curve fitting of the whole CNTFET device, including eq. 4.2 have also been proposed [177, 178]. These models are however inconvenient and unrealistic because the curve fittings are done for a specific nanotube diameter and length. For CNTFETs of different sizes, the model needs to be redesigned.

The goal of this section is not aimed toward building a novel CNTFET model but rather to use the existing models to investigate and get an insight of the electronic transport in devices made using the colloidal lithography or direct-writing techniques. Considering criteria such as computation time, computer resources, model accuracy, and possibility to adapt the CNTFET model to recreate our experimental conditions, we found the compact models from Raychowdhury *et al.* [16] to be the most suitable. Based on their work, the electrostatic potential experienced by the nanotube can be approximately related to  $V_g$  as follows [16]:

$$\begin{aligned} \psi_S &= V_g && \text{for } V_g < E_{C1} \\ \psi_S &= \alpha(V_g - E_{C1}) && \text{for } V_g \geq E_{C1} \end{aligned} \quad (4.3)$$

where  $\psi_S$ ,  $V_g$ ,  $V_D$ ,  $E_{C1}$  and  $\alpha$  are respectively the electrostatic potential, gate voltage, drain voltage, first conduction band of the SWCNT and a fitting parameter set according to [16]. The total drain current for a ballistic SWCNT at each subband denoted by index  $n$  is expressed as follows [16, 173, 174]:

$$I_{Ballistic} = \frac{4qKT}{h} \sum_n \left[ \log(1 + e^{-\xi_S}) - \log(1 + e^{-\xi_D}) \right] \quad (4.4)$$

where  $\xi_S$  and  $\xi_D$  are defined according to the  $n^{\text{th}}$  conduction band ( $E_{cn}$ ) as follows [16, 173, 174]:

$$\xi_S = \left( \frac{\psi_S - E_{cn}}{KT} \right) \quad (4.5)$$

$$\xi_D = \left( \frac{\psi_S - E_{cn} + qV_D}{KT} \right) \quad (4.6)$$

where  $K$ ,  $h$  and  $T$  are respectively the temperature, Planck's and Boltzmann's constants. The drain current model presented in eq. (4.4) encompasses both the linear regime and the saturation regime. Deviations from the ballistic transport in CNT devices are principally due to a combination of factors such as contact resistance, and elastic and inelastic scatterings within the channel. The first factor is mainly dictated by the Schottky barriers that are created at the metal-SWCNT junctions and it can be written as a triangular potential profile [38, 172, 179]. Using the Wentzel-Kramers-Brillouin (WKB) approximation, the transmission probability can be written as follows [38, 172, 179]:

$$\log T_{SB} = -\frac{8w_{SB}\sqrt{2h_{SB}}}{9d_t\sqrt{E_{cl}}} \quad (4.7)$$

where  $w_{SB}$  and  $h_{SB}$  are respectively the width and the height of the triangular Schottky barrier. For the purpose of the numerical calculations, we employed gold electrodes with a work function of 5.1 eV and SWCNTs were assumed to have a work function of 4.8 eV [79]. These work function values create the highest Schottky barrier for electron tunneling [42]. Although CNTs are theoretically ballistic, elastic and inelastic scattering due to defects in experimental and fabricated CNT devices are often observed [172]. Therefore, scattering within the conductance channel should be considered when calculating the current for a SWCNT. The transmission probability due to elastic scattering is expressed as a function of the channel length ( $L_g$ ) and the effective elastic-scattering ( $l_{eff} = [d_t / 1.5 \text{ nm}] \cdot 200 \text{ nm}$ ) as [38, 172]:

$$T_{ch} = \frac{l_{eff}}{L_g + l_{eff}} \quad (4.8)$$

Contrary to the elastic scattering, the inelastic scatterings depend on the carrier energy and require intraband scattering computations. However, as long as a compact model and device performance approximation are employed, we are assuming that the effective phonon scattering MFPs are equal to the phonon scattering MFPs. Consequently, the total effective inelastic phonon scattering MFP can be written as:

$$l_{in\_eff} = \left[ \lambda_{op}^{-1} + \lambda_{ac}^{-1} \right]^{-1} \quad (4.9)$$

where  $\lambda_{op} \approx 20$  nm and  $\lambda_{ac} \approx 500$  nm are respectively the optical and the acoustic inelastic phonon scattering MFP [38, 42, 172]. The transmission probability of inelastic ( $T_{inSc}$ ) scattering can be computed using eq. 4.8 and eq. 4.9 and now the total drain current for a SWCNT affected by the Schottky barriers and scattering events can be written as follows [180]:

$$I_D = \frac{T_{SB} T_{inSc} T_{ch}}{(1 - R_{inSc} R_{ch}) - R_{SB} (1 - R_{inSc} R_{ch} - T_{inSc} T_{ch})} \cdot I_{Ballistic} \quad (4.10)$$

where  $R_{xx}$  is the reflection probability, whereas subscript (xx) refers either to Schottky barrier (SB), inelastic scattering (inSc) or elastic scattering (ch). The contact resistance is also characterized by the interface resistance and is difficult to quantify as it depends on several variables such as wetting properties of the metal on SWCNT walls (i.e. overlap of electronic states), quality of the contact, cleanness of the surface, etc [96]. In order to

model the performance of CNT devices made using colloidal lithography (see chapter 2) and nanowriting (see chapter 3), numerical calculations are presented first. Based on the RBM spectrum of the Raman spectroscopy and AFM height profiles of the post-growth catalyst samples (see section 2 and 3), we assume that the nanotubes have an average diameter of 1.5 nm. The schematic of a 1.5 nm diameter SWCNT connected to two-terminal gold electrodes is depicted in Figure 4-2a. Schottky barriers are created at each end of the nanotube due to differences in the work functions.

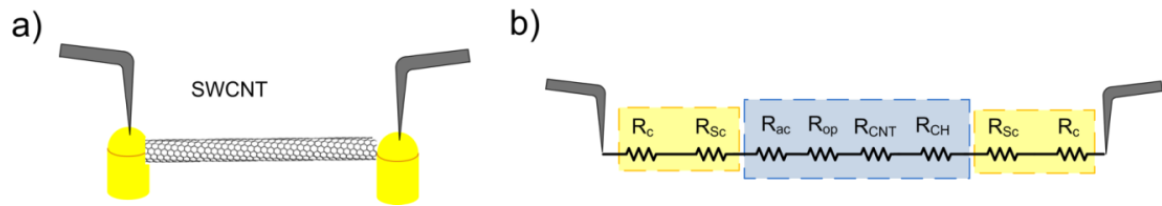


**Figure 4-2: Schematic of the a)  $I$ - $V$  characterization of an isolated SWCNT connected to the drain/source electrodes, and b) its circuit model representation.  $R_c$ ,  $R_{CNT}$ ,  $R_{Sc}$ ,  $R_{op}$ ,  $R_{ac}$ ,  $R_{ch}$  are respectively the contact, nanotube quantum resistance, Schottky barrier, optical, acoustic and elastic resistance.**

Assuming that the electronic transport is performed on an individual and isolated SWCNT as displayed in Figure 4-2a, the voltage drop between the two-terminal probes is  $V_D = [R_{TOT}]I_D$ , with  $R_{TOT}$  being the equivalent circuit resistance (see Figure 4-2b). For this particular setup and  $R_{TOT}$  consists of Schottky barrier resistances ( $R_{Sc}$ ), nanotube quantum resistance ( $R_{CNT}$ ), elastic scattering resistance ( $R_{ch}$ ), contact resistances ( $R_c$ ), optical ( $R_{op}$ ) and acoustic ( $R_{ac}$ ) inelastic resistances. Numerical simulations of a 450 nm long SWCNT-FET are reported in Figure 4-3 for three different scenarios: a) ballistic transport only, b) addition of elastic scatterings within the channel, and c) addition of inelastic scatterings and Schottky barriers.

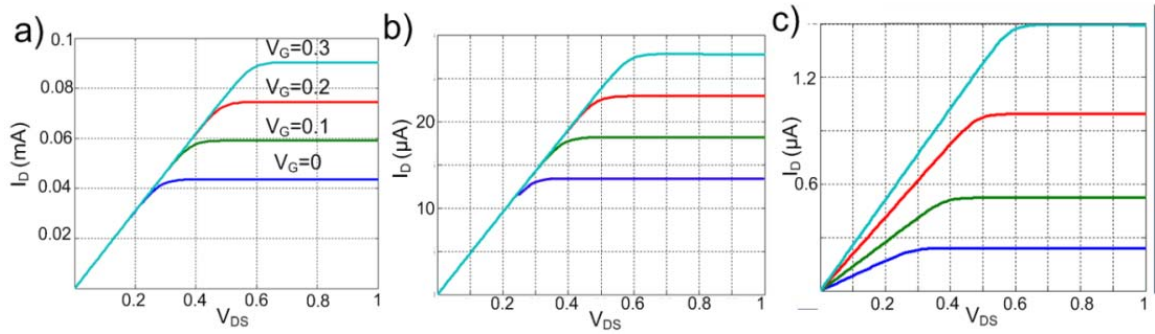


**Figure 4-3: Numerical simulations of a 1.5 nm diameter CNTFET of 450 nm in length considering : a) ballistic transport, b) elastic scattering, and c) elastic scattering, inelastic scatterings and Schottky barriers. Gate voltages are set respective to 0 V (blue), 0.1 V (green), 0.2 V (red), and 0.3 V (cyan).**

The results show a decrease of the channel conductance (increase of resistance) from the maximal quantum conductance of  $\sim 153 \mu\text{S}$  ( $6.5 \text{ k}\Omega$ ) due to Schottky barriers, and elastic and inelastic scatterings within the nanotube. While the quantum conductance is invariant,  $R_{\text{ch}}$ ,  $R_{\text{op}}$  and  $R_{\text{ac}}$  are dependent on the channel length, and  $R_{\text{Sc}}$  is sensitive to the gate voltage. This latter behavior is attributed to the modulation of the Schottky barrier height via gate voltages, which enhance carrier tunneling. From these numerical simulations, the circuit model resistances depicted in Figure 4-2b at each gate voltages are reported in Table 4-1.

**Table 4-1: Resistances of the CNTFET made of a SWCNT of 1.5 nm in diameter and 450 nm in length.**

$V_G$	Device resistances				
	$R_{\text{CNT}} (\text{k}\Omega)$	$R_{\text{ac}} (\text{k}\Omega)$	$R_{\text{CH}} (\text{k}\Omega)$	$R_{\text{op}} (\text{k}\Omega)$	$R_{\text{Schot}} (\text{M}\Omega)$
<b>0.0</b>	6.5	5.5	14.8	118.2	4.37
<b>0.1</b>	6.5	5.5	14.8	118.2	1.67
<b>0.2</b>	6.5	5.5	14.8	118.2	0.73
<b>0.3</b>	6.5	5.5	14.8	118.2	0.47

It should be noted that the experimental  $I$ - $V$  measurements described in the subsequent section were done at  $V_G = 0$ , which implies that the nanotube is assumed to be an active conductance channel or in the “ON” state.

## **4.2 Electronic Transport Measurements**

### **4.2.1 Electronic Transport of the Colloidal Lithography Samples**

Electronic transport characterizations of the post-growth high-yield colloidal lithography samples were achieved via two-terminal current-voltage ( $I$ - $V$ ) measurements using a Keithley 4200-SCS connected to a Janis probe station. Tungsten probe tips of 1  $\mu\text{m}$  nominal diameter were brought into contact with the multilayer metal catalyst at the edge of the hexagonal array as depicted in Figure 4-4a. Optical images in Figure 4-4b and c show the three areas of interest used for the electronic transport measurements. Investigations of these regions via SEM depicted in Figure 4-4d-f revealed large areas of patterned catalyst islands containing SWCNTs.  $I$ - $V$  measurements were initiated by setting one of the probe as an electrical ground (source electrode) while the other as an input (drain electrode). In order to prevent shunt resistances due to the metallic thin film surrounding the hexagonal arrays, we isolated the contact points by physically scratching the areas between them.

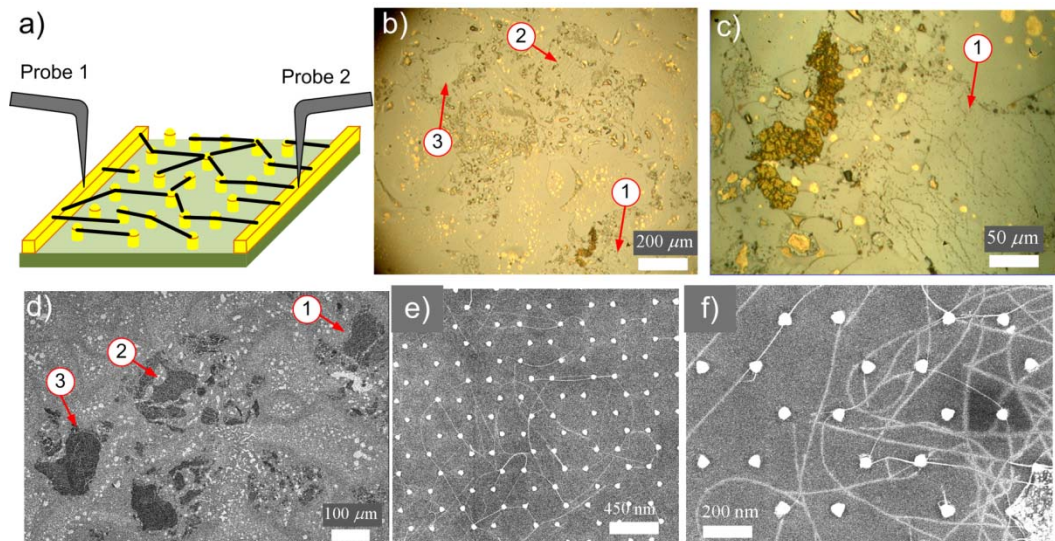


**Figure 4-4:** a) Schematic of the  $I$ - $V$  characterizations of the post-CVD hexagonal arrays. Optical images of the areas of interest of a post-CVD growth hexagonal catalyst islands on Si substrate b) 10X objective, and c) 50X objective. Scanning electron microscopy of d) the three areas, and e-f) close-up of the areas showing thin SWCNT films.

Typical  $I$ - $V$  data, shown in Figure 4-5, display good linearity in the three areas for drain voltage ranging between -1 V to 1 V. We also observed sometimes deviations from ohmic behavior as depicted Figure 4-5a and b. and it is probably due to the effects of contact resistance. Assessment of the results was obtained by performing multiple measurements of the same regions. This was achieved by retracting the probe tips and then bringing them into contact with the gold electrodes.

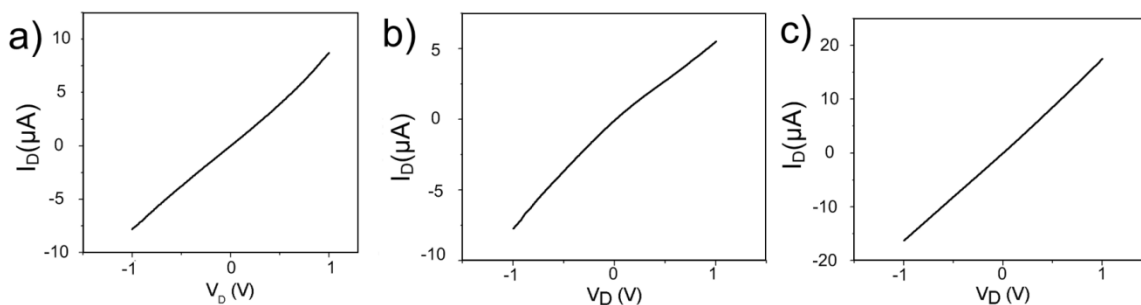


**Figure 4-5:** Two-terminal  $I$ - $V$  measurements of the post-growth hexagonal array evaporated on Si: a) area 1 (see Figure 4-4c), b) area 2 of Figure 4-4d, and c) area 3 of Figure 4-4d.

Two-terminal zero bias conductances and resistances of each area over several measurements are reported in Table 4-2. The large variation observed in the conductance (resistance) of area 3 is mainly due to the contact resistance. By retracting the probe tips and bringing them back into contact with the substrate, the contact resistance is changed. Depending on the measurement locations, many factors such as amorphous carbon, thin film of alumina, cobalt catalyst and even direct path to the undoped Si substrate, are possible candidates for contact resistance.

**Table 4-2: Zero bias conductances and resistances of each area of the post-growth hexagonal catalyst array evaporated on Si substrate.**

Area	Conductance ( $\mu\text{S}$ )	Resistance ( $\text{M}\Omega$ )
1	4.92 - 7.48	0.134 - 0.204
2	1.62 - 6.42	0.156 - 0.617
3	3.37 - 16.5	0.061 - 0.297

Similarly, post-growth hexagonal arrays on Si/SiO<sub>2</sub> substrates were subjected to the two-terminal  $I$ - $V$  measurements. Figure 4-6a shows an optical image of the region under test, and the numbers correspond to the locations of the contact points. The dark orange color area in the optical image corresponds to high density of SWCNTs as depicted in the SEM images of Figure 4-6b-e.

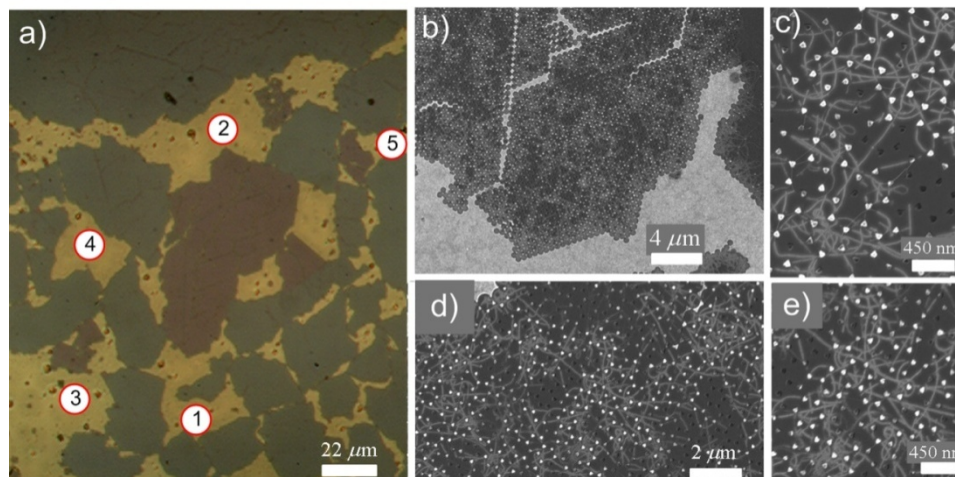


**Figure 4-6: a)** Optical images of the areas of interest of a post-CVD growth hexagonal catalyst islands on Si/SiO<sub>2</sub> substrate 50X objective, and b)-e) scanning electron microscopy of the area of interest showing thin SWCNT films.

Typical  $I$ - $V$  data, shown in Figure 4-7, display good linearity for drain voltages up to  $\pm 1$  V. Results were obtained by performing multiple measurements at the same location. It should be noted that other combinations of contact points were also performed and similar results were observed. Deviations from ohmic behavior can also be seen in Figure 4-7b and c.

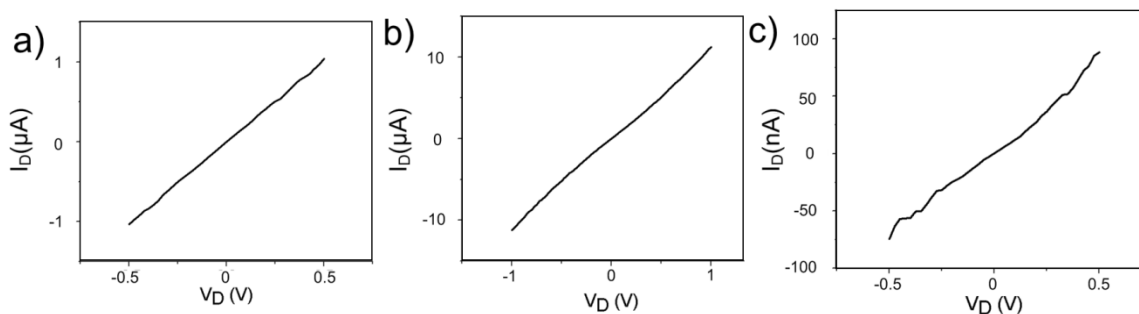


**Figure 4-7: Two-terminal  $I$ - $V$  measurements of the post-growth hexagonal catalyst array evaporated on Si/SiO<sub>2</sub> substrate performed between a) area 1 and 2, b) area 1 and 3, and c) area 4 and 5.**

Two-terminal zero bias conductances and resistances are reported in Table 4-3. The conductance (resistance) is influenced by the same factors mentioned above.

However, in this configuration, current leakages through the substrate are negligible due to the 1  $\mu\text{m}$  thick  $\text{SiO}_2$  layer.

**Table 4-3: Zero bias conductances and resistances for each area of the hexagonal catalyst array on Si/SiO<sub>2</sub>.**

Area	Conductance ( $\mu\text{S}$ )	Resistance ( $\text{M}\Omega$ )
1-2	0.86 - 2.04	0.490 - 1.163
1-3	9.43 - 9.62	0.104 - 0.106
1-4	1.99 - 2.52	0.397 - 0.503
1-5	2.02 - 2.45	0.408 - 0.495
4-5	0.12 - 1.13	0.885 - 8.333

#### 4.2.2 Electronic Transport of the Nanowriting Samples

Post-growth samples patterned via nanowriting were also subjected to the electronic transport characterization. Two-terminal zero bias current-voltage ( $I$ - $V$ ) measurements on the nanotube samples between the patterned catalyst electrodes were performed. Typical  $I$ - $V$  data shown in Figure 4-8 display good linearity and sometimes deviations from the nearly ohmic behavior were also observed (Figure 4-8b and c).

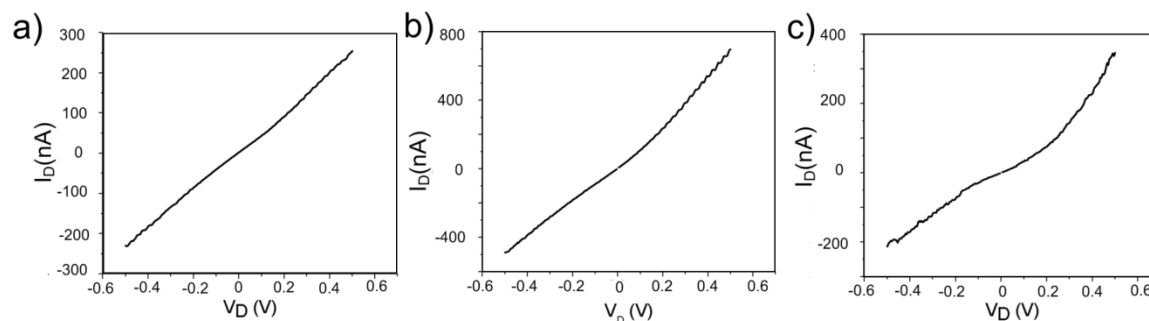


**Figure 4-8: Two-terminal  $I$ - $V$  measurements performed between post-growth  $\text{Al}_2\text{O}_3$ -FeMo catalyst lines.**

Two-terminal conductances and resistances are reported in Table 4-4. Due to the small number of parallel channels between the catalyst lines, the conductance is smaller compared to the hexagonal arrays.

**Table 4-4: Conductances and resistances on the post-growth Al<sub>2</sub>O<sub>3</sub>-FeMo catalyst lines.**

Measurement	Conductance ( $\mu\text{S}$ )	Resistance ( $\text{M}\Omega$ )
# 1	0.41	2.44
# 2	1.00	1.00
# 3	0.27	3.70

If we assume nanotubes of 1.5 nm in diameter were able to grow over lengths of  $\sim 2 \mu\text{m}$  to connect two adjacent catalyst lines, its conductance is  $0.21 \mu\text{S}$  ( $4.75 \text{M}\Omega$ ) using the numerical model. Based on this value and Table 4-4, we estimated the number of SWCNTs forming the channel between one and five.

### 4.2.3 Discussion

A factor that might affect the overall channel conductance of the hexagonal array is the presence of aluminum oxide on the surface. A resistivity as high as  $1 \times 10^{14} \Omega / \text{cm}$  [181] has been reported for this dielectric. Therefore, if we consider the worst case scenario that the whole 10 nm aluminum layer of the multilayer catalyst is oxidized; we should expect an additional serial resistance between each probe and the gold electrodes of  $100 \text{M}\Omega$ . Based on the experimental zero bias resistance, this is clearly not the case. In fact, scratching the surface of the electrode pads using the probe tips did expose the underneath gold layer, and thus the low contact resistance observed.

Using the numerical model presented above, the overall resistance for a 450 nm single long channel is  $\sim 4.51$  M $\Omega$  (see Table 4-1) due to the presence of a Schottky barriers at each metal/nanotube junctions. For a device composed of multiple 450 nm channels as it is the case with the hexagonal arrays, one should expect the total resistance to be much higher. However, the experimental measurements reported in Table 4-2 and Table 4-3, show the opposite behavior due to many SWCNTs being in parallel.

If we compare the hexagonal array approach to other thin film CNTFET approaches depicted in Figure 4-9a and Figure 4-9b, many advantages arise from the configuration of the metals catalyst islands and the way SWCNTs grow on them. Firstly, for the parallel SWCNT array of Figure 4-9a, the total resistance of the channels will be dictated by the elastic and inelastic scattering resistance (evaluated respectively to 143.3 k $\Omega$  and 889.3 k $\Omega$  for a single 4.5  $\mu$ m long SWCNT using the numerical model) and the 4.51 M $\Omega$  Schottky barrier resistance. Even though the scattering process increases, it remains smaller than the tunneling barrier and the conductance will be better. However, the probability of metallic SWCNTs pathways from the source to drain electrodes increases, which will negatively affect the on/off current ratios of the device [161].

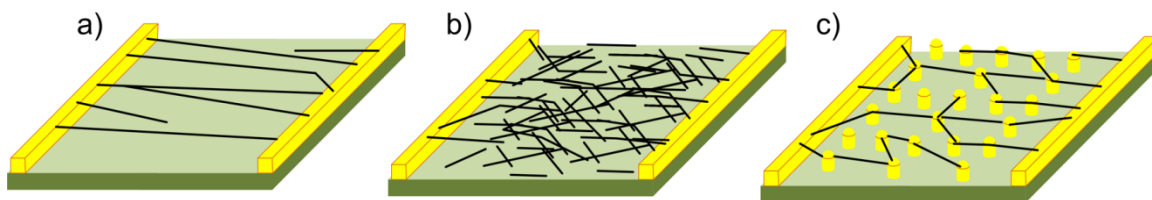


**Figure 4-9: Schematic of a 1.5  $\mu$ m wide and 4.5  $\mu$ m long CNT device made using a) parallel SWCNTs connecting gold electrodes, b) randomly distributed SWCNTs on the substrate, and c) SWCNTs grown via the hexagonal array.**

For randomly distributed SWCNT (Figure 4-9b), the conductance will primarily depend on the inter-tube coupling as continuous conductive channels are unlikely to happen over a distance of 4.5  $\mu\text{m}$ . Stahl *et al.* [182] estimated this inter-coupling resistance to 140 M $\Omega$ , which is thirty times higher than the tunnelling barrier resistance of a SWCNT connected two catalyst islands. This major drawback makes this configuration less attractive compared to the hexagonal array (Figure 4-9c). In contrast with the two other CNTFET approaches, the hexagonal array offers unique advantages: i) knowing that a third of the SWCNTs grown under CVD are metallic, the probability of having continuous metallic channels from the drain to the source is extremely low, and ii) inter-coupling resistances are unlikely to occur. In this configuration, the conductance is mainly dependant on the Schottky barriers created at every catalyst island/nanotube junctions. Since the catalyst islands in this work are small in size, we might expect a reduction of the Schottky barriers height. However, this may not be the case as Ruffino *et al.* [183] reported that Au clusters larger than 7 nm approach the behaviour of the Schottky barriers formed by continuous Au films.

Using the numerical model, we performed some simple calculations on the 1.5  $\mu\text{m}$  wide and 4.5  $\mu\text{m}$  long CNT devices shown in Figure 4-9. For the parallel array, we considered 500 parallel semiconducting SWCNTs of 1.5 nm in diameter and 4.5  $\mu\text{m}$  in length are connecting the source and drain electrodes (i.e. pitch of 3 nm). For the other two approaches, we assumed nine nanotubes in series are forming the 4.5  $\mu\text{m}$  long channel. Screening effects between adjacent nanotubes have been omitted and gate voltage was set to zero.

Numerical results are shown in Figure 4-10. Conductance of the devices depicted in Figure 4-9 is found to be  $94 \mu\text{S}$  ( $10.7 \text{ k}\Omega$ ) for the parallel SWCNTs array,  $12.7 \mu\text{S}$  ( $78.9 \text{ k}\Omega$ ) for the hexagonal array, and  $0.38 \mu\text{S}$  ( $2.61 \text{ M}\Omega$ ) for the randomly distributed SWCNTs. This agrees with the discussion above about the performance of each approach. Even though metallic pathways have not been considered in the numerical model, their presence will directly affect device performance. In contrast to the parallel array device shown in Figure 4-9a, where metallic channels decrease the on/off ratio, the hexagonal approach does not suffer from this issue as the probability of direct metallic pathways between the drain and source electrodes is extremely low. Experimentally, a third of the SWCNTs grown via colloidal lithography are metallic (see section 1.2). Therefore we expect a decrease of the number of Schottky barrier resistances in the device and device channel length due to metallic pathways within the hexagonal array. For this reason, compared to numerical device performance, the experimental electronic transport within hexagonal array CNT devices could be better.

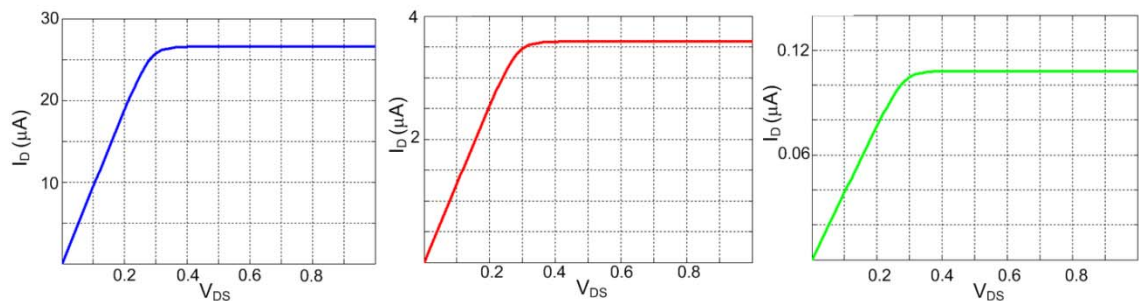


**Figure 4-10: Matlab numerical simulations of a  $1.5 \mu\text{m}$  wide and  $4.5 \mu\text{m}$  long CNT device made of  $1.5 \text{ nm}$  diameter SWCNTs: a) parallel SWCNTs connecting gold electrodes (Figure 4-9a), b) SWCNTs grown via the hexagonal array of (Figure 4-9c), and c) thin film of SWCNTs randomly distributed on the substrate (Figure 4-9b).**

Decrease in the conductance of the nanowriting samples is due to the same factors described above: interface resistances, Schottky barriers, amorphous carbon and cleanness of the surface. In contrast to the hexagonal array, solely catalyst lines were used as electrodes, and depending on the measurement locations, one should expect a mixture of iron, iron carbide and alumina as conduction path between the nanotubes and the tip probes.

### 4.3 Summary

In summary, two-terminal  $I$ - $V$  measurements on post-growth colloidal lithography and nanowriting samples were performed. Results show mostly ohmic behavior with conductances of  $\sim 0.86$ - $16.5 \mu\text{S}$  for the hexagonal catalyst array (combining Si and Si/SiO<sub>2</sub> samples) and  $0.27$ - $1 \mu\text{S}$  for the nanowriting samples. Decrease of the channel conductance has been attributed to the quality and cleanness of the contacts, and the presence of Schottky barriers at each nanotube/metal junction. In addition, compact models have been used to compare the electronic transport in devices made via colloidal lithography to devices fabricated using parallel or randomly distributed SWCNTs. Through this comparison, insights into the device performance and the unique advantages of the hexagonal array approach were possible. The experimental and numerical electronic transport characterizations allow thorough nanoscale investigation of device performance. Ultimately this will assist design and fabrication of better CNT devices as required for nanoelectronics.

## 5 Conclusion and Future Work

In this thesis, two new techniques for SWCNT catalyst patterning and growth have been presented. These methods are also in principle compatible with the silicon planar processing used to manufacture integrated circuits.

Firstly, colloidal lithography has been used to pattern SWCNT multilayer catalyst on Si and Si/SiO<sub>2</sub> substrates. In order to do so, nanospheres were used as a shadow mask during metal catalyst evaporation which resulted in large areas of periodic catalyst islands. CVD growth resulted in aligned SWCNTs within the hexagonal catalyst array that appeared to be along the  $\langle 110 \rangle$  crystal directions of the Si substrates, while on Si/SiO<sub>2</sub>, SWCNTs were found to connect the catalyst islands in a network-like structure. Such aligned growth is still not yet fully understood but has been attributed to the combination of electrostatic interaction, van der Waals interaction, silicide formation and gas flow. A growth model based on experimental data has been presented in order to explain the contribution of the hexagonal array to SWCNT alignment on Si/SiO<sub>2</sub>. Further investigations are needed to understand the alignment of nanotubes on the plain Si

substrate and the contribution of silicides on CNT growth. Due the advantages of colloidal lithography of being an inexpensive and fast process that allows high control over the mask opening, it may be reliable method of patterning periodic and nanoscale catalyst islands for carbon nanotube growth. This work also contributes to the investigation and understanding of CNT growth at the nanoscale level as required for nanoelectronic applications.

A novel method based on direct-nanowriting of liquid catalyst has also been demonstrated as a potential technique to produce nanoscale catalyst geometries in a highly controlled manner for CNT growth and applications. SWCNT growth on the patterned regions was demonstrated via CVD and provided insight into the catalyst nanowriting process and nanotube yield. Our results highlight nanowriting as an effective method to directly write precise catalyst shapes for nanotube growth, in a convenient manner that is not specific to a particular type of catalyst or substrate. Furthermore, nanowriting was also used to pattern carbon based materials such as SWCNTs and C<sub>60</sub> molecules on Si and Si/SiO<sub>2</sub>. Nanowriting allows the controlled nanoscale deposition of catalyst into predefined patterns for the creation of functional CNT architectures and their integration into devices.

Investigations of the electronic transport in devices made via colloidal lithography and nanowriting were made to gain insight into the conductance mechanisms and aid device design. Two-terminal  $I$ - $V$  measurements on post-growth colloidal lithography and nanowriting samples were performed and results show mainly ohmic behavior with

conductances between 0.18-17.5  $\mu\text{S}$ . The channel conductance is correlated to the contact resistance that arises from the Schottky barrier resistances, and to the quality and cleanness of the contacts. Numerical calculations using available compact models have been used to demonstrate the unique advantages of the hexagonal array approach. Such examination will allow better nanoscale design and efficient fabrication of CNT devices.

## **5.1 Future Work**

Future work should focus on many aspects ranging from the growth mechanism and alignment of SWCNT to building electronic devices using the patterning methods presented in this thesis.

### **5.1.1 Single-Walled Carbon Nanotube Catalyst Patterning Methods**

Even though the alignment of SWCNTs within the hexagonal arrays has been addressed via a growth model, many aspects are still unclear. In particular, the contribution of silicide structures to the SWCNT growth has not yet been understood. Therefore, more advanced structural characterization techniques of the samples and structures are needed:

- Transmission electron microscopy of the samples could provide important information regarding the interaction of nanotube with silicide and the Si substrate. However, transferring the aligned SWCNTs along the  $\langle 110 \rangle$  family of the undoped silicon substrates to carbon grids without losing the alignment and/or damaging the tube is highly challenging.

- Scanning tunneling microscopy is the ideal characterization tool for these particular samples due to its atomic resolution. Structural characterization of the potential nanotube/silicide junctions will shed light on the growth mechanism and the interaction between silicides and nanotubes. Until now, no one has performed such investigation on samples showing clear silicide/nanotube interactions.
- Another way of investigating the structural composition of these nanostructures is via electronic transport measurements using a three-terminal setup. Gate voltage dependence of the  $I$ - $V$  curves will reveal nanotube types. However, due to the features sizes, conventional photolithography is challenging and advanced techniques are needed. Electron-beam lithography could be used to pattern nanometer scale electrodes on top of the nanotubes but one should also expect performance deterioration due to the damaging high energy electron beam.

The alignment mechanism proposed in this thesis gives only a glimpse of the electrostatic interactions involved within the catalyst islands. A more complex model using multiple active catalyst islands should be considered. The effect of the catalyst island separation as a function of the alumina thickness (and therefore charge density) on the nanotube alignments needs to be addressed as well. Future work should also focus on optimizing SWCNT growth. High yield growth can hinder SWCNT alignment due to inter-tube interactions, whereas at low yield growth, only sporadic aligned SWCNTs are observed. An ideal SWCNT growth recipe will yield dense SWCNT films showing alignment along preferential directions.

Turning now to direct-writing of CNT catalyst in liquid form, the method shown here is serial in nature, but it can be extended to multiple parallel pens or pipettes for increased throughput [25]. Another way to control the pattern dimensions via nanowriting can be achieved by changing the wetting properties of the nanopipette tip. As one can notice in the simulation using Surface Evolver [184] of Figure 5-1, a hydrophobic tip surface will yield larger patterns, while a hydrophilic one will prevent the liquid solution from spreading on the surface, if the appropriate tip height is used. Furthermore, the liquid meniscus will interact with the nanopipette outer wall [185] and consequently this factor needs to be considered.

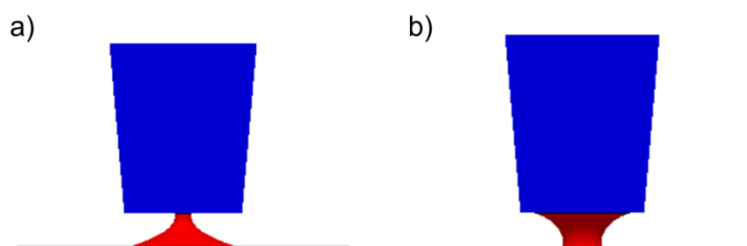


**Figure 5-1: Simulation using Surface Evolver [184] of the effect of the wetting properties of the tip surface on the pattern dimensions: a) hydrophobic tip surface, and b) hydrophilic tip surface.**

Nanowritten ferritin samples showed little or no SWCNT growth. Therefore, modification and optimization of the growth conditions is needed. Recently, a new growth recipe for ferritin showing higher SWCNT yield has been reported and consists of [186]:

1. Calcination at 800 °C,
2. Preheat from room temperature to 925 °C under 120 sccm of H<sub>2</sub>,

3. Growth under 1500 sccm of CH<sub>4</sub> and 120 sccm of H<sub>2</sub>, and
4. Cool down under Ar.

It was shown that the nanotubes tend to connect parallel catalyst lines due to either electrostatic interaction or simply van der Waals forces. Eventually, more complex and arbitrary catalyst geometries are needed to investigate their role in the alignment of nanotubes during the growth process.

In terms of SWCNT solutions for direct CNT deposition/patterning, clogging of the nanopipettes and tangling of the tubes are the main issues for the nanowriting process. Future work should focus on shortening of the carbon nanotubes and functionalization of the tube for better dispersion. Ultimately, steps of centrifugation and filtration of the CNT solutions using glass wool or other approaches should be attempted.

### **5.1.2 Single-Walled Carbon Nanotube Electronic Devices**

In the electronic transport model we have only considered simple tunneling through Schottky barriers. Future work should focus on studying the effects of the gate and the drain on the overall performance of the CNT devices. Consequently, a more complex model treating the modulation of the Schottky barriers at the drain/source junctions by the gate voltage and the drain electrodes is needed. In this particular case, the surface potential can no longer be considered as linear as it was assumed in the thesis. Other factors such as channel length should be considered. In fact, shorter nanotube channels will experience a Schottky barrier modulation at both ends by the drain, while

for longer SWCNTs the drain will only be affecting the Schottky barriers at the drain side [187]. Charge screening caused by adjacent SWCNTs should also be investigated, especially for thin SWCNT films.

As the main factor influencing channel conductance is often the contact resistance, reducing this resistance is a major priority. One way of solving the problem is to pattern a new layer of gold on top of the existing electrodes using, for example, photolithography and e-beam evaporation. However, this does not eliminate amorphous carbon and/or alumina from the underlying layer. Additional steps of cleaning the electrodes should be considered. Methods such as electron cyclotron resonance (ECR) may be used to clean the surface while protecting the nanotubes with photoresist. Another simple approach consists of annealing the samples to reduce the contact resistance between the nanotubes and the electrodes. This step however also does not eliminate amorphous carbon or alumina layer.

Ultimately, three-terminal electronic devices should be fabricated. Back-gate configuration is the most straightforward approach to make CNTFETs as the underlying heavily doped Si substrate can be used as a gate (see Figure 5-2a). However as discussed in Section 1.7, this design is inconvenient for large scale electronic device integration and therefore a top-gate CNTFET architecture should be introduced. In this configuration, a gate is patterned on top of a thin SiO<sub>2</sub> or SiN<sub>4</sub> layer deposited, for example, via plasma-enhanced chemical vapor deposition (PECVD) (see Figure 5-2b). The nanotubes are then protected from outside elements. This approach can also be extended to the nanowriting

samples in the same manner. Fabrication of more complex CMOS devices can be achieved by *n*- or *p*-doping of the nanotubes prior to top-gate patterning, etc.

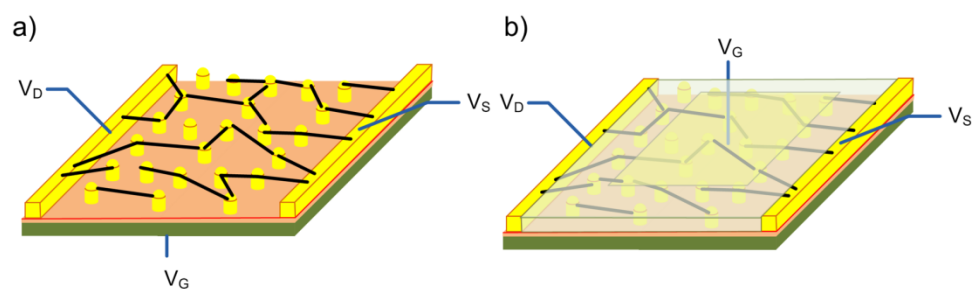


**Figure 5-2: Schematic of hexagonal array three-terminal CNTFET devices using a) a back-gate electrode, and b) a top-gate electrode patterned on top of SiO<sub>2</sub> or SiN<sub>4</sub>.**

## 6 Bibliography

- [1] M. Monthieux, and V. L. Kuznetsov, "Who Should Be Given The Credit for The Discovery of Carbon Nanotubes?," *Carbon*, vol. 44, pp. 1621, 2006.
- [2] S. Iijima, "Helical microtubules of graphitic carbon," *Nature*, vol. 354, no. 6348, pp. 56-58, 1991.
- [3] S. Iijima, and T. Ichihashi, "Single-shell carbon nanotubes of 1-nm diameter," *Nature*, vol. 363, no. 6430, pp. 603-605, 1993.
- [4] D. S. Bethune, C. H. Klang, M. S. de Vries *et al.*, "Cobalt-catalysed growth of carbon nanotubes with single-atomic-layer walls," *Nature*, vol. 363, no. 6430, pp. 605-607, 1993.
- [5] I. Wako, T. Chokan, D. Takagi *et al.*, "Direct observation of single-walled carbon nanotube growth processes on SiO<sub>2</sub> substrate by in situ scanning electron microscopy," *Chemical Physics Letters*, vol. 449, no. 4-6, pp. 309-313, 2007.
- [6] A. R. Graham, G. S. Duesberg, R. V. Seidel *et al.*, "Carbon nanotubes for microelectronics?," *Small*, vol. 1, no. 4, pp. 382-90, 2005.
- [7] M. Bohr, "The New Era of Scaling in an SoC World," in IEEE International Solid-State Circuits Conference, 2009.
- [8] R. Chau, B. Doyle, S. Datta *et al.*, "Integrated Nanoelectronics for The Future," *Nature Materials*, vol. 6, pp. 810-812, 2007.
- [9] IBM. "Catch me if you can!, 2006,"  
<http://www.zurich.ibm.com/news/06/moleculeswitch.html>.
- [10] T. H. Ning, "GLSVLSI 2008 invited/keynote talk," in Proceedings of the 18th ACM Great Lakes symposium on VLSI, Orlando, Florida, USA, 2008.
- [11] Becta. "Hardware analysis: Processor futures, 2008,"  
<http://emergingtechnologies.becta.org.uk/index.php?section=etn&rid=14153>.
- [12] L. Peters. "Multigate FETs: A Risky Proposition, 2008,"  
[http://www.semiconductor.net/article/199881-Multigate\\_FETs\\_A\\_Risky\\_Proposition.php](http://www.semiconductor.net/article/199881-Multigate_FETs_A_Risky_Proposition.php).
- [13] B. Doyle, B. Boyanov, S. Datta *et al.*, "Tri-Gate fully-depleted CMOS transistors: fabrication, design and layout," *Symposium on VLSI Technology*, pp. 133-134, 2003.
- [14] I. Ferain, R. Duffy, N. Collaert *et al.*, "Performance improvement in narrow MuGFETs by gate work function and source/drain implant engineering," *Solid-State Electronics*, vol. 53, no. 7, pp. 760-766, 2009.
- [15] H. Khan, D. Mamaluy, and D. Vasileska, "Fully 3D self-consistent quantum transport simulation of Double-gate and Tri-gate 10 nm FinFETs," *Journal of Computational Electronics*, vol. 7, no. 3, pp. 346-349, 2008.
- [16] A. Raychowdhury, S. Mukhopadhyay, and K. Roy, "A Circuit-Compatible Model of Ballistic Carbon Nanotube Field-Effect Transistors," *IEEE Transactions on Computer-Aided Design of Integrated Circuits and Systems*, vol. 23, no. 10, pp. 1411-1420, 2004.

- [17] P. Gargini. "Intel Nanotechnology Overview, 2004," [http://www.intel.com/technology/silicon/post\\_CMOS.htm](http://www.intel.com/technology/silicon/post_CMOS.htm).
- [18] A. M. Thayer. "Carbon Nanotubes By The Metric Ton: Anticipating New Commercial Applications, Producers Increase Capacity, 2007," <http://pubs.acs.org/cen/business/85/8546bus1.html>.
- [19] P. C. Eklund, P. M. Ajayan, R. Blackmon *et al.*, *International Assessment of Carbon Nanotube Manufacturing and Applications*, World Technology Evaluation Center, 2007.
- [20] R. Saito, G. Dresselhaus, and M. S. Dresselhaus, *Physical Properties of Carbon Nanotubes* Imperial College Press, 1998.
- [21] S. Ege, *Organic Chemistry: Structure and Reactivity*, 4th ed., Boston: Houghton Nifflin Company, 1999.
- [22] A. Loiseau, P. Launois, P. Petit *et al.*, *Understanding Carbon Nanotubes: from Basics to Application*, Berlin Heidelberg: Springer, 2006.
- [23] Y. Yoon, J. M. Fodor, J. Guo *et al.*, CNTbands Tool v.2.2 available for free at [www.nanohub.org](http://www.nanohub.org), 2009.
- [24] H. C. Chuan, "Modeling and Analysis of Ballistic Carbon Nanotube Field Effect Transistor (CNTFET) with Quantum Transport Concept," Faculty of Electrical Engineering, Universiti Teknologi Malaysia, 2007.
- [25] T. S. Jespersen, "Raman Scattering in Carbon Nanotubes," Nels Bohr Institute for Astronomy, Physics and Geophysics, University of Copenhagen, Copenhagen, 2003.
- [26] J. C. Charlier, P. C. Eklund, J. Zhu *et al.*, "Electron and phonon properties of graphene: their relationship with carbon nanotubes," *Carbon Nanotubes. Advanced Topics in the Synthesis, Structure, Properties and Applications*, pp. 673-709, Berlin, Germany: Springer-Verlag, 2008.
- [27] M. T. Ahmadi, R. Ismail, M. L. P. Tan *et al.*, "The Ultimate Ballistic Drift Velocity in Carbon Nanotubes," *Journal of Nanomaterials*, vol. 2008, pp. 8, 2008.
- [28] H. Dai, "Nanotube Growth and Characterization," *Carbon Nanotubes: Synthesis, Structure, Properties and Application*, p. 29, 2001.
- [29] J. Deng, A. Lin, G. C. Wan *et al.*, "Carbon Nanotube Transistor Compact Model for Circuit Design and Performance Optimization," *ACM Journal on Emerging Technologies in Computing Systems* vol. 4, no. 2, pp. 7:1-7:20, 2008.
- [30] C. L. Venema, *Electronic Structure of Carbon Nanotube*: Delft University Press, 2000.
- [31] R. E. Smalley, M. S. Dresselhaus, G. Dresselhaus *et al.*, *Carbon Nanotubes: Synthesis, Structure, Properties, and Applications*: Springer, 2001.
- [32] S. Maruyama. "1D DOS (van Hove singularity), 2002," [http://www.photon.t.u-tokyo.ac.jp/~maruyama/kataura/1D\\_DOS.html](http://www.photon.t.u-tokyo.ac.jp/~maruyama/kataura/1D_DOS.html).
- [33] J. W. G. Wildoer, L. C. Venema, A. G. Rinzler *et al.*, "Electronic structure of atomically resolved carbon nanotubes," *Nature*, vol. 391, no. 1, pp. 59-62, 1998.
- [34] M. Glerup, V. Krstic, C. P. Ewels *et al.*, *Doping of Carbon Nanotubes*: To appear in "Doped Nanomaterials and Nanodevices", edited by Wei Chen (in press, 2008). 2008.

- [35] S. Ilani, L. A. K. Donev, M. Kindermann *et al.*, "Measurement of the quantum capacitance of interacting electrons in carbon nanotubes," *Nature Physics*, vol. 2, no. 687-691, 2006.
- [36] T. Belin, and F. Epron, "Characterization methods of carbon nanotubes: a review," *Materials Science and Engineering*, vol. 119, pp. 105-118, 2005.
- [37] S. M. Bachilo, M. S. Strano, C. Kittrell *et al.*, "Structure-Assigned Optical Spectra of Single-Walled Carbon Nanotubes," *Science*, vol. 298, pp. 2361-2366, 2002.
- [38] J. Deng, and H. S. P. Wong, "A compact SPICE model for carbon-nanotube field-effect transistors including nonidealities and its application - part I: model of the intrinsic channel region," *IEEE Transactions on Electron Devices*, vol. 54, no. 12, pp. 3186-94, 2007.
- [39] P. Avouris, Z. Chen, and V. Perebeinos, "Carbon-based electronics," *Nature Nanotechnology*, vol. 2, no. 10, pp. 605-615, 2007.
- [40] S. Heinze, J. Tersoff, and P. Avouris, "Carbon Nanotube Electronics and Optoelectronics," *Introducing Molecular Electronics*, pp. 381-409, 2005.
- [41] D. Mann, A. Javey, K. Jing *et al.*, "Ballistic transport in metallic nanotubes with reliable Pd ohmic contacts," *Nano Letters*, vol. 3, no. 11, pp. 1541-4, 2003.
- [42] M. J. Biercuk, S. Ilani, C. M. Marcus *et al.*, "Electrical Transport in Single Wall Carbon Nanotubes," *Carbon Nanotubes*, pp. 455-493, 2008.
- [43] W. Liang, M. Bockrath, D. Bozovic *et al.*, "Fabry - Perot interference in a nanotube electron waveguide," *Nature*, vol. 411, no. 6838, pp. 665-669, 2001.
- [44] P. Avouris, J. Appenzeller, R. Martel *et al.*, "Carbon nanotube electronics," *Proceedings of the IEEE*, vol. 91, no. 11, pp. 1772-1784, 2003.
- [45] M. S. Dresselhaus, G. Dresselhaus, R. Saito *et al.*, "Raman Spectroscopy of Carbon Nanotubes," *Physics Reports*, vol. 409, pp. 47, 2004.
- [46] M. S. Dresselhaus, and P. C. Eklund, "Phonons in carbon nanotubes," *Advances in Physics*, vol. 49, no. 6, pp. 705-814, 2000.
- [47] C. V. Raman, and K. S. Krishnan, "A New Type of Secondary Radiation," *Nature*, vol. 121, 1928.
- [48] A. Jorio, M. A. Pimenta, A. G. Souza Filho *et al.*, "Characterizing carbon nanotube samples with resonance Raman scattering," *New Journal of Physics*, no. 5, pp. 139.1-139.17, 2003.
- [49] A. M. Rao, J. Chen, E. Richter *et al.*, "Effect of van der Waals interactions on the Raman modes in single walled carbon nanotubes," *Physical Review Letters*, vol. 86, no. 17, pp. 3895-8, 2001.
- [50] L. G. Cancado, K. Takai, T. Enoki *et al.*, "General equation for the determination of the crystallite size  $L_{[a]}$  of nanographite by Raman spectroscopy," *Applied Physics Letters*, vol. 88, no. 16, pp. 163106-3, 2006.
- [51] R. G. Lacerda, A. S. Teh, M. H. Yang *et al.*, "Growth of high-quality single-wall carbon nanotubes without amorphous carbon formation," *Applied Physics Letters*, vol. 84, no. 2, pp. 269-271, 2004.
- [52] M. S. Dresselhaus, G. Dresselhaus, A. Jorio *et al.*, "Raman spectroscopy on isolated single wall carbon nanotubes," *Carbon*, vol. 40, no. 12, pp. 2043-61, 2002.
- [53] E. Lamouroux, P. Serp, and P. Kalck, "Catalytic Routes Towards Single Wall Carbon Nanotubes," *Catalysis Reviews*, vol. 49, no. 3, pp. 341 - 405, 2007.

- [54] V. Vinciguerra, F. Buonocore, G. Panzera *et al.*, “Growth mechanisms in chemical vapour deposited carbon nanotubes,” *Nanotechnology*, vol. 14, pp. 655–660, 2003.
- [55] M. Lin, J. P. Ying Tan, C. Boothroyd *et al.*, “Direct Observation of Single-Walled Carbon Nanotube Growth at the Atomistic Scale,” *Nano Letters*, vol. 6, no. 3, pp. 449-452, 2006.
- [56] K. B. K. Teo, C. Singh, M. Chhowalla *et al.*, “Catalytic Synthesis of Carbon Nanotubes and Nanofibers,” *Encyclopedia of Nanoscience and Nanotechnology*, vol. 1, pp. 665-686, 2004.
- [57] R. Seidel, G. S. Duesberg, E. Unger *et al.*, “Chemical Vapor Deposition Growth of Single-Walled Carbon Nanotubes at 600 °C and a Simple Growth Model,” *Journal of Physical Chemistry B*, vol. 108, no. 6, pp. 1888-1893, 2004.
- [58] D. E. Resasco, “Kinetic Modeling of Single-Walled Carbon Nanotube Growth on Co-Mo/SiO<sub>2</sub> Catalysts with Same-Particle Characterization of Catalysts and Product,” in MRS Spring Meeting 2008, San Francisco, CA, 2008.
- [59] D. Ogrin, R. Colorado Jr, B. Maruyama *et al.*, “Single-walled carbon nanotube growth using [Fe<sub>3</sub>(3-O)(-O<sub>2</sub>CR)<sub>6</sub>(L)<sub>3</sub>]<sup>n+</sup> complexes as catalyst precursors,” *Dalton Transactions*, no. 1, pp. 229-236, 2006.
- [60] M. Lin, J. P. Y. Tan, C. Boothroyd *et al.*, “Direct observation of single-walled carbon nanotube growth at the atomistic scale,” *Nano Letters*, vol. 6, no. 3, pp. 449-452, 2006.
- [61] C. T. Wirth, S. Hofmann, J. Robertson *et al.*, “In-situ Time-resolved XPS Study of Catalyst Behavior During Carbon Nanotube Growth,” in MRS Spring Meeting 2008, San Francisco, CA, 2008.
- [62] A.-D. Dupuis, “The catalyst in the CCVD of carbon nanotubes—a review,” *Progress in Materials Science*, vol. 50, pp. 929-961, 2005.
- [63] J. M. Simmons, B. M. Nichols, M. S. Marcus *et al.*, “Critical Oxide Thickness for Efficient Single-Walled Carbon Nanotube Growth on Silicon Using Thin SiO<sub>2</sub> Diffusion Barriers,” vol. 7, no. 2, pp. 902-909, 2006.
- [64] P. Nikolaev, M. J. Bronikowski, R. K. Bradley *et al.*, “Gas-phase catalytic growth of single-walled carbon nanotubes from carbon monoxide,” *Chemical Physics Letters*, vol. 313, pp. 91-97, 1999.
- [65] K. Hata, D. N. Futaba, K. Mizuno *et al.*, “Water-Assisted Highly Efficient Synthesis of Impurity-Free Single-Walled Carbon Nanotubes,” *Science*, vol. 306, no. 5700, pp. 1362-1364, November 19, 2004, 2004.
- [66] H. Cui, G. Eresa, J. Y. Howeib *et al.*, “Growth behavior of carbon nanotubes on multilayered metal catalyst film in chemical vapor deposition” *Chemical Physics Letters*, vol. 374, no. 3, pp. 222-228, 2003.
- [67] N. R. Franklin, and H. Dai, “An enhanced CVD approach to extensive nanotube networks with directionality,” *Advanced Materials*, vol. 12, no. 12, pp. 890-4, 2000.
- [68] J. Kong, H. T. Soh, A. M. Cassell *et al.*, “Synthesis of individual single-walled carbon nanotubes on patterned silicon wafers,” *Nature*, vol. 395, no. 6705, pp. 878-81, 1998.

- [69] J. Kong, C. Zhou, A. Morpurgo *et al.*, "Synthesis, integration, and electrical properties of individual single-walled carbon nanotubes," *Applied Physics A: Materials Science & Processing*, vol. 69, no. 3, pp. 305-308, 1999.
- [70] O. Byung Seok, M. Yo-Sep, B. Eun Ju *et al.*, "Fabrication of suspended single-walled carbon nanotubes via a direct lithographic route," *Journal of Materials Chemistry*, vol. 16, no. 2, pp. 174-8, 2006.
- [71] L. M. Huang, Z. Jia, and S. O'Brien, "Orientated assembly of single-walled carbon nanotubes and applications," *Journal of Materials Chemistry*, vol. 17, no. 37, pp. 3863-3874, 2007.
- [72] S. Huang, B. Maynor, X. Cai *et al.*, "Ultralong, Well-Aligned Single-Walled Carbon Nanotube Architectures on Surfaces," *Advanced Materials*, vol. 15, no. 19, pp. 1651-1655, 2003.
- [73] Z. Yu, S. Li, and P. J. Burke, "Synthesis of aligned arrays of millimeter long, straight single-walled carbon nanotubes," *Chemistry of Materials*, vol. 16, no. 18, pp. 3414-3416, 2004.
- [74] R. G. Lacerda, A. S. Teh, M. H. Yang *et al.*, "Growth of high-quality single-wall carbon nanotubes without amorphous carbon formation," *Applied Physics Letters*, vol. 84, no. 2, pp. 269-71, 2004.
- [75] X. Wang, A. Volodin, C. Van Haesendonck *et al.*, "Controllable growth of individual, uniform carbon nanotubes by thermal chemical vapor deposition," *Physica E: Low-Dimensional Systems and Nanostructures*, vol. 25, no. 4, pp. 597-604, 2005.
- [76] R. Seidel, M. Liebau, G. S. Duesberg *et al.*, "In-Situ Contacted Single-Walled Carbon Nanotubes and Contact Improvement by Electroless Deposition," *Nano Letters*, vol. 3, no. 7, pp. 965-968, 2003.
- [77] H. Ago, K. Nakamura, K.-i. Ikeda *et al.*, "Aligned growth of isolated single-walled carbon nanotubes programmed by atomic arrangement of substrate surface," *Chemical Physics Letters*, vol. 408, no. 4-6, pp. 433-438, 2005.
- [78] M. Su, Y. Li, B. Maynor *et al.*, "Lattice-Oriented Growth of Single-Walled Carbon Nanotubes," *Journal of Physical Chemistry B*, vol. 104, no. 28, pp. 6505-6508, 2000.
- [79] Q. Yu, G. Qin, H. Li *et al.*, "Mechanism of Horizontally Aligned Growth of Single-Wall Carbon Nanotubes on R-Plane Sapphire," *Journal of Physical Chemistry B*, vol. 110, no. 45, pp. 22676-22680, 2006.
- [80] H. Ago, N. Uehara, K.-i. Ikeda *et al.*, "Synthesis of horizontally-aligned single-walled carbon nanotubes with controllable density on sapphire surface and polarized Raman spectroscopy," *Chemical Physics Letters*, vol. 421, no. 4-6, pp. 399-403, 2006.
- [81] S. Han, X. Liu, and C. Zhou, "Template-Free Directional Growth of Single-Walled Carbon Nanotubes on a- and r-Plane Sapphire," *J. Am. Chem. Soc.*, vol. 127, no. 15, pp. 5294-5295, 2005.
- [82] C. Kocabas, S. H. Hur, A. Gaur *et al.*, "Guided growth of large-scale, horizontally aligned arrays of single-walled carbon nanotubes and their use in thin-film transistors," *Small*, vol. 1, no. 11, pp. 1110-16, 2005.

- [83] S. Jeon, C. Lee, J. Tang *et al.*, "Growth of serpentine carbon nanotubes on quartz substrates and their electrical properties," *Nano Research*, vol. 1, no. 5, pp. 427-433, 2008.
- [84] D. Yuan, L. Ding, H. Chu *et al.*, "Horizontally Aligned Single-Walled Carbon Nanotubes on Quartz from a Large Variety of Metal Catalysts," *Nano Letters*, vol. 8, no. 8, pp. 2576-2579, 2008.
- [85] Y. Yao, X. Dai, C. Feng *et al.*, "Crinkling Ultralong Carbon Nanotubes into Serpentes by a Controlled Landing Process," *Advanced Materials*, 2009 (*in press*).
- [86] N. Geblinger, A. Ismach, and E. Joselevich, "Self-organized nanotube serpentes," *Nat Nano*, vol. 3, no. 4, pp. 195-200, 2008.
- [87] C. Kocabas, S. J. Kang, T. Ozel *et al.*, "Improved Synthesis of Aligned Arrays of Single-Walled Carbon Nanotubes and Their Implementation in Thin Film Type Transistors" *The Journal of Physical Chemistry C*, vol. 111, no. 48, pp. 17879-17886, 2007.
- [88] A. Ural, Y. Li, and H. Dai, "Electric-field-aligned growth of single-walled carbon nanotubes on surfaces," *Applied Physics Letters*, vol. 81, no. 18, pp. 3464-3466, 2002.
- [89] A. Nojeh, A. Ural, R. F. Pease *et al.*, "Electric-field-directed growth of carbon nanotubes in two dimensions," *Journal of Vacuum Science and Technology B: Microelectronics and Nanometer Structures*, vol. 22, no. 6, pp. 3421-3425, 2004.
- [90] Y. Zhang, A. Chang, J. Cao *et al.*, "Electric-field-directed growth of aligned single-walled carbon nanotubes," *Applied Physics Letters*, vol. 79, no. 19, pp. 3155-3157, 2001.
- [91] A. Ismach, and E. Joselevich, "Orthogonal Self-Assembly of Carbon Nanotube Crossbar Architectures by Simultaneous Graphoepitaxy and Field-Directed Growth," *Nano Letters*, vol. 6, no. 8, pp. 1706-1710, 2006.
- [92] R. Martel, T. Schmidt, H. R. Shea *et al.*, "Single- and multi-wall carbon nanotube field-effect transistors," *Applied Physics Letters*, vol. 73, no. 17, pp. 2447-9, 1998.
- [93] S. J. Tans, R. M. Verschueren, and C. Dekker, "Room temperature transistor based on a single carbon nanotube," *Nature*, vol. 393, no. 6680, pp. 49-52, 1998.
- [94] N. R. Franklin, W. Qian, T. W. Tombler *et al.*, "Integration of suspended carbon nanotube arrays into electronic devices and electromechanical systems," *Applied Physics Letters*, vol. 81, no. 5, pp. 913-15, 2002.
- [95] S. J. Wind, J. Appenzeller, R. Martel *et al.*, "Vertical scaling of carbon nanotube field-effect transistors using top gate electrodes," *Applied Physics Letters*, vol. 80, no. 20, pp. 3817-19, 2002.
- [96] J. J. Cha, M. Weyland, J. Briere *et al.*, "Three-Dimensional Imaging of Carbon Nanotubes Deformed by Metal Islands by Electron Tomography," in *MRS Spring Meeting 2008*, San Fransisco, CA, 2008.
- [97] J. Appenzeller, Y.-M. Lin, J. Knoch *et al.*, "Comparing carbon nanotube transistors - The ideal choice: A novel tunneling device design," *IEEE Transactions on Electron Devices*, vol. 52, no. 12, pp. 2568-2576, 2005.

- [98] J. Appenzeller, "What promises do nanotubes & nanowires hold for future nanoelectronics applications?," *ECE 694A Graduate Seminar*, Purdue University & Birck Nanotechnology.
- [99] V. Derycke, R. Martel, J. Appenzeller *et al.*, "Carbon Nanotube Inter- and Intramolecular Logic Gates," *Nano Letters*, vol. 1, no. 9, pp. 453-456, 2001.
- [100] M. Freitag, J. Chen, J. Tersoff *et al.*, "Mobile Ambipolar Domain in Carbon-Nanotube Infrared Emitters," *Physical Review Letters*, vol. 93, no. 7, pp. 076803, 2004.
- [101] J. A. Misewich, R. Martel, P. Avouris *et al.*, "Electrically Induced Optical Emission from a Carbon Nanotube FET," *Science*, vol. 300, no. 5620, pp. 783-786, May 2, 2003, 2003.
- [102] P. Avouris, "Supertube," *IEEE Spectrum*, pp. 40-45, 2004.
- [103] Z. Yao, H. W. C. Postma, L. Balents *et al.*, "Carbon nanotube intramolecular junctions," *Nature*, vol. 402, no. 6759, pp. 273-6, 1999.
- [104] Y. Massoud, and A. Nieuwoudt, "Modeling and design challenges and solutions for carbon nanotube-based interconnect in future high performance integrated circuits," *J. Emerg. Technol. Comput. Syst.*, vol. 2, no. 3, pp. 155-196, 2006.
- [105] B. Q. Wei, R. Vajtai, and P. M. Ajayan, "Reliability and current carrying capacity of carbon nanotubes," *Applied Physics Letters*, vol. 79, no. 8, pp. 1172-1174, 2001.
- [106] C. Papadopoulos, and B. Omrane, "Nanometer-scale Catalyst Patterning for Controlled Growth of Individual Single-walled Carbon Nanotubes," *Advanced Materials*, vol. 20, no. 7, pp. 1344-1347, 2008.
- [107] C. Papadopoulos, and B. Omrane, "Synthesis of Aligned Single-Walled Carbon Nanotube Networks," in American Chemical Society spring Meeting, Chicago, 2007.
- [108] B. Omrane, and C. Papadopoulos, "A Direct-Write Approach for Carbon Nanotube Catalyst Deposition," *IEEE Transactions on Nanotechnology*, 2009 (*In Press*).
- [109] B. Omrane, and C. Papadopoulos, "Nanopipette Catalyst Writing for Single-Walled Carbon Nanotube Growth," in Materials Research Society spring meeting, San Francisco, 2008, pp. P16.5.
- [110] B. Omrane, and C. Papadopoulos, "Nanoscale Writing of Liquid Catalysts for Carbon Nanotube Growth," in Pacific Centre for Advanced Materials and Microstructures annual meeting, Victoria, 2009.
- [111] S. Motavas, B. Omrane, and C. Papadopoulos, "Large-Area Patterning of Carbon Nanotube Ring Arrays," *Langmuir*, vol. 25, no. 8, pp. 4655-4658, 2009.
- [112] S. Motavas, B. Omrane, and C. Papadopoulos, "Large-Area Arrays of Single-Walled Carbon Nanotube Rings with Tunable Diameter," in American Chemical Society spring meeting, New Orleans, 2008.
- [113] C. L. Haynes, and R. P. Van Duyne, "Nanosphere lithography: A versatile nanofabrication tool for studies of size-dependent nanoparticle optics," *Journal of Physical Chemistry B*, vol. 105, no. 24, pp. 5599-5611, 2001.
- [114] F. Jarai-Szabo, S. Astilean, and Z. Neda, "Understanding self-assembled nanosphere patterns," *Chemical Physics Letters*, vol. 408 pp. 241-246, 2005.
- [115] A. Kosiorek, W. Kandulski, H. Glaczynska *et al.*, "Fabrication of Nanoscale Rings, Dots, and Rods by Combining Shadow Nanosphere Lithography and

- Annealed Polystyrene Nanosphere Masks,” *Small*, vol. 1, no. 4, pp. 439–444, 2005.
- [116] C. Papadopoulos, R. S. van den Boogaard, S. Clutterbuck *et al.*, “Large-area ordered C<sub>60</sub> nanoparticle arrays,” *Nanotechnology*, vol. 18, pp. 2453061, 2007.
- [117] F. Sun, W. Cai, Y. Li *et al.*, “Morphology-Controlled Growth of Large-Area Two-Dimensional Ordered Pore Arrays,” *Advanced Functional Materials*, vol. 14, no. 3, pp. 283-288, 2004.
- [118] B. J. Y. Tan, C. H. Sow, T. S. Koh *et al.*, “Fabrication of size-tunable gold nanoparticles array with nanosphere lithography, reactive ion etching, and thermal annealing,” *Journal of Physical Chemistry B*, vol. 109, no. 22, pp. 11100-9, 2005.
- [119] Y. Wang, X. Wang, J. Rybczynski *et al.*, “Triangular lattice of carbon nanotube arrays for negative index of refraction and subwavelength lensing effect,” *Applied Physics Letters*, vol. 86, no. 15, pp. 153120, 2005.
- [120] M. Winzer, M. Kleiber, N. Dix *et al.*, “Fabrication of nano-dot- and nano-ring-arrays by nanosphere lithography,” *Applied Physics A: Materials Science & Processing*, vol. 63, pp. 617-619, 1996.
- [121] N. Denkov, O. Velev, P. Kralchevski *et al.*, “Mechanism of formation of two-dimensional crystals from latex particles on substrates,” *Langmuir*, vol. 8, no. 12, pp. 3183-3190, 1992.
- [122] K. Nagayama, “Two-dimensional self-assembly of colloids in thin liquid films,” *Colloids and Surfaces A: Physicochemical and Engineering Aspects*, vol. 109, pp. 363-374, 1996.
- [123] J. C. Hulthen, D. A. Treichel, M. A. Smith *et al.*, “Nanosphere Lithography: Size-Tunable Silver Nanoparticle and Surface Cluster Arrays,” *Journal of Physical Chemistry B*, vol. 103, pp. 3854-3863, 1999.
- [124] Interfacial Dynamics Corporation <http://www.idclatex.com>.
- [125] A. S. Dimitrov, C. D. Dushkin, H. Yoshimura *et al.*, “Observations of Latex Particle Two-Dimensional-Crystal Nucleation in Wetting Films on Mercury, Glass, and Mica,” *Langmuir*, vol. 10, no. 2, pp. 432-440, 2002.
- [126] C. D. Dushkin, H. Yoshimura, and K. Nagayama, “Nucleation and growth of two-dimensional colloidal crystals,” *Chemical Physics Letters*, vol. 204, no. 5-6, pp. 455-460, 1993.
- [127] F. Burmeister, C. Schafle, T. Matthes *et al.*, “Colloid Monolayers as Versatile Lithographic Masks,” *Langmuir*, vol. 13, no. 11, pp. 2983-2987, 1997.
- [128] R. Y. Zhang, I. Amlani, J. Baker *et al.*, “Chemical vapor deposition of single-walled carbon nanotubes using ultrathin Ni/Al film as catalyst,” *Nano Letters*, vol. 3, no. 6, pp. 731-5, 2003.
- [129] Z. P. Huang, D. Z. Wang, J. G. Wen *et al.*, “Effect of nickel, iron and cobalt on growth of aligned carbon nanotubes,” *Applied Physics A: Materials Science and Processing*, vol. 74, no. 3, pp. 387-391, 2002.
- [130] Y. J. Yoon, J. C. Bae, H. K. Baik *et al.*, “Growth control of single and multi-walled carbon nanotubes by thin film catalyst,” *Chemical Physics Letters*, vol. 366, 2002.
- [131] K. Henardi, A. Fonseca, J. B. Nagy *et al.*, “Production of nanotubes by the catalytic decomposition of different carbon-containing compounds,” *Applied Catalysis A*, vol. 199, pp. 245-255, 2000.

- [132] R. V. Seidel, "Carbon Nanotube Devices," Fakultät Maschinenwesen der Technischen Universität Dresden, Dresden, 2004.
- [133] L. Ci, Z. Zhou, D. Tang *et al.*, "Double Wall Carbon Nanotubes with an Inner Diameter of 0.4 nm," *Chemical Vapor Deposition*, vol. 9, no. 3, pp. 119-121, 2003.
- [134] S. Bandow, M. Takizawa, K. Hirahara *et al.*, "Raman scattering study of double-wall carbon nanotubes derived from the chains of fullerenes in single-wall carbon nanotubes," *Chemical Physics Letters*, vol. 337, no. 1-3, pp. 48-54, 2001.
- [135] L. Ci, Z. Zhou, X. Yan *et al.*, "Resonant Raman scattering of double wall carbon nanotubes prepared by chemical vapor deposition method," *Journal of Applied Physics*, vol. 94, no. 9, pp. 5715-5719, 2003.
- [136] S. Xie, L. Song, L. Ci *et al.*, "Controllable preparation and properties of single-/double-walled carbon nanotubes," *Science and Technology of Advanced Materials*, vol. 6, no. 7, pp. 725-735, 2005.
- [137] D. S. Macintyre, I. Youngb, A. Glidlea *et al.*, "High resolution e-beam lithography using a thin titanium layer to promote resist adhesion," *Microelectronic Engineering*, vol. 83, no. 4-9, pp. 1128-1131, 2006.
- [138] W. R. McGovern, F. Anariba, and R. L. McCreery, "Importance of Oxides in Carbon/Molecule/Metal Molecular Junctions with Titanium and Copper Top Contacts," *Journal of the Electrochemical Society*, vol. 152, no. 5, pp. E176-E183, 2005.
- [139] I. Radu, Y. Hanein, and D. H. Cobden, "Oriented Growth of Single-Walled Carbon Nanotubes Using Alumina Patterns," *Nanotechnology*, vol. 15, pp. 473-476, 2004.
- [140] R. S. Johnson, G. Lucovsky, and I. Baumvol, "Physical and electrical properties of noncrystalline Al<sub>2</sub>O<sub>3</sub> prepared by remote plasma enhanced chemical vapor deposition," *Journal of Vacuum Science and Technology A*, vol. 19, no. 4, pp. 1353-1360, 2001.
- [141] T. Hertel, R. E. Walkup, and P. Avouris, "Deformation of carbon nanotubes by surface van der Waals forces," *Physical Review B*, vol. 58, no. 20, pp. 13870, 1998.
- [142] Y. Homma, D. Takagi, and Y. Kobayashi, "Suspended architecture formation process of single-walled carbon nanotubes," *Applied Physics Letters*, vol. 88, no. 2, pp. 23115-1, 2006.
- [143] P. M. Albrecht, and J. W. Lyding, "Ultrahigh-vacuum scanning tunneling microscopy and spectroscopy of single-walled carbon nanotubes on hydrogen-passivated Si(100) surfaces," *Applied Physics Letters*, vol. 83, no. 24, pp. 5029-5031, 2003.
- [144] P. M. Albrecht, S. Barraza-Lopez, and J. W. Lyding, "Scanning tunnelling spectroscopy and ab-initio calculations of single-walled carbon nanotubes interfaced with highly doped hydrogen-passivated Si(100) substrates," *Nanotechnology*, vol. 18, no. 9, pp. 095204, 2007.
- [145] Peter M. Albrecht, S. Barraza-Lopez, and Joseph W. Lyding, "Preferential Orientation of a Chiral Semiconducting Carbon Nanotube on the Locally Depassivated Si(100)-2×1:H Surface Identified by Scanning Tunneling Microscopy," *Small*, vol. 3, no. 8, pp. 1402-1406, 2007.

- [146] Peter M. Albrecht, and Joseph W. Lyding, "Lateral Manipulation of Single-Walled Carbon Nanotubes on H-Passivated Si(100) Surfaces with an Ultrahigh-Vacuum Scanning Tunneling Microscope," *Small*, vol. 3, no. 1, pp. 146-152, 2007.
- [147] P. M. Albrecht, and J. W. Lyding, "Atomically Clean Integration of Carbon Nanotubes with Silicon," *Electric properties of synthetic nanostructures: XVII International Winterschool/Euroconference on Electronic Properties of Novel Materials*, vol. 723, pp. 173-180, 2004.
- [148] N. Tayebi, Z. C. Leseman, L. Rotkina *et al.*, "Lattice Aligned Single-Walled Carbon Nanotubes Grown on Silicon Membrane" *Microscopy Society of America*, 2007
- [149] K. B. Lee, E. Y. Kim, C. A. Mirkin *et al.*, "The use of nanoarrays for highly sensitive and selective detection of human immunodeficiency virus type 1 in plasma," *Nano Letters*, vol. 4, pp. 1869-1872, 2004.
- [150] B. Li, C. H. Goh, X. Zhou *et al.*, "Patterning Colloidal Metal Nanoparticles for Controlled Growth of Carbon Nanotubes," *Advanced Materials*, vol. 20, pp. 4873-4878, 2008.
- [151] M. Sokuler, and L. A. Gheber, "Nano Fountain Pen Manufacture of Polymer Lenses for Nano-biochip Applications," *Nano Lett.*, vol. 6, no. 4, pp. 848-853, 2006.
- [152] A. Lewis, Y. Kheifetz, E. Shambrodt *et al.*, "Fountain pen nanochemistry: Atomic force control of chrome etching," *Applied Physics Letters*, vol. 75, no. 17, pp. 2689-91, 1999.
- [153] K. T. Rodolfa, A. Bruckbauer, D. Zhou *et al.*, "Two-Component Graded Deposition of Biomolecules with a Double-Barreled Nanopipette," *Angewandte Chemie - International Edition*, vol. 44, pp. 6854-6858, 2005.
- [154] C. Klinke, "Analysis of Catalytic Growth of Carbon Nanotubes," Section De Physique, École Polytechnique Federale De Lausanne, Karlsruhe, 2003.
- [155] L. Jodin, A.-C. Dupuis, E. Rouviere *et al.*, "Influence of the Catalyst Type on the Growth of Carbon Nanotubes via Methane Chemical Vapor Deposition," *Journal of Physical Chemistry B*, vol. 110, pp. 7325-7333, 2006.
- [156] A. M. Cassell, J. A. Raymakers, J. Kong *et al.*, "Large Scale CVD Synthesis of Single-Walled Carbon Nanotubes," *Journal of American Chemical Society B*, vol. 103, pp. 6484-6492, 1999.
- [157] L. Durrer, T. Helbling, C. Zenger *et al.*, "SWNT Growth by CVD on Ferritin-based Iron Catalyst Nanoparticles Towards CNT Sensors," *Sensors and Actuators B*, vol. 132, pp. 485-490, 2008.
- [158] U. S. N. L. o. Medicine. "Genetics Home Reference, 2009," <http://ghr.nlm.nih.gov/handbook/illustrations/ferritin.jpg>.
- [159] L. W. Liu, J. H. Fang, L. Lu *et al.*, "Chemical vapor deposition of individual single-walled carbon nanotubes using nickel sulfate as catalyst precursor," *Journal of Physical Chemistry B*, vol. 108, no. 48, pp. 18460-18462, 2004.
- [160] Y. Li, W. Kim, Y. Zhang *et al.*, "Growth of single-walled carbon nanotubes from discrete catalytic nanoparticles of various sizes," *Journal of Physical Chemistry B*, vol. 105, no. 46, pp. 11424-11431, 2001.
- [161] S.-H. Hur, C. Kocabas, A. Gaur *et al.*, "Printed thin-film transistors and complementary logic gates that use polymer-coated single-walled carbon

- nanotube networks,” *Journal of Applied Physics*, vol. 98, no. 11, pp. 114302-6, 2005.
- [162] W. Kim, H. C. Choi, M. Shim *et al.*, “Synthesis of Ultralong and High Percentage of Semiconducting Single-walled Carbon Nanotubes,” *Nano Lett.*, vol. 2, no. 7, pp. 703-708, 2002.
- [163] A. Baba, F. Sato, N. Fukuda *et al.*, “Micro/nanopatterning of single-walled carbon nanotube-organic semiconductor composites,” *Nanotechnology*, vol. 20, no. 8, pp. 085301 (6 pp.), 2009.
- [164] T. Schwamb, N. C. Schirmer, B. R. Burg *et al.*, “Fountain-Pen Controlled Dielectrophoresis for Carbon Nanotube-Integrated in Device Assembly,” *Applied Physics Letters*, vol. 93, pp. 193104-1, 2008.
- [165] J. L. Bahr, E. T. Mickelson, M. J. Bronikowski *et al.*, “Dissolution of small diameter single-wall carbon nanotubes in organic solvents?,” *Chemical Communications*, pp. 193-194, 2001.
- [166] R. Katoh, H. Yokoi, S. Usuba *et al.*, “Sonochemical polymerization of benzene derivatives: the site of the reaction,” *Ultrasonics Sonochemistry*, vol. 5, no. 2, pp. 69-72, 1998.
- [167] S. Niyogi, M. A. Hamon, D. E. Perea *et al.*, “Ultrasonic dispersions of single-walled carbon nanotubes,” *Journal of Physical Chemistry B*, vol. 107, no. 34, pp. 8799-8804, 2003.
- [168] X. Lu, M. Grobis, K. H. Khoo *et al.*, “Spatially Mapping the Spectral Density of a Single C<sub>60</sub> Molecule,” *Physical Review Letters*, vol. 90, no. 9, pp. 096802-1, 2003.
- [169] R. E. Smalley, “Discovering the fullerenes,” *Reviews of Modern Physics*, vol. 69, no. 3, pp. 723, 1997.
- [170] T. Tomiyama, S. Uchiyama, and H. Shinohara, “Solubility and partial specific volumes of C<sub>60</sub> and C<sub>70</sub>,” *Chemical Physics Letters*, vol. 264, no. 1-2, pp. 143-148, 1997.
- [171] J. Guo, S. Datta, M. Lundstrom *et al.*, "Towards Multi-Scale Modeling of Carbon Nanotube Transistors," 2006.
- [172] J. Deng, and H. S. P. Wong, “A compact SPICE model for carbon-nanotube field-effect transistors including nonidealities and its application-part ii: full device model and circuit performance benchmarking,” *IEEE Transactions on Electron Devices*, vol. 54, no. 12, pp. 3195-205, 2007.
- [173] T. J. Kazmierski, D. Zhou, and B. M. Al-Hashimi, “A Fast, Numerical Circuit-Level Model of Carbon Nanotube Transistor,” in *Nanoscale Architectures*, IEEE International Symposium on, 2007.
- [174] B. C. Paul, S. Fujita, M. Okajima *et al.*, "Modeling and analysis of circuit performance of ballistic CNFET," *Proceedings - Design Automation Conference*, pp. 717-722.
- [175] D. Jimenez, X. Cartoixa, E. Miranda *et al.*, “A simple drain current model for Schottky-barrier carbon nanotube field effect transistors,” *Nanotechnology*, vol. 18, no. 2, pp. 025201, 2007.
- [176] J. Zou, Q. Zhang, N. Marzari *et al.*, “Theoretical study of the performance for short channel carbon nanotube transistors with asymmetric contacts,” *Physics Letters A*, vol. 372, no. 46, pp. 6940-6943, 2008.

- [177] A. Balijepalli, S. Sinha, and Y. Cao, "Compact modeling of carbon nanotube transistor for early stage process-design exploration," in Proceedings of the 2007 international symposium on Low power electronics and design, Portland, OR, USA, 2007.
- [178] S. Sinha, A. Balijepalli, and Y. Cao, "A Simplified Model of Carbon Nanotube Transistor with Applications to Analog and Digital Design," in Proceedings of the 9th international symposium on Quality Electronic Design, 2008.
- [179] A. A. Odintsov, "Schottky barriers in carbon nanotube heterojunctions," *Physical Review Letters*, vol. 85, no. 1, pp. 150-3, 2000.
- [180] S. Datta, *Electronic Transport in Mesoscopic Systems*, Cambridge, New York, 2003.
- [181] G. Elert. "Resistivity of Aluminum Oxide, 2006," <http://hypertextbook.com/facts/2006/EuniceHuang.shtml>.
- [182] H. Stahl, J. Appenzeller, R. Martel *et al.*, "Intertube Coupling in Ropes of Single-Wall Carbon Nanotubes," *Physical Review Letters*, vol. 85, no. 24, pp. 5186, 2000.
- [183] F. Ruffino, A. Canino, M. G. Grimaldi *et al.*, "Electrical Properties of Self-Assembled Nano-Schottky Diodes," *Journal of Nanomaterials*, vol. 2008, 2008.
- [184] K. Brakke, Surface Evolver v.2.30 available for free at <http://www.susqu.edu/brakke/evolver/evolver.html>, 2008.
- [185] A. Meister, M. Liley, J. Brugger *et al.*, "Nanodispenser for attoliter volume deposition using atomic force microscopy probes modified by focused-ion-beam milling," *Applied Physics Letters*, vol. 85, no. 25, pp. 6260-6262, 2004.
- [186] Q. Cao, H.-s. Kim, N. Pimparkar *et al.*, "Medium-scale carbon nanotube thin-film integrated circuits on flexible plastic substrates," *Nature*, vol. 454, no. 7203, pp. 495-500, 2008.
- [187] K. F. Brennan, "Introduction to Semiconductor Devices," Cambridge: Cambridge University Press, 2005.